

**Thermal properties of atomic-scale
skyrmions in PdFe nanoislands on Ir(111)
investigated by variable-temperature and
time-resolved scanning tunneling
microscopy and spectroscopy**

Dissertation
zur Erlangung des Doktorgrades
an der Fakultät für Mathematik, Informatik und Naturwissenschaften
Fachbereich Physik
der Universität Hamburg

vorgelegt von
Philipp Lindner

Hamburg
2020

Gutachter der Dissertation:

Prof. Dr. Roland Wiesendanger
Prof. Dr. Michael Thorwart

Zusammensetzung der Prüfungskommission:

Prof. Dr. Michael Potthoff
Prof. Dr. Roland Wiesendanger
Prof. Dr. Michael Thorwart
PD Dr. habil. Guido Meier
Dr. Stefan Krause

Vorsitzender der Prüfungskommission:

Prof. Dr. Michael Potthoff

Datum der Disputation:

17. Dezember 2020

Vorsitzender des Fach-Promotionsausschusses PHYSIK:

Prof. Dr. Günter Hans Walter Sigl

Leiter des Fachbereichs PHYSIK:

Prof. Dr. Wolfgang Hansen

Dekan der MIN-Fakultät:

Prof. Dr. Heinrich Graener

Contents

1	Introduction	2
2	Magnetic Nanostructures of Pd/Fe/Ir(111)	4
2.1	Magnetic interactions at the nanoscale	4
2.2	The spin spiral	6
2.3	The skyrmion	7
2.3.1	Structure, size and arrangement	7
2.3.2	Creation and annihilation dynamics	11
2.4	Disordered spin states	14
3	Scanning tunneling microscopy (STM)	16
3.1	Quantum tunneling of electrons	16
3.2	Microscope operation	18
3.3	Scanning tunneling spectroscopy	20
3.4	Spin-polarized STM	21
3.5	Non-collinear magnetoresistance	23
4	Experimental implementation	26
4.1	UHV-system	26
4.2	Low temperature and magnetic field generation systems	28
4.3	STM design and operation	31
4.4	Variable temperature capability and calibration	32
4.5	Pd/Fe/Ir(111) sample preparation and characterization	34
4.6	Cr tip preparation and characterization	39
5	Results	43
5.1	Confirmation of the ordered magnetic phases at low temperature	43
5.2	Thermal influence on skyrmion creation and annihilation dynamics	46

5.3	The ordered phases at elevated temperature	52
5.3.1	Spin spiral, skyrmion and field-polarized phase at $T \approx 40$ K	52
5.3.2	Skyrmion movement and contrast changes	53
5.3.3	Thermal stability of the ordered phases	56
5.4	Observation of disordered structures	59
5.5	The thermomagnetic phase diagram	64
6	Upgrading an existing multi-probe scanning tunneling microscope	67
6.1	Motivation and MP-STM basics	67
6.2	State of the MP-STM before upgrade	69
6.3	Upgrades	72
6.3.1	Improved side scanner XY coarse drive	72
6.3.2	Improved bonding of the side scanner slide plates	73
6.3.3	Proposed general XY coarse drive improvement	75
6.3.4	New side tip design	76
6.4	System tests	77
6.4.1	Tube scanner XY calibration	77
6.4.2	Tube scanner Z calibration	80
6.4.3	Lateral current test	82
7	Conclusion	84
	Bibliography	88
	Publications	94
	Conference contributions	95
	Danksagung / Acknowledgements	97
	Eidesstattliche Versicherung / Declaration on oath	98

Abstract

Magnetic skyrmions show great potential for future data storage and processing technology due to their unique property combination of topological stability and the simultaneous existence of several accessible manipulation pathways. Especially, the subclass of atomic-scale skyrmions could be employed to replace current semiconductor-based logic gates with spintronic devices due to predicted advantages in size, speed and energy consumption.

So far, atomic-scale magnetic skyrmions were observed only at very low temperature $T < 10$ K. Their thermal stability is of high relevance for the transfer of skyrmion-based technology from research to application.

In this work, skyrmions and other magnetic nanostructures of the Pd/Fe/Ir(111) multilayer system were investigated via variable-temperature and time-dependent scanning tunneling microscopy and spectroscopy.

The recently discovered non-collinear magnetoresistance effect was utilized to explore the thermomagnetic phase space up to $B = 3$ T within the temperature range between 1 K and 100 K. The ordered magnetic spin-spiral (SS) and field-polarized (FP) phases, and evidence for the presence of skyrmions (SK) were found at up to $T \approx 78$ K. Indications for temperature-induced skyrmion dynamics were found via the analysis of the stochastic transitions between the SK and the FP state, and by comparison of the observed nanostructures to spin-dynamics simulations from the literature. Additionally, disordered spin structures were found at elevated T and could be identified as a possible manifestation of a predicted fluctuation-disordered state.

The resulting thermo-magnetic phase diagram of the investigated PdFe nanoislands on Ir(111) was found to be in good qualitative and quantitative agreement with predictions from Monte-Carlo simulations of extended Pd/Fe/Ir(111) films.

As a second part of this thesis, several upgrades and successive functional tests were performed on the current iteration of a multi-probe scanning tunneling microscope, which is designated for atomic-scale skyrmion transport experiments. Constant-current images with atomic resolution were achieved on HOPG(0001) for all three microscope tips at ambient conditions.

Kurzfassung

Magnetische Skyrmionen zeigen großes Potenzial für zukünftige Datenspeicherungs- und Datenverarbeitungstechnologien durch eine einzigartige Kombination von topologischer Stabilität und vielfältigen Manipulationsmöglichkeiten. Insbesondere könnten Skyrmionen atomarer Größenordnung verwendet werden, um aktuelle halbleiterbasierte Logikgatter aufgrund vorhergesagter Vorteile bezüglich Größe, Geschwindigkeit und Energieverbrauch durch spintronische Bauelemente zu ersetzen.

Skyrmionen dieser Größenordnung konnten bisher nur bei sehr tiefen Temperaturen $T < 10$ K beobachtet werden, obwohl ihre thermische Stabilität hohe Relevanz für den Transfer von der Grundlagenforschung zur Anwendung von skyrmionenbasierter Technologie aufweist.

In dieser Arbeit wurden Skyrmionen und andere magnetische Nanostrukturen des Pd/Fe/Ir(111) Mehrschichtsystems experimentell mittels temperaturabhängiger und zeitaufgelöster Rastertunnelmikroskopie und -spektroskopie untersucht. Zur Erkundung des thermomagnetischen Phasenraums bis zu $B = 3$ T im Temperaturbereich von 1 K bis 100 K wurde der kürzlich entdeckte nichtkollineare Magnetowiderstand eingesetzt.

Die geordneten magnetischen Phasen, Spinspirale (SS) und feldpolarisierter Zustand (FP), konnten ebenso wie Skyrmionen (SK) bis zu einer Temperatur von $T \approx 78$ K nachgewiesen werden. Durch Analyse der stochastischen Übergänge zwischen den Zuständen SK und FP sowie Vergleiche der beobachteten Strukturen mit Spindynamiksimulationen konnten Hinweise auf eine thermische Aktivierung dynamischer Skyrmionenprozesse gefunden werden. Zusätzlich wurden ungeordnete Spinstrukturen bei erhöhter Temperatur gefunden, die möglicherweise einem ungeordneten, fluktuierenden Zustand zugeordnet werden können.

Das resultierende thermo-magnetische Phasendiagramm der untersuchten PdFe-Nanoinseln auf Ir(111) stimmt qualitativ und quantitativ gut mit Vorhersagen auf Basis von Monte-Carlo Simulationen für ausgedehnte Pd/Fe/Ir(111)-Filme überein.

Der zweite Teil dieser Arbeit besteht aus verschiedenen Verbesserungen und darauffolgenden Funktionstests eines Mehrfachspitzen-Rastertunnelmikroskops, das mit dem Ziel der Durchführung von Transportexperimenten an Skyrmionen atomarer Größenordnung entwickelt wird. Hier konnte atomare Auflösung auf HOPG(0001) bei Raumtemperatur und an Atmosphäre für alle drei Spitzen erreicht werden.

Chapter 1

Introduction

In the last decades, the information age progressed further and further. The availability of personal computers, the internet, smartphones and artificial intelligence based devices to the general public leads to an accelerated computerization of our lives and environment, with an increasing number of new machines equipped with processors and network connectivity appearing in every scientific, economic and social area imaginable.

As a consequence, demand in processing power, data transmission and storage volume increases. The associated electrical power consumption increased to a significant fraction of the global power consumption: In 2018, the data centers responsible for the global internet traffic [1] and the specialized mining hardware of the cryptocurrency *Bitcoin* [2] alone contributed to over 1 percent of the global power consumption, comparable to half of Germany's total consumption [3].

Most energy-intensive are the processors responsible for computation, the data storage units and the associated cooling systems to remove the waste heat, which is generated by movement of electric current through resistive conductors. Therefore, energy consumption can be vastly decreased by replacing current based logical and storage operations with something more efficient.

One way to achieve this goal is the application of spintronics ("spin electronics"), which instead employs the magnetic orientation of nanoscale objects. A promising class of these nanostructures are skyrmions [4], quasiparticle-like knots in the collective magnetization of non-centrosymmetric crystals and thin films composed of multiple atomic layers of magnetic and nonmagnetic metals. The chiral skyrmion structure is stabilized against decay by Dzyaloshinsky-Moriya interaction [5, 6], which enforces a canted angle between neighboring atomic spins in 3d transition metals like iron, cobalt or manganese, mediated by spin-orbit coupling to adjacent heavy metals, and can be manipulated by a multitude of control forces like electric [7] and mag-

netic fields [8], small neutral [9] or spin-polarized [10] electric currents, interaction with atomic defects or adsorbates [11], or highly polarizable capping layers [10].

To create a useful skyrmionic demonstrator, the manufactured device has to be competitive against current semiconductor technology in terms of size and operation temperature. While skyrmions with sizes bigger than integrated circuit logic gates and individual magnetic storage bits have been successfully stabilized and employed at room temperature [12], skyrmions with diameters in the order of a few atoms were discovered so far only close to liquid helium temperatures [7, 10, 13].

This includes the prototypical PdFe double layer on Ir(111), the most experimentally and theoretically investigated sample system with atomic-scale, tunable skyrmions. Therefore, this thesis aims to gain insights into the thermal stability of these skyrmions.

The experimental technique of choice is scanning tunneling microscopy (STM), a method to image topographic [14], electronic [15] and magnetic [16] material properties of surfaces with picometer-resolution in real space by harnessing the exponential distance dependence of quantum tunneling through a controlled vacuum gap between two metals. The time-resolved and variable temperature experiments on magnetic nanostructures in Pd/Fe/Ir(111) are conducted in an ultra-high vacuum chamber system equipped with a custom-designed cryostat and a superconducting magnet.

The second part of this thesis describes upgrades and successive functional tests of key components of a home-built multi-probe scanning microscope, which will be used for skyrmion transport experiments on Pd/Fe/Ir(111) in the near future to further explore the potential of the sample system for the application and understanding of skyrmion physics.

Chapter 2

Magnetic Nanostructures of Pd/Fe/Ir(111)

Pd/Fe/Ir(111) is used as a model-type sample system consisting of a crystalline iridium substrate with a pseudomorphic, monoatomic iron layer on its (111) surface, which is capped by a pseudomorphic palladium monolayer. At $T < 10$ K, three distinct magnetic textures were found in the Pd/Fe/Ir(111) system [10]: Spin spirals, skyrmions and field-polarized state. This chapter describes the competition between several magnetic interactions, which leads to the formation of these magnetic structures, and their resulting properties.

2.1 Magnetic interactions at the nanoscale

The formation of nanoscale magnetic structures is determined by a subtle balance between different magnetic interactions, which will be described here in terms of a micromagnetic model on a two-dimensional lattice. The model approximates the localized 3d transition metal electrons responsible for magnetic effects with an effective, classical atomic spin, localized on the center of its lattice position.

The four relevant interactions competing in the Pd/Fe/Ir(111) system are Heisenberg exchange (term 2.1), magnetocrystalline anisotropy (term 2.2), Dzyaloshinsky-Moriya-interactions (term 2.4) [5, 6] and Zeeman interaction (term 2.3) [17]. The following combined Hamiltonian de-

describes the total energy of a system of atomic spins \mathbf{S}_i in a two-dimensional lattice:

$$\hat{H} = - \sum_{\langle ij \rangle} J_{ij} (\mathbf{S}_i \cdot \mathbf{S}_j) \quad (2.1)$$

$$- A_z \sum_i (S_{z,i})^2 \quad (2.2)$$

$$- \mu B_z \sum_i S_{z,i} \quad (2.3)$$

$$- \sum_{\langle ij \rangle} \mathbf{D}_{ij} \cdot (\mathbf{S}_i \times \mathbf{S}_j), \quad (2.4)$$

where the brackets under the sum sign represent all possible permutations except $i = j$. All stated interactions prefer distinct spin alignments. The exchange interaction prefers collinear alignment of \mathbf{S}_i and \mathbf{S}_j due to the dot product in term 2.1, while the sign of the exchange constant J_{ij} decides about the parallel or antiparallel orientation of the spins.

Spin-orbit interaction introduces magnetocrystalline anisotropy, the preferred spin alignment is collinear to the easy axis of the crystal which is chosen here to be along the z axis without loss of generality.

In an external magnetic field B_z , the spins with total magnetic moment μ tend to align parallel to it, this is called Zeeman energy.

The Dzyaloshinsky-Moriya-interaction prefers a perpendicular alignment between \mathbf{S}_i and \mathbf{S}_j due to the vector product in term 2.4. The left- and right-handed symmetry is broken through the multiplication with the DM-vector \mathbf{D}_{ij} , inducing chirality. This phenomenon can only be found in systems with broken inversion symmetry, like surfaces, interfaces and certain non-centrosymmetric crystals [7, 8, 10, 12, 13, 18–22].

The final magnetic configuration is determined by minimizing the total energy and varies greatly, depending on the relative strength of the interactions, given by the pre-factors in Eq. 2.1-2.4.

The trivial case of no interactions between the spins leads to a paramagnetic ground state with fluctuating spins in random configuration. A ferromagnetic ground state can be constructed by minimizing term 2.1 without the other contributions and only allowing nearest neighbor exchange interaction with positive J_{ij} . All spins align parallel to each other in an arbitrary overall orientation. If an external field acts on the spins, the ground state aligns parallel to B_z by minimizing term 2.3. To prevent confusion with the ferromagnetic ground state, which also consists of a parallel spin configuration, this case is called "field-polarized" in this thesis.

2.2 The spin spiral

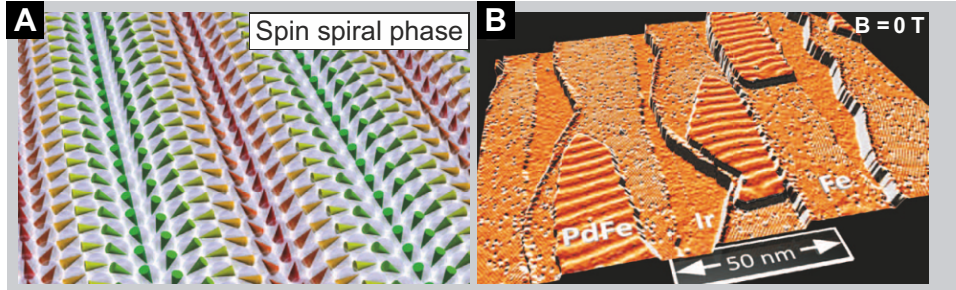


Figure 2.1: The spin spiral ground state of Pd/Fe/Ir(111). A: Simplified cone model with color-coded spin direction, wave vector roughly from left to right. B: 3D representation of a constant current SP-STM image, colored with its derivative. From [10]. Reprinted with permission from AAAS.

The spin spiral is a simple example of a frustrated structure. It can be constructed by introducing ferromagnetic nearest neighbor exchange and DM interaction. Neither parallel nor orthogonal spin alignment can be realized and the minimum solution lies in between, i.e. the spins are canted to each other. Fig. 2.1 A shows a model of such a spiral. The ground state of Pd/Fe/Ir(111) is an inhomogeneous spin spiral with a wavelength $\lambda \approx 7$ nm [10], which corresponds to the stripe pattern on the surface of the Pd/Fe areas in Fig. 2.1 B. The inhomogeneity results from the influence of magnetocrystalline anisotropy, which prefers spins aligned to the [111] direction perpendicular to the surface. The angle between spins, which are nearly collinear to this direction, is decreased, and the angle between spins which are nearly perpendicular to the preferred direction is increased. As a consequence, the spin angle is modulated with a period of half the spin spiral wavelength.

The spin spiral in Pd/Fe/Ir(111) has been studied at $T < 10$ K in [10] and was found to exist up to $|B_z| = 1$ T.

2.3 The skyrmion

If additional Zeeman energy introduced by an external magnetic field is added to the spin spiral, it will be destabilized. The new energy minimum shifts to a configuration with more spins aligned parallel to the external field. In Pd/Fe/Ir(111), this structure consists of individual skyrmions within a field-polarized background.

2.3.1 Structure, size and arrangement

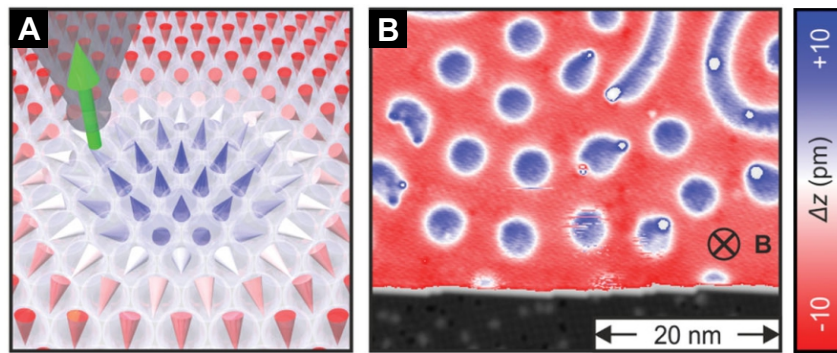


Figure 2.2: Skyrmion structure. A: Simplified cone model of a skyrmion in Pd/Fe/Ir(111) with the field-polarized background. B: Constant-current SP-STM image of the Pd/Fe/Ir(111) surface. The circular blue objects are skyrmions. Same coloring scheme as A. Reprinted with permission from [23]. Copyright (2015) by the American Physical Society.

Fig. 2.2 A shows a model of such a skyrmion in a background of spins polarized parallel to the applied external magnetic field. The central spin of the skyrmion is aligned antiparallel to the background and magnetic field. Starting from there and going outwards, the spins successively rotate by 180 degree to match the surroundings. The radially symmetric skyrmion can be characterized by a topological charge or winding number S [10]:

$$S = \frac{1}{4\pi} \int \mathbf{n} \cdot \left(\frac{\partial \mathbf{n}}{\partial x} \times \frac{\partial \mathbf{n}}{\partial y} \right) dx dy. \quad (2.5)$$

with normalized local magnetization $\mathbf{n} = \mathbf{S}_i / |\mathbf{S}_i|$ and the integration over the whole skyrmion. S counts the number of spin rotations to create the structure from a field polarized background and is a primary measure of how much its corresponding spin configuration is protected from unwinding back to it. For the skyrmion in Fig. 2.2 A, $S = 1$ follows. A hypothetical unwinding of the skyrmion would consist of shrinking the central \uparrow domain until a configuration with only one central \uparrow spin, surrounded by \downarrow spins, is reached. To transform this minimum structure to the

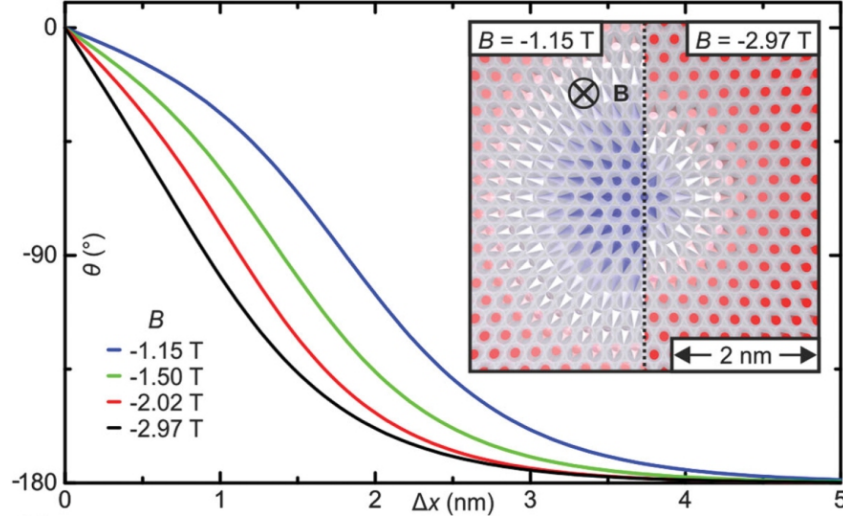


Figure 2.3: Magnetic field-dependent one-dimensional skyrmion profile from center (left) to rim (right). θ is the angle between spin and negative z -axis. The insert compares skyrmion size and structure at high and low $|B_z|$. Reprinted with permission from [23]. Copyright (2015) by the American Physical Society.

completely field-polarized case ($S = 0$), the last spin has to be flipped, which is impossible in a continuous description of the magnetization. Therefore the topological charge is conserved and transitions between different S states are forbidden. This concept of strict topological protection breaks down and translates to a finite potential barrier between different S -states, if the discrete lattice hosting the spin configuration is taken into account [10]. The spin spiral shown in Fig. 2.1 has the winding number $S = 0$, as the directional derivative perpendicular to the spin spiral wave vector in the integrand of Eq. 2.5 becomes zero.

The physical driving force behind the shrinking of the \uparrow -domain is the external magnetic field. A high field increases the amount of Zeeman-energy gained by aligning a maximum amount of spins to the B -field, thereby stabilizing structures parallel to it and destabilizing antiparallel areas like the \uparrow -domain. Consequently, the new energetic ground state of the whole spin ensemble at an increased magnetic field consists of smaller skyrmions, where the \uparrow -domain is reduced in size, as shown in the insert of Fig. 2.3.

Apart from the shrinking of the central area, the wall of the skyrmion also changes its shape: Now the whole 180 degree rotation from the center to the rim has to fit in a much smaller space, thereby increasing the canting angle between neighboring spins. This leads to DM interaction induced energy gain and further skyrmion stabilization, the new equilibrium between the interaction forces determines the smaller skyrmion size. The location of maximum spin canting,

2.3. The skyrmion

equivalent to the inflection point of the angle-distance curves in Fig. 2.3, also moves closer to the skyrmion center.

Due to the B -dependence of skyrmion size, structure and ultimately energy, three different magnetic states can be identified:

1. If the magnetic field exceeds a certain threshold being roughly around $|B_z|= 1$ T, the skyrmions become thermodynamically favored compared to the spin spiral. To transition between both states with different winding numbers (spin spiral: 0, skyrmion: 1), a potential barrier has to be overcome. This kinetic inhibition allows the coexistence of spin spirals and skyrmions in Pd/Fe/Ir(111) [24], which is shown in Fig. 2.4 B.
2. Further increase in $|B_z|$ leads to the complete disappearance of the spin spiral, only skyrmions remain. As huge areas of field polarized spins are still energetically unfavorable due to DM interaction, multiple skyrmions form a loose hexagonally close packed lattice [10] (Fig. 2.4 A,C).
3. If the magnetic field increases even further, the skyrmion lattice dissolved into isolated skyrmions before the fully field-polarized state (Fig. 2.4 D) is reached and becomes the thermodynamically stable phase. Similar to the transition from spin spirals to skyrmions, a potential barrier has to be overcome to transform the skyrmions ($S = 1$) into the field-polarized state ($S = 0$). Consequently, isolated skyrmions can survive as metastable objects in the field-polarized phase (Fig. 2.4 E).

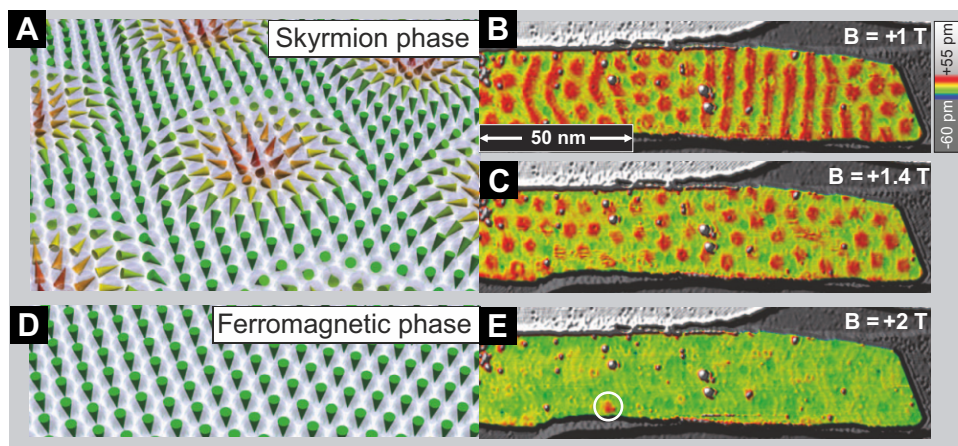


Figure 2.4: Magnetic phases. A,D: Cone models of a skyrmion lattice and field-polarized ferromagnetic phase. B,C,E: Constant-current SP-STM images of the skyrmion sub-phases in a Pd/Fe island on Ir(111). B: Coexistence with spin spiral. C: Skyrmion lattice. E: Field polarized, except for a single, isolated skyrmion marked by the white circle. From [10]. Reprinted with permission from AAAS.

2.3.2 Creation and annihilation dynamics

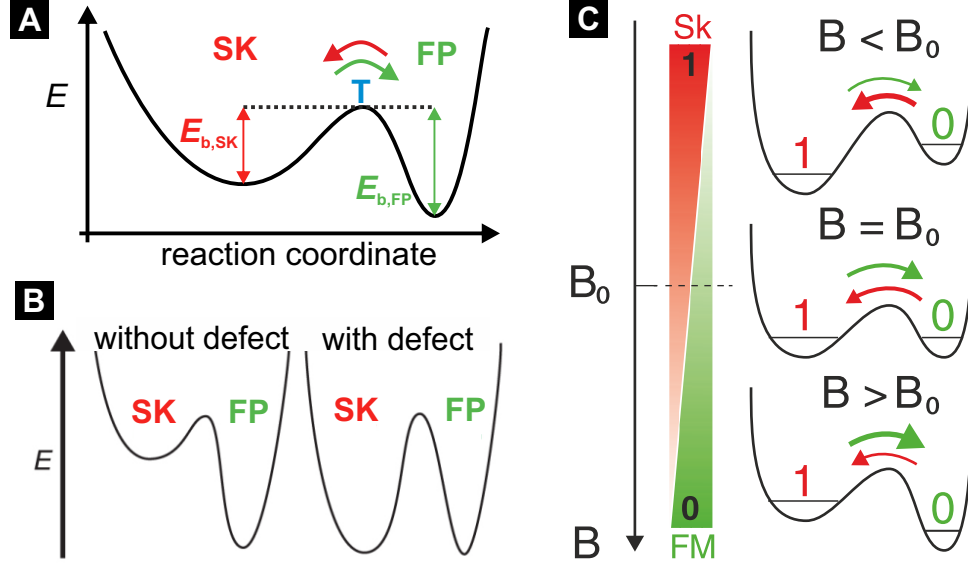


Figure 2.5: A: Simplified potential landscape of the harmonic transition state theory model for skyrmion creation and annihilation. Definitions in the main text. B: Potential landscape modified by pinning to a defect. Adapted from [11], licensed under CC-BY-3.0. C: Magnetic field influence on the potential landscape. FM $\hat{=}$ FP. From [10]. Reprinted with permission from AAAS.

The transition between skyrmion and field-polarized configuration at a fixed location on Pd/Fe/Ir(111) can be described by a simple asymmetric potential, as shown in Fig. 2.5 A. To switch between SK and FP, the system has to overcome an energetic transition state T. The reaction coordinate symbolizes the actual configuration between the pure SK and FP states along an idealized one-dimensional path in the high-dimensional configuration space. Similar to chemical reaction kinetics, the transition rates ν_i between SK and FP can be quantified by an Arrhenius equation with the barrier height corresponding to the difference in energy $E_{b,i}$ between the metastable state i and the transition state [24]:

$$\nu_i = \frac{1}{\tau_i} = \nu_{0,i} \exp\left(\frac{-E_{b,i}}{k_B T}\right), \quad (2.6)$$

with temperature T , state lifetime τ_i , Boltzmann constant k_b and Arrhenius' attempt frequencies $\nu_{0,i}$, which incorporate the entropic differences of the involved states. The asymmetric shape of the potential symbolizes the difference in entropy between SK and FP: the SK state has higher entropy compared to the highly ordered FP state [24]. The potential depth is controlled by Zeeman energy: a high magnetic field increases the SK energy and decreases the FP energy, stabilizing the latter. The relative activation energy for skyrmion creation (FP \rightarrow SK) increases

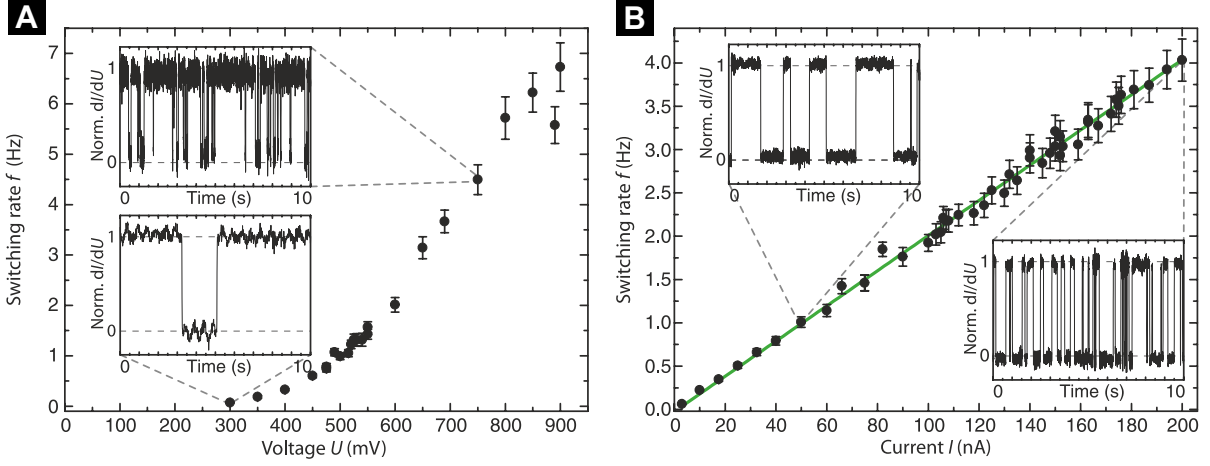


Figure 2.6: Time-averaged switching rate at $T = 4.2$ K between the skyrmion (1) and field-polarized (0) states for a selected pinning position on Pd/Fe/Ir(111); inserts show sections of the magnetic telegraph noise. A: Non-linear voltage dependency at constant tunneling current. $I = 300$ nA, $B = 2.7$ T. B: Linear current dependency at constant bias voltage. $B = 2.9$ T, $U = 650$ mV. From [10]. Reprinted with permission from AAAS.

and the affected SK creation rate is depressed, thereby the lifetime of the FP state increases. Conversely, the SK annihilation rate (SK \rightarrow FM) is increased by the destabilization of the SK state, and the SK lifetime decreases. This effect is shown in the bottom part of Fig. 2.5 C. In the top part of the same figure, the inverse process is shown: a low magnetic field decreases the SK energy and increases the FP energy, thereby stabilizing the former. Consequently, the SK annihilation rate (SK \rightarrow FM) is depressed and the SK lifetime increases. At a critical field $B = B_0$ (middle part of Fig. 2.5 C), creation and annihilation rate are equal. This does not necessarily requires equal SK and FP state energies as implied by the simplified potential in Fig. 2.5 C.

The local potential landscape can not only be influenced by the external magnetic field, but also by pinning to defects in the Pd/Fe/Ir(111) surface, which are caused by incorporation of Fe atoms into the Pd layer [11]. The presence of a different magnetic atom species modifies the relative strength of the prefactors in Eq. 2.1-2.4. Skyrmions were observed to bind to the defect position with their in-plane oriented spins, which are located within a ring around their center. This preferred binding position could be explained for large skyrmions (low magnetic field) either by decreased exchange interaction or increased DM interaction, or generally reduced anisotropy for all skyrmion sizes at the binding site [11]. The result of the pinning is an energetic stabilization of the skyrmion state, as illustrated in Fig. 2.5 B.

Additional mechanisms like pinning to subsurface defects [11], or deflection by other skyrmions

[25] can influence the local skyrmion potential landscape and the associated skyrmion annihilation and creation rates for Pd/Fe/Ir(111).

The switching dynamics of individual skyrmion-hosting positions can be investigated with time-dependent spin-polarized scanning tunneling microscopy [10]. In Fig. 2.6, a magnetic telegraph noise signal (inserts) was recorded by parking the SP-STM tip on top of a pinned skyrmion [10]. The changes in normalized dI/dU reflect the transition between the skyrmion (1) and the field polarized (0) state. The vertical lines at the switching events indicate, that the actual time scale of the transition process is much faster than the time-resolution of the experiment. The displayed transition rate was obtained by averaging over a large number of transitions from both directions and shows a linear current (Fig. 2.6 A) and non-linear voltage dependency (Fig. 2.6 B).

Although a precise explanation for the cause of the stochastic switching is still missing in the published literature as of September 2020, the reported dependencies provide hints about the relative importance of different contributions to the transition rate. The authors of [10] excluded thermal contributions at $T=4.2$ K: Thermally induced switching due to the non-zero sample temperature was ruled out by the vanishing transition rate for $U, I \rightarrow 0$. Localized heating of the sample through the tunneling current was excluded due to a remaining U dependency of the transition rates at constant power UI . Instead, the determining factor was reported to be the energy of the tunneling electrons, which is proportional to the applied bias voltage U .

2.4 Disordered spin states

When temperature is introduced to an ensemble of ordered magnetic spins, thermally induced disorder arises. A historical example for this observation is the ferromagnet-paramagnet transition within the two-dimensional zero-field Ising model [26, 27]: At $T=0$, all spins are aligned \uparrow and the total magnetization of the spin ensemble is at its maximum. The model allows random, temperature induced spin-flips between \uparrow and \downarrow , whose probabilities increase with temperature. The magnetization decreases with temperature and drops to zero when the critical temperature T_c , determined by a certain ratio between thermal energy and spin ordering interaction energy, is exceeded. At this point, half of the spins are \uparrow and \downarrow respectively, and found to be in ferromagnetic domains with fluctuating sizes. While the long-range order of the whole system broke down at T_c , the domains still consist of spins aligned in the same direction. The short-range order decreases further with temperature and breaks down totally for $T \rightarrow \infty$. This simple example shows an important distinction between long-range and short-range order, which also occurs in real magnetic systems.

In Pd/Fe/Ir(111), where the spin interaction is determined by a complex Hamiltonian with at least 4 different contributions (Eq. 2.1-2.4) instead of a single type of interaction, the phase behavior is more complex. At low temperature, the long-range ordered spin spiral, skyrmion lattice and field polarized phases can be found depending on the applied magnetic field. For high temperatures, different predictions based on Monte-Carlo (MC) simulations exist in the literature [28, 29]. They share a common result: after a first critical temperature T_{c1} , which is calculated to be 81 K in [29] and 100 K in [28], the long-range order breaks down and is replaced by a short-range ordered phase, which in turn transitions to the paramagnetic state at a second critical temperature T_{c2} which is calculated to be 250 K in [29] and around 240 K in [28]. In Fig. 2.7, a snapshot of the spin configuration of the short-range ordered phase obtained by MC simulations at elevated temperature is shown [28]. Two distinct structural features can be found: First, an irregular, but connected network of spins with out-of-plane components parallel to the external magnetic field and secondly, compact objects of irregular size and shape with an out-of-plane component anti-parallel to the external field. The objects were interpreted as the result of thermally induced skyrmion creation, annihilation and movement events. In the time evolution of the system, the total topological charge of the spin configuration fluctuates above T_{c1} .

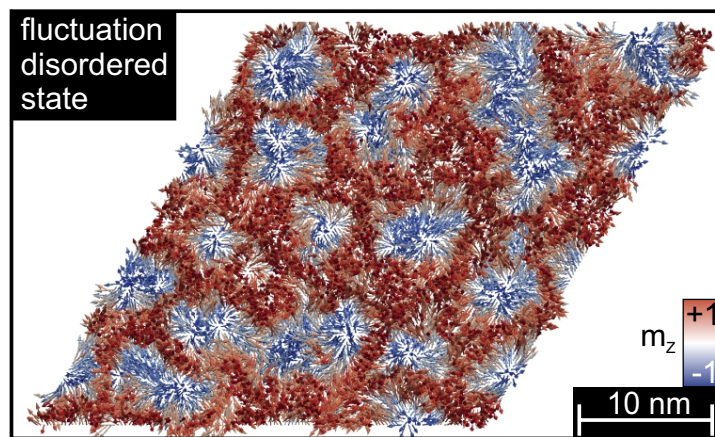


Figure 2.7: Snapshot of the high-temperature fluctuation disordered structure of Pd/Fe/Ir(111), obtained by Monte-Carlo simulations. The simulation field consists of 128×128 spins on a hexagonal lattice with periodic boundary conditions, each one represented by a small arrow. $T = 120\text{K}$, $B = 2\text{ T}$. Spin distribution image reprinted with permission from [28]. Copyright (2016) by the American Physical Society.

Chapter 3

Scanning tunneling microscopy (STM)

This chapter describes the basics of STM operation and the magnetic imaging mechanisms relevant to this thesis.

3.1 Quantum tunneling of electrons

Quantum objects, described by dual particle-like and wave-like properties, can penetrate classically impenetrable potential barriers with a certain probability, even if their kinetic or potential energy is significantly smaller than the barrier height [30, 31]. This behavior is known as quantum tunneling and can, for example, be observed for electrons, which can overcome a vacuum gap between two solid metal objects in close proximity.

Electrons can tunnel from a filled or occupied state to an empty or unoccupied state, if the wave functions of both states overlap, i.e. coexist at least partially in the same region. In metallic solids, for example tip and sample of a scanning tunneling microscope, a huge number of electron states exists, which can be combined to an energy- and location-dependent density of states. Relevant for the tunneling process itself is only the local density of states (LDOS) at the location of the tunneling event. A model of the tunneling process inside the STM was introduced by Tersoff and Hamann [32], considering the sample LDOS $\rho_{\text{sample}}(\mathbf{r}_0, E_F)$ at the center of the tip \mathbf{r}_0 and close to the Fermi level E_F . The model is valid in the low-temperature and small tunneling bias U limits, and assumes s-type wave functions for the electronic states in the tip with radius R . For finite bias voltage, a more generalized equation describes the relationship of the tunneling current between sample and tip (Fig. 3.1) with the convolution of their respective LDOS' [33]:

$$I_T(\mathbf{r}_0, U) \propto \int_0^{eU} \rho_{\text{tip}}(E + eU) \cdot \rho_{\text{sample}}(\mathbf{r}_0, E) dE, \quad (3.1)$$

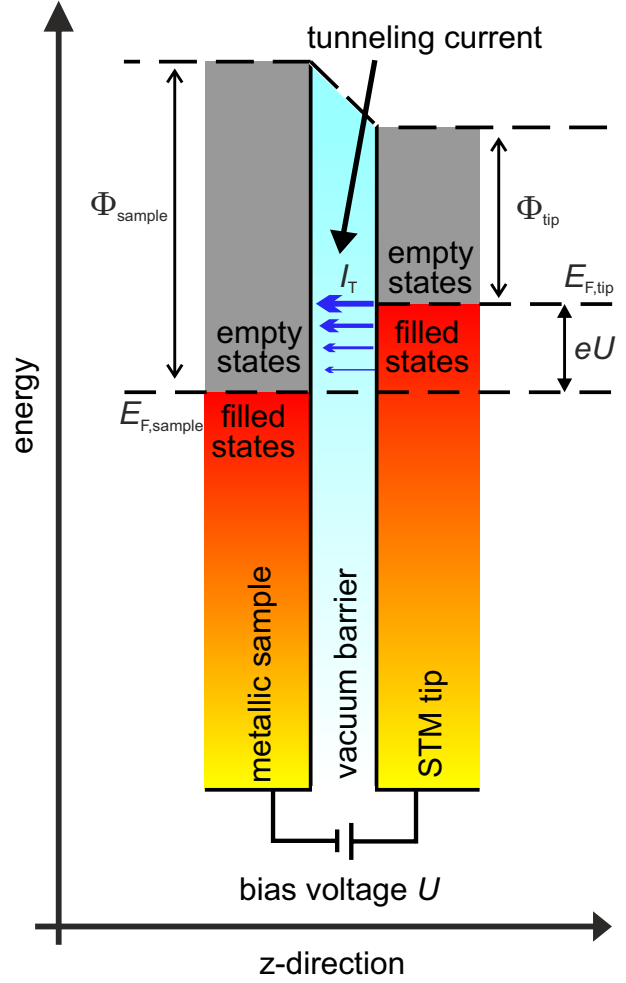


Figure 3.1: Tunneling contact between tip and sample. Applied bias voltage U increases the tip's Fermi level E_F by eU relative to the sample, resulting in a constant tunneling current flow I_T . The blue arrows indicate the higher tunneling probability of electrons near the Fermi edge. The effective barrier height is the mean of tip and sample work function. Adapted with permission from [22].

where all energies E are measured with respect to the Fermi level.

Within this approximation, U is small enough to not disturb the tip and sample wave functions and just results in an energy shift eU of the tip LDOS $\rho_{\text{tip}}(E + eU)$ relative to the sample LDOS. The latter strongly depends on the tip-sample separation s and can be separated in a spatially constant part $\bar{\rho}_{\text{sample}}$ and a transmission coefficient T :

$$\rho_{\text{sample}}(\mathbf{r}_0, E) \propto \bar{\rho}_{\text{sample}}(E) \cdot \underbrace{\exp \left[-2(s + R) \sqrt{\frac{2m}{\hbar^2} \left(\frac{\Phi_t + \Phi_s}{2} + \frac{eU}{2} - E \right)} \right]}_{T(E, eU)} \quad (3.2)$$

T depends on the tip and sample work functions Φ_i , electron mass m , elementary charge e and Planck's reduced constant \hbar , and is the source of the exponential distance-dependency of the tunneling current in the STM.

3.2 Microscope operation

Due to the exponential distance-dependency of the tunneling current, only the tip atom closest to the sample (tip apex) contributes significantly to the total tunneling current. This enables sample examination with atomic resolution in the lateral directions.

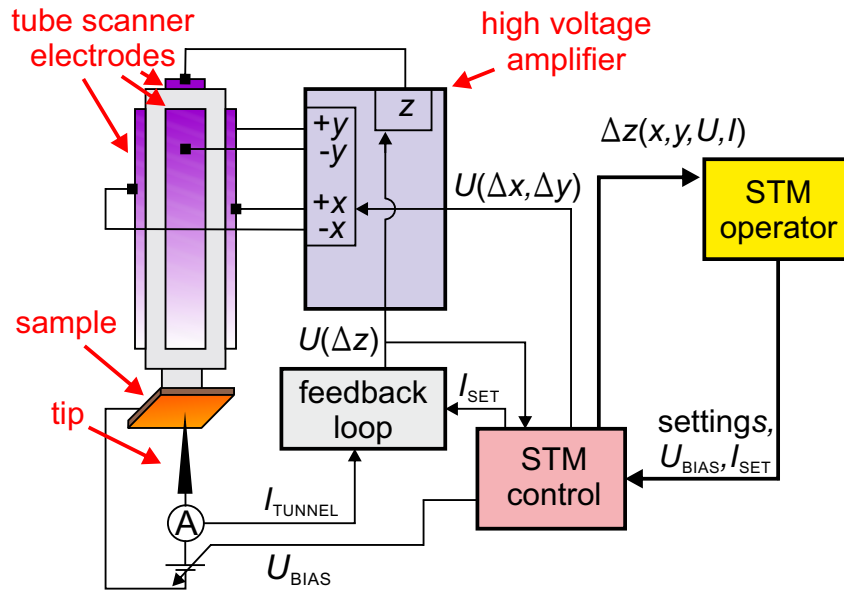


Figure 3.2: Microscope operation in constant-current mode. Tip-sample distance is changed by a piezoelectric tube scanner, which combines lateral and vertical deflection. The feedback loop is regulated by the STM control unit, which also drives the lateral scanning motion of the sample. The control unit is programmed by operator inputs and generates the desired topography images of the sample surface. Adapted with permission from [22].

When an electronic feedback loop (Fig. 3.2) is utilized to stabilize the tunneling current at a fixed lateral tip position, the tip-sample distance will be stabilized, too. Each deviation Δz from a given tip-sample distance creates a change in tunneling current, which is converted to a control voltage $U_z(\Delta z)$, which in turn drives the piezo actuator responsible for z-deflection, effectively negating the change in tip-sample distance. If the sample surface is now scanned laterally (scan voltages $U_x(\Delta x), U_y(\Delta y)$) relative to the tip, the measured control voltages $U_z(\Delta z, U_x(\Delta x), U_y(\Delta y))$ can be used to reconstruct a map of tip height at constant tunneling current $\Delta z(x, y, U, I)$, which contains the encoded nanostructure of the sample and is known as topography or constant-current STM image.

An alternate imaging mode scans the tip over the sample or vice versa at constant height while recording the changes in tunneling current. The resulting map $I(x, y, U, z)$ is free from feedback

3.2. Microscope operation

loop influences, but involves the danger of tip-sample collisions, as the distance between them is not regulated.

Absolute tip (or sample) positions are not known *a priori*, as there is no feasible way to directly measure the absolute height with the desired accuracy. Therefore, the measured control voltage maps have to be calibrated on known atomic-scale structures, e.g. step edge heights or atomic distances on surfaces, determined by e.g. x-ray crystal structure analysis.

A calibration connects the scanner deflection voltages U_x, U_y, U_z to the physical length x, y, z via linear calibration constants C_x, C_y, C_z : $i = C_i U_i$.

The exponential distance dependency of the tunneling current is not only the source of the high lateral and vertical spatial STM resolution, but also of the high sensitivity to external vibrations. The resulting relative vibrations of tip and sample disturb the tunneling current or feedback loop performance heavily, therefore effective vibration isolation is required for low-noise microscope operation.

3.3 Scanning tunneling spectroscopy

Apart from topographic information, the electronic sample properties could be of interest, too. They can be extracted from the differential conductance of the tunneling junction dI/dU , which can be derived from Eq. 3.1 by applying Leibniz's integral rule [15]:

$$\begin{aligned} \frac{dI}{dU}(U) \propto & e \cdot \rho_{\text{tip}}(0) \cdot \bar{\rho}_{\text{sample}}(eU) \cdot T(eU, eU) \\ & + \int_0^{eU} \rho_{\text{tip}}(E - eU) \cdot \bar{\rho}_{\text{sample}}(E) \cdot \frac{dT(E, eU)}{dU} dE \\ & + \int_0^{eU} \frac{d\rho_{\text{tip}}(E - eU)}{dU} \cdot \bar{\rho}_{\text{sample}}(E) \cdot T(E, eU) dE \end{aligned} \quad (3.3)$$

The assumption of small bias dependency of tip LDOS and transmission coefficient allows to neglect both integral terms in Eq. 3.3. The dI/dU signal can then be assumed to be directly proportional to the sample LDOS at the bias voltage and only the electrons tunneling at the Fermi edge contribute to the signal. The differential tunneling conductance can be recorded simultaneously to the control signals in constant-current mode by application of a small amplitude U_{LI} , high frequency f_{LI} modulation to the bias voltage. The resulting high-frequency change in tunneling current is too fast for the feedback loop to react and can be demodulated by a lock-in amplifier. Apart from $dI/dU(U)$ spectra at a fixed location with or without enabled feedback loop, maps of the dI/dU -signal at constant bias and current, which are directly proportional to the sample LDOS, can also be recorded. With careful experimental analysis, it is possible to separate topographic (height) and electronic (LDOS) sample information with this technique.

3.4 Spin-polarized STM

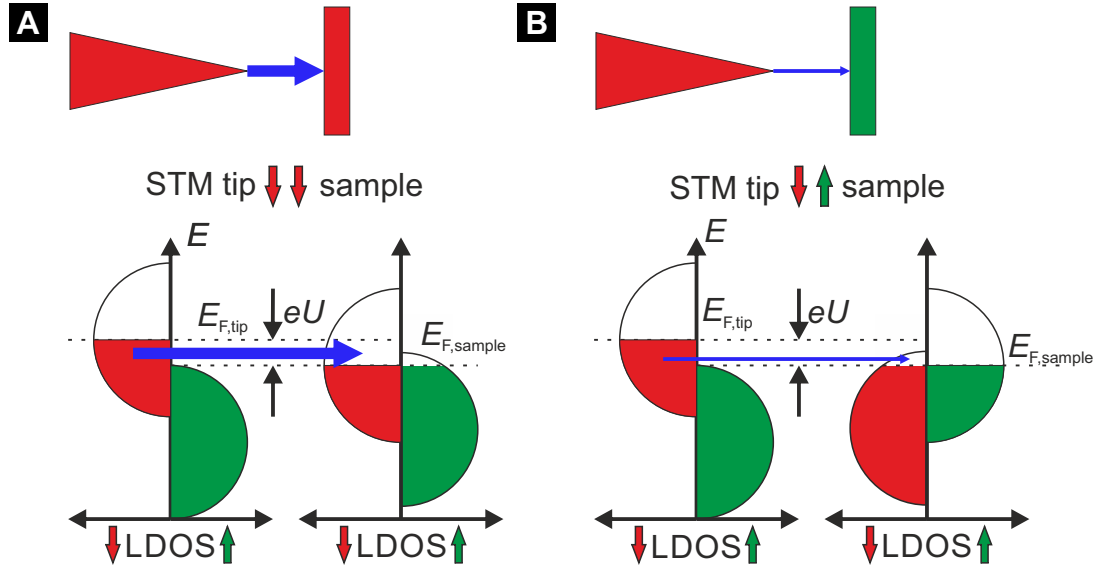


Figure 3.3: Tunneling magneto-resistance. Here, simplified d -type spin sub-bands of tip and sample are shown. Depending on the relative magnetization angle, the \downarrow -tunneling current varies, as the \downarrow - and \uparrow -sub-bands are shifted by the exchange split. \uparrow -current not shown. Adapted with permission from [22].

Apart from topographic and electronic sample information, scanning tunneling microscopy can also be employed to investigate the local magnetic properties of nanostructures.

If the metal-metal tunneling junction from Sec. 3.1 is replaced by magnetic electrodes, the tunneling current and dI/dU vary depending on the angle θ between the magnetization directions of both electrodes. The tunneling conductance is higher for parallel magnetization (Fig. 3.3 A) than for antiparallel alignment (Fig. 3.3 B) and can be described by a $\cos(\theta)$ dependency [34].

For the simple case of ferromagnetic materials, this behavior can be explained by the spin-dependent LDOS at the Fermi edge, which results from an energy split between spin-up (\uparrow) and spin-down (\downarrow)-bands due to exchange interaction [35, 36]. Conservation of spin during the elastic tunneling process only allows tunneling between the same spin-subbands.

Because of the tip and sample LDOS dependency of the tunneling current in Eq. 3.1, the \downarrow -current is high in the parallel case (Fig. 3.3 A) due to high tip and sample LDOS. The \uparrow -current is low, as only a few occupied tip states are available for tunneling. In the antiparallel case (Fig. 3.3 B), the \downarrow -current is lower due to less available empty sample states. The \uparrow -current is still low due to the small number of occupied tip states even though the sample LDOS is now higher than in the parallel case. The total tunneling current is the sum of both spin channels

and higher for the parallel case. Eq. 3.1 can now be rewritten as the sum of a spin-averaged I_0 and a spin-polarized I_{SP} part under the additional assumption of energy-independent tip LDOS within the energy integration interval [37]:

$$\begin{aligned}
 I(\mathbf{r}_0, eU, \theta) &= I_0(\mathbf{r}_0, eU) + I_{\text{SP}}(\mathbf{r}_0, eU, \theta) \\
 &\propto \rho_{\text{tip}} \int g_V(E, eU) \rho_{\text{sample}}(\mathbf{r}_0, E, eU) dE + \mathbf{m}_{\text{tip}} \int g_V(E, eU) \mathbf{m}_{\text{sample}}(\mathbf{r}_0, E, eU) dE,
 \end{aligned} \tag{3.4}$$

with the difference of tip and sample Fermi functions $g_V(E, eU) = f(E) - f(E + eU)$, and the local magnetization density of states of sample resp. tip $\mathbf{m}_i = (\rho_{\uparrow} - \rho_{\downarrow})\mathbf{e}_M$. The latter consists of the difference in \uparrow - and \downarrow -LDOS oriented along the local magnetization direction. Application of Leibniz's rule similar to Eq. 3.3 yields the spin-polarized differential tunneling conductance [37]:

$$\frac{dI}{dU}(\mathbf{r}_0, eU) \propto \rho_{\text{tip}} \rho_{\text{sample}}(\mathbf{r}_0, eU) + \mathbf{m}_{\text{tip}} \mathbf{m}_{\text{sample}}(\mathbf{r}_0, eU) \tag{3.5}$$

Tunneling current and dI/dU -signal variations at different relative tip and sample magnetization are known as **tunneling magnetoresistance (TMR)**.

3.5 Non-collinear magnetoresistance

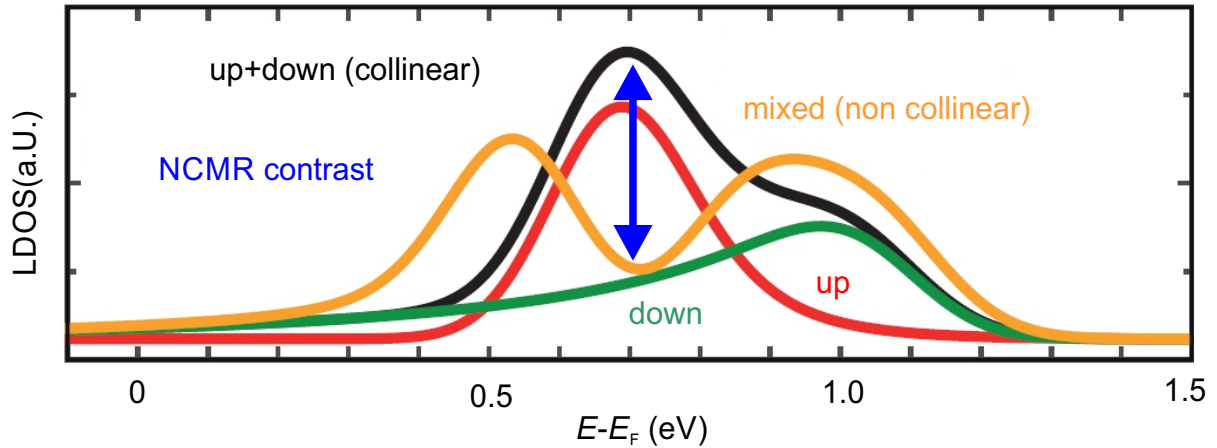


Figure 3.4: NCMR effect. LDOS of hcp-Pd/Fe/Ir(111) simulated by a tight-binding model. In case of collinear neighbors, \downarrow - (green) and \uparrow -LDOS (red) add to the spin-averaged LDOS (black). Non-collinear neighbors lead to hybridization, the resulting LDOS (orange) deviates from the spin-averaged one. The difference between both can be observed as NCMR-contrast via STS with a nonmagnetic tip. Adapted with permission from [9]. Copyright (2015) by Springer Nature.

The last equation showed a possible description of the tunneling current and dI/dU as a sum of the spin-averaged and spin-polarized parts. A recent discovery proved that magnetic nanostructures could also be resolved at high contrast without a magnetic STM tip [9]. They discovered a sample LDOS modulation by the local magnetic environment of the examined sample position. Fig. 3.4 shows the simulated LDOS of hcp-Pd/Fe/Ir(111). The spin-split \downarrow - and \uparrow -LDOS are shown in green and red. Their differences can be resolved experimentally by SP-STM and SP-STs (magnetic tip) via the TMR-effect. Without a magnetic tip, the situation depends strongly on the local environment: When all 6 nearest neighbors \mathbf{S}_i of a central spin \mathbf{S}_a are aligned parallel to \mathbf{S}_a , which is fulfilled for the field-polarized case where all spins are collinear, both spin sub-bands are added to create the black curve. The LDOS-curve is independent of the absolute magnetization direction of the sample and different ferromagnetic domains can not be distinguished. This changes when the nearest-neighbor spins deviate from the parallel alignment to the central spin (non-collinear spins). Now, \downarrow - and \uparrow -channels are mixed and the hybridized LDOS deviates significantly from the collinear case (orange curve). The deviation scales with the angle between \mathbf{S}_i and \mathbf{S}_a averaged over all nearest neighbors [9]. At the particular bias voltage of 700 mV, the difference between collinear and non-collinear LDOS is maximized and a relative dI/dU contrast (blue in Fig. 3.4) of up to 50 % was reported in [9] and up to 30 % for

fcc-Pd/Fe/Ir(111) in [25]. This effect is called **non-collinear magneto-resistance (NCMR)** and was up to now found only on Pd/Fe/Ir(111), 3Fe/Ir(111) and Rh/Co/Ir(111) [7, 9, 13].

TMR and NCMR contrast mechanisms can be combined to further split Eq. 3.5:

$$\frac{dI}{dU} \propto \underbrace{\rho_{\text{tip}}\rho_{\text{sample}}}_{\text{spin-averaged}} + \underbrace{\mathbf{m}_{\text{tip}}\mathbf{m}_{\text{sample}}}_{\text{TMR}} + \underbrace{\sum_i \angle(\mathbf{S}_a, \mathbf{S}_i)}_{\text{NCMR}} \quad (3.6)$$

Another contrast mechanism named **tunneling anisotropic magneto-resistance (TAMR)** based on spin-orbit coupling in the sample [38] contributes to the overall dI/dU -level, but can be neglected for Pd/Fe/Ir(111) due to its small size compared to TMR and NCMR [39]. A detailed discrimination between all three magnetic imaging contributions was performed in [39] and will be conducted here only in a simplified manner.

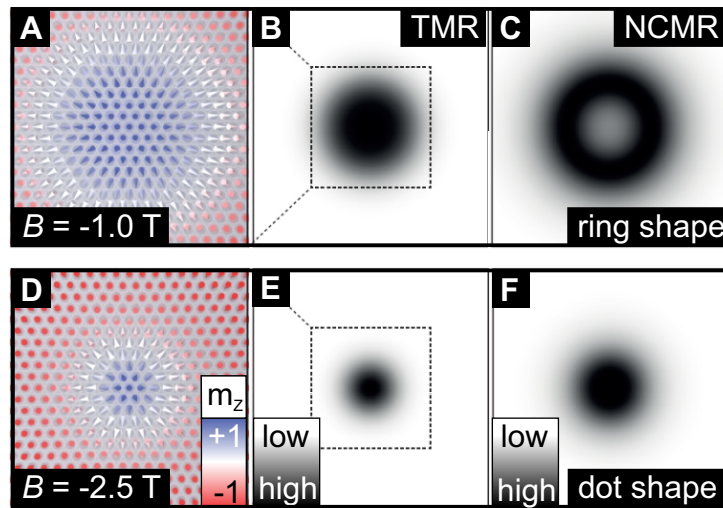


Figure 3.5: How to distinguish NCMR and TMR. Structural model of a skyrmion for low (A) and high (D) magnetic field. Red and blue cones represent local magnetization vectors antiparallel and parallel to the viewing direction, white cones the directions in between. B,E: Simulated STM dI/dU -map with TMR only and tip magnetization antiparallel to the viewing direction. C,F: Simulated STM dI/dU -map with NCMR only and non-magnetic tip. Both effects can be easily distinguished by the different shape at low magnetic fields. Adapted with permission from [9]. Copyright (2015) by Springer Nature.

Fig. 3.5 A and D show a structural model of a skyrmion at high and low magnetic field. For low field, the maximum spin canting and therefore NCMR contrast lies on the circularly shaped set of inflection points far from the skyrmion center (C), while the TMR contribution with a completely out-of-plane tip (B) is maximized in the skyrmion center. Both effects can be distinguished by the skyrmion shape: Ring-like for NCMR and point-like for TMR. At high

3.5. Non-collinear magnetoresistance

magnetic field, the difference vanishes and both mechanisms show the same shape (E,F). The reason for this shift lies in the compression of the skyrmion at higher magnetic fields. The whole 360° spin rotation still has to fit in the skyrmion but has much less space compared to the low-field skyrmion. Therefore, the maximum spin-canting position moves from the edge to the skyrmion center, as the spin angles increase. As the area of collinear spins in the skyrmion center vanishes, so does the ring shape.

Chapter 4

Experimental implementation

This chapter describes the experimental setup of the STM UHV system used in this thesis with emphasis on its essential features. The setup was designed and constructed by Johannes Friedlein and Jonas Harm and is described in detail in [40] and [41].

4.1 UHV-system

Fig. 4.1 schematically shows the experimental setup. The ultra high vacuum (UHV) system consists of three main chambers: STM chamber, molecular beam epitaxy (MBE) chamber and oxygen annealing chamber. A fast entry lock separated by a gate valve enables tip and sample insertion and extraction without breaking the vacuum in the remaining chambers. Sample and tip transfers between the chambers and between individual preparation and analysis facilities can be performed by magnetic transfer manipulators and wobble sticks. The system's base pressure below 10^{-10} mbar can be achieved by a multi-step process: At first, all external openings are closed, the internal gate valves between the chambers are opened and mechanical scroll pumps start to evacuate the chambers. They are installed as roughing pumps on the exhaust side of turbo-molecular pumps, as the latter cannot operate at atmospheric pressure due to aerodynamic drag. As soon as a suitable medium vacuum is achieved, the turbo pumps start to spool up and reduce the pressure down to $p < 10^{-7}$ mbar. Further pressure decrease is now hindered by atmospheric moisture, previously adsorbed to the inner chamber walls. Its high vapor pressure can only be eliminated by removing the water film through a multiple day bake of the whole chamber at up to $T = 425$ K. During and after the bake, turbo-molecular and other types of vacuum pumps further reduce pressure. The latter operate purely electrically without moving parts, examples are titanium sublimation, ion getter and non-evaporable getter pumps, which all adsorb and absorb remaining gas molecules through active chemical species inside the chamber.

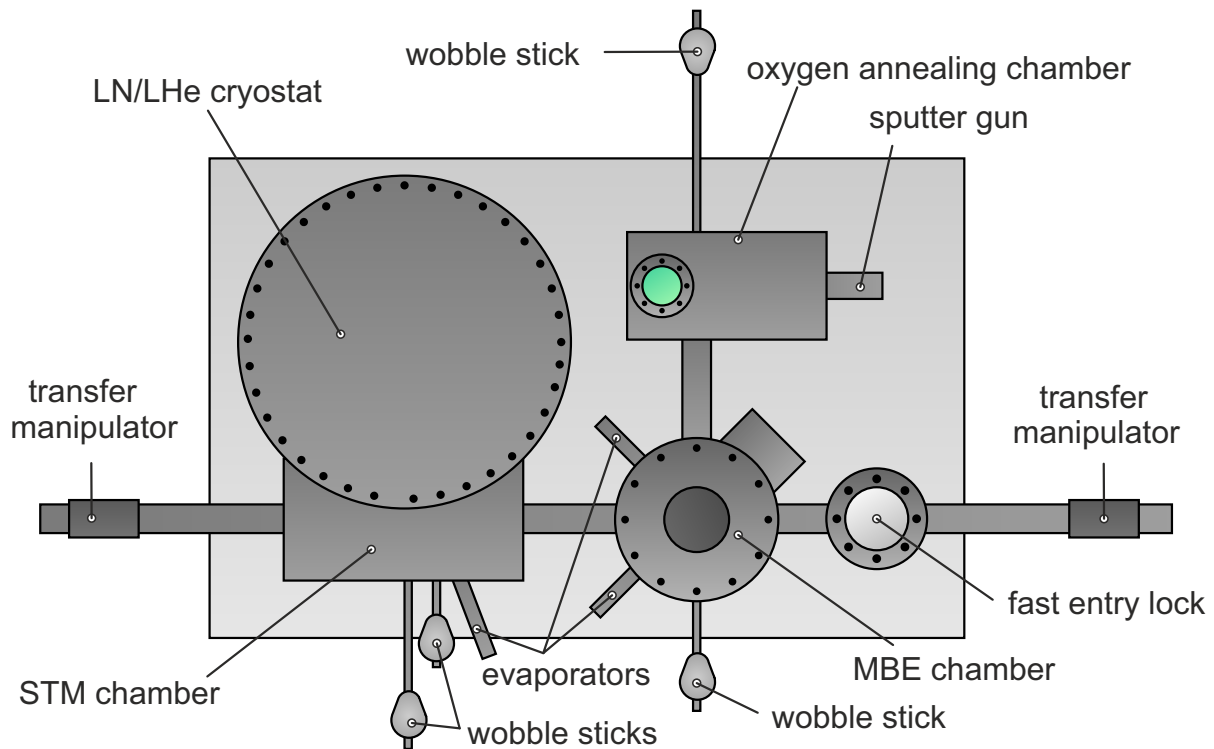


Figure 4.1: Top view schematic representation of the experimental setup. Adapted with permission from [42].

After reaching the base pressure, the turbo-molecular and scroll pumps are separated from the chambers via closed gate valves and subsequently shut down. The remaining non-mechanical pumps do not generate mechanical vibrations, but can hold the necessary base pressure during measurements.

Chamber pressure monitoring is continuously performed with vacuum gauges in all main chambers. Atmospheric to medium vacuum ($p > 10^{-3}$ mbar) gauges are of the Pirani type and exploit the pressure dependency of the thermal conductivity. At lower pressure, the amount of residual gas is too low to employ this principle, and ionization vacuum gauges of the Bayard-Alpert type are used instead. The remaining gas molecules are ionized by thermally emitted electrons and collected by an electrode on high voltage potential. The resulting current correlates to the remaining pressure.

4.2 Low temperature and magnetic field generation systems

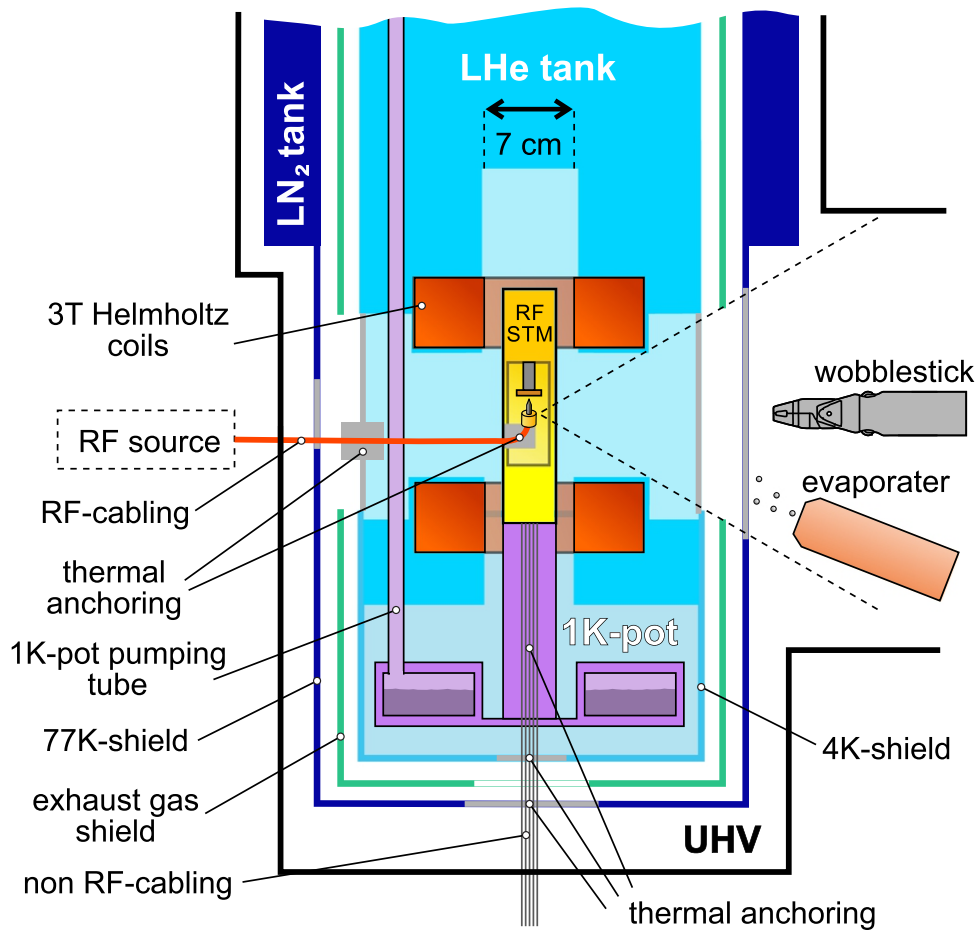


Figure 4.2: Cut view schematic representation of the cryostat system located inside the STM chamber. Reprinted from [41], with the permission of AIP publishing.

Fig. 4.2 shows a cut view of the cryostat system which is used to cool the STM to the desired base temperature. Its structure consists of multiple thermally decoupled concentric cylinders. The outer stage is an open bath cryostat, filled with 120 l of liquid nitrogen (LN_2). Heat removal is implemented by evaporation cooling and subsequent venting of the gaseous nitrogen to the atmosphere. The bath equilibrium temperature of $T = 77 \text{ K}$ and its large thermal mass protect the inner cryostat layers against radiative heat transfer from the room temperature environment. Convective and conductive heat transfer are negligible, as the whole cryostat system is located inside the STM vacuum chamber. The LN_2 bath also cools the outermost radiation shield. Another bath cryostat, filled with 130 l of liquid helium (LHe), is located inside the outer stage. Evaporation cooling leads to a base temperature near the helium boiling point of $T = 4.2 \text{ K}$. The

4.2. Low temperature and magnetic field generation systems

gaseous helium exhaust generated by this process is still very cold and used to cool a radiation shield between the LN₂ and LHe baths to reduce radiative heat transfer between them. Then, the helium gas is led out of the cryostat and collected by the helium recycling system of the building. The LHe bath is directly connected to and cools the third radiation shield. Together, all three shields enclose the STM, the magnet coils and the forced evaporation stage almost completely except for sliding gates to enable wobble stick and evaporator access to the STM. The shields also act as a cryotrapping pump by temporarily adsorbing residual gas molecules on their large surface, further reducing the base pressure around the enclosed STM.

Below the LHe bath, the forced evaporation stage ("1 K-pot") constitutes the innermost part of the cooling system and is thermally decoupled from the bath cryostat via thin stainless steel metal struts with low thermal conductivity. Liquid helium can be transferred from the bath to a 1.2l tank through either a capillary for continuous cooling or a thicker tube for batch cooling. A roots type vacuum pump is located at the exhaust of the 1 K-pot and can depress the helium boiling point down to 1 K. The 1 K-pot is directly connected to the STM at the center of the cryostat, whose only other thermal connections to the exterior are wires. The resulting equilibrium between cooling from below and heat entry through the cables lies at 1.2 K, measured by a temperature diode directly at the STM body.

Superconducting Helmholtz coils located at the center of the cryostat can generate an almost homogenous magnetic field \mathbf{B} of up to ± 3.0 T perpendicular to the sample surface at the tunnel junction of the STM. The coils are enclosed by the LHe bath cryostat and constantly held at their operating temperature $T = 4.2$ K. Magnet operation is controlled by two separate electric circuits, as shown in Fig. 4.3. Both coils consist of superconducting niobium-titanium wire in a copper matrix and are connected to the control unit via thick, normally conducting copper leads. A small applied magnet voltage leads to a huge current inside the coils, which in turn generates the magnetic field, whose orientation and strength can be controlled by current direction and intensity. In this mode of operation, the magnet mode switch from Fig. 4.3 is heated above the critical temperature of an incorporated NbTi wire, which is in the normal-conducting state. Consequently, no current flows through it, as the superconducting magnet coils provide a path with much higher conductivity. After the desired magnetic field strength is achieved, the heater is switched off. Now, the NbTi wire transitions back to the superconducting state, effectively short-circuiting the coils and generating a quasi-perpetual magnetic field through the trapped current (persistent mode). The magnet voltage can now be switched off and the current leads can be disconnected. To change the magnetic field, the procedure has to be reversed.

The temperature of the energized magnet must remain below its critical temperature, else a quench occurs. This phenomenon describes the sudden loss of superconductivity and the re-

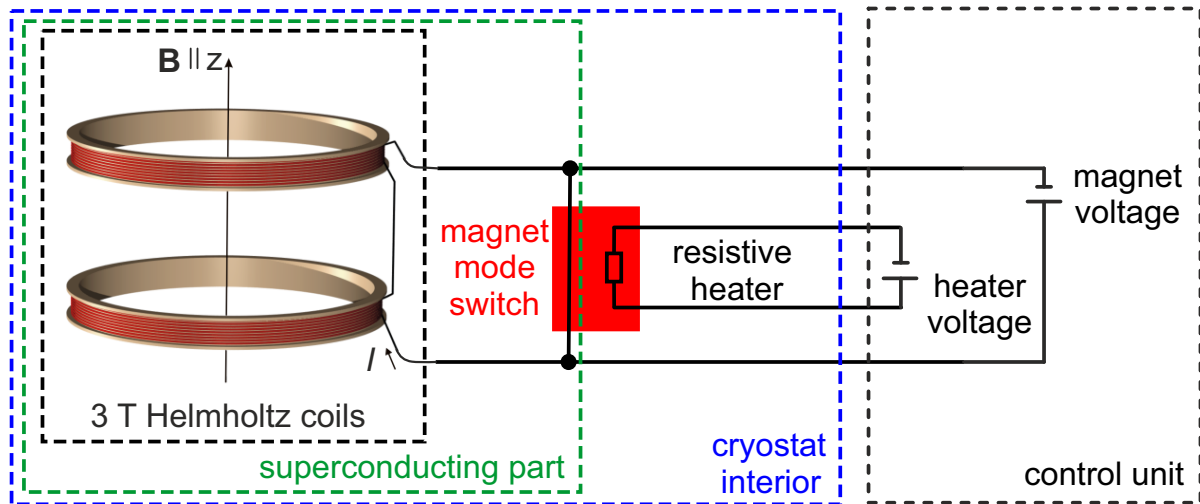


Figure 4.3: Magnet control scheme. The resistive element heats a part of the superconducting circuit above its critical temperature and enables a change of coil current and consequently magnetic field. Without applied heater voltage, the current flows quasi-perpetual through the superconducting circuit (persistent mode). The resulting magnetic field is then independent from the applied magnet voltage. Helmholtz coil image adapted from [43], licensed under CC-BY-SA-3.0.

sulting consequences. When temperature and/or current are too high in parts of the superconductor, a fast transition to the normal-conducting state leads to an increase in resistivity. Now, the current can induce a high voltage which can damage the coils through arcing. Also, the normal-conductive region warms up rapidly through Joule heating, forcing the neighboring areas out of superconductivity through heat transfer. The process cascades then through the whole magnet and the magnetic energy is completely converted to heat, leading to material damage. In modern superconducting coils, the risk of quench damage is greatly reduced through the use of quench protection systems which quickly drain the current to load resistors in the magnet power supply if a voltage variation at the current leads is detected. Nevertheless, the system does not work if the power supply is disconnected or switched off in persistent mode.

Magnet operation also leads to vibration reduction in the STM: The magnetic field induces eddy currents in all conductive parts moving relative to it, greatly damping high frequency vibrations of the STM. The effect depends linearly on the magnetic field.

4.3 STM design and operation

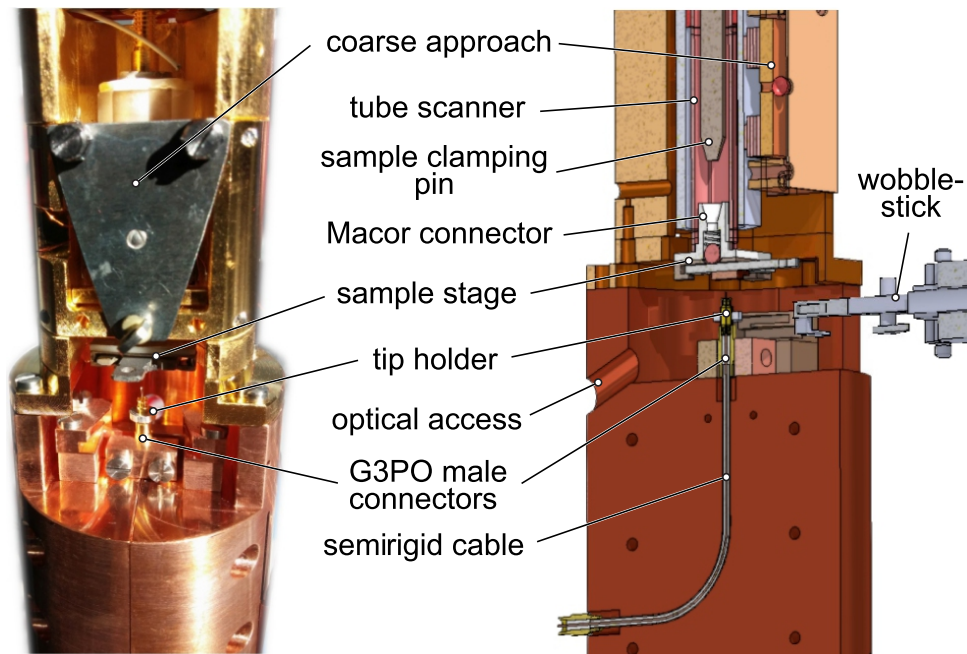


Figure 4.4: Photograph (left) and corresponding 3D sketch (right) of the STM design. The sample stage approaches the tip from above through coarse drive motion. Sample and tip can be exchanged *in situ* via a wobble stick. Reprinted from [41], with the permission of AIP publishing.

Fig. 4.4 shows the design of the STM, which is connected to the 1 K pot described in the section above. Once the sample is inserted into the sample holder via a wobble stick, the coarse approach motor moves a sapphire prism containing the tube scanner with glued-on sample holder to the tip. Then, the sample can be scanned over the fixed tip while the feedback loop described in Sec. 3.2 regulates the tip-sample distance. The reason for this deviation from conventional designs with a scanned tip lies in the rigidity of the installed RF cable, which would impede macroscopic movements of the coarse drive. The cable is tightly clamped to the STM and the LHe bath cryostat to reduce external heat input. The microscope is described in detail in [40, 41, 44].

4.4 Variable temperature capability and calibration

In scanning tunneling microscopy, design considerations for variable temperature capability often antagonize the application of high magnetic fields and vice versa. For magnetic field operation with a superconducting coil, a LHe bath cryostat is needed to prevent the superconducting material from exceeding its critical temperature and subsequent quenching. But if the STM is cooled by the same bath cryostat as the magnet, a large temperature differential between them is not possible. Also, the approach from the direction of a purpose-built variable temperature microscope is not feasible. This type of microscope employs a flow cryostat to control microscope temperature through the balance between helium flow, which is proportional to the cooling power, and radiative and conductive heating from the room temperature parts of the chamber assembly. A safe cooling of a huge magnetic coil cannot be realized this way. But there exist several alternative methods to expose the tunnel junction to magnetic fields: First, permanent magnets could be installed close to the sample or used as tip material, but magnetic flux is inhomogeneous, the field strength can not be adjusted and the total field strength B is limited to the high millitesla range. As a second method, water cooled Helmholtz coils outside the vacuum chamber can provide adjustable field strength with high homogeneity, but total field strength is limited by the huge coil bore and reasonable limits on coil size and cooling water flux. Finally, a separate superconducting magnet system with an air filled bore in its center could be used, in which the STM inside its own vacuum chamber is inserted. Here, the field strength is limited by the bore diameter, too.

The solution for this problem is a STM located inside, but thermally decoupled from the LHe bath cryostat, which cools the superconducting magnet coils. As described in Sec. 4.2, the microscope temperature can be significantly depressed from the bath temperature through the use of forced evaporation cooling. Conversely, it can be significantly higher, if the 1 K pot includes a resistive heating element to warm up, while the magnet coils remain at their operation temperature, safely suspended in the LHe bath. The STM temperature is then balanced between heat flux from the 1 K pot, conductive heat loss through cabling to the LHe bath and radiative heat loss to the surrounding LHe bath and shield. The maximum temperature under full magnetic field strength is likely limited by radiative heat transfer from the STM body to the magnet coils, which increases with T^4 according to the Stefan-Boltzmann law of black body radiation. For the experiments in this thesis, a safe operational upper limit of 100 K was chosen, at which 3.0 T could be easily achieved. A higher temperature should be possible, but the risk of quench damage and subsequent cryostat repairs outweighed the experimental gains here.

When STM experiments are performed at different temperatures, several material properties of

4.4. Variable temperature capability and calibration

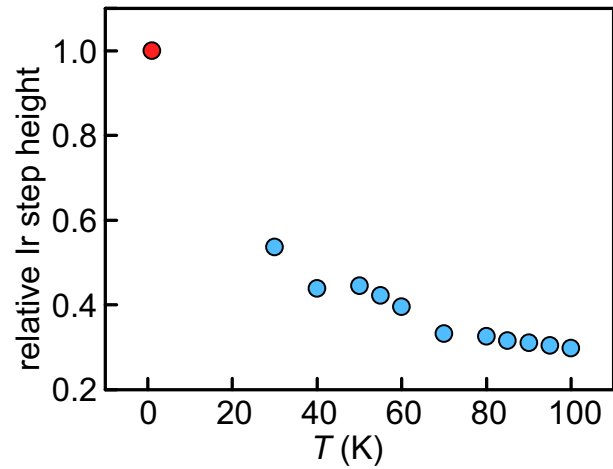


Figure 4.5: Relative Ir(111) step height for different sample temperature. Adapted with permission from [45].

the microscope components influence the results. The dominant contribution is caused by temperature dependent variations in the piezoelectric parameters of the tube scanners. Therefore, the STM has to be calibrated individually for each temperature step. Such a calibration was performed in the Master's thesis of Lennart Bargsten [45], from where Fig. 4.5 was adapted. It shows the relative height of Ir(111) monoatomic step edges, imaged with a piezo drive calibrated at 1.2 K on Au(111). The observed step height decreases with increasing temperature, which means that for a given physical distance, less voltage is required to deflect the tube scanner as the relevant piezoelectric parameter increases. Under the assumption of a constant aspect ratio between lateral and vertical piezoelectric deflection, the x,y and z-values of the STM images have to be multiplied by the inverted relative Ir(111) step heights to correctly display length and topographic height.

4.5 Pd/Fe/Ir(111) sample preparation and characterization

The UHV system is equipped with a multitude of sample preparation facilities. Both the MBE chamber and the oxygen annealing chamber contain two types of sample heaters. For high temperature annealing processes above 1300 K, electron beam heating is used. A tungsten filament from an off the shelf halogen lamp is heated by an electric current and creates free electrons by thermionic emission, which are accelerated to the back side of a sample holder at positive high voltage. Variations in emission current and high voltage are used to control the heating power, and the sample temperature can be monitored remotely with a pyrometer.

Resistive heaters are used to adjust the sample temperature between RT and 1300 K for preparation steps with precise temperature requirements. A glowing tungsten wire inside insulating ceramic tubes heats the sample holder through radiative and conductive heat transfer while temperature monitoring takes place via a chromel/alumel thermocouple.

The oxygen annealing chamber also contains leak valves for the controlled creation of high-purity argon or oxygen atmospheres. Balancing the inflow of processing gas against the turbo-molecular pumping power enables the operator to increase the chamber pressure to typical values of $10^{-6} - 10^{-8}$ mbar. The pure oxygen atmosphere at elevated pressure is important for the process of oxygen annealing which cleans the heated sample surface by oxidation of carbon species which diffuse from the bulk to the surface of metal samples.

Sputtering is the second sample cleaning technique available in the oxygen annealing chamber being especially suited to remove oxide layers or other surface contaminants. Here, argon ions accelerated by high voltage will impact on the sample surface and induce collision cascades in the material. Some atoms are ejected from the sample after these impacts and erode the surface over time. The intensity of this process can be controlled by monitoring the ionic current between the sputtering gun and the sample.

The MBE chamber is used primarily to grow metallic films on the substrate. Different evaporant metal rods of high purity are bombarded with an electron beam to induce local overheating which sublimates the metal atoms without melting the rod itself. The resulting beam of neutral and ionized metal atoms is directed onto the sample. Beam intensity is proportional to the ionic current, which can be measured at the exit of the evaporator. The MBE chamber's sample holder is located on top of a resistive heater. By adjusting beam intensity and substrate temperature, different growth modes can be achieved.

The cleaning procedure for an Ir(111) single crystal is described in [10] and subjects the sample to repeated cycles of sputtering, annealing and oxygen annealing. The experiments in this thesis used a crystal with 0.15° miscut relative to the (111) plane which promotes big terrace growth.

4.5. Pd/Fe/Ir(111) sample preparation and characterization

The sample was inserted in the fast entry lock and transferred to the oxygen annealing chamber to clean the surface:

1. Ar ion sputtering ($p_{\text{Ar}} = 4 \cdot 10^{-7}$ mbar, $U_{\text{accel.}} = 1$ kV, $I_{\text{ion}} = 1.4 \mu\text{A}$, $t > 1$ h) to remove surface contamination from air exposure outside the chamber.
2. Annealing for 30 min at 32 W electron beam power heats the sample to 1450 K and leads to the healing of sputtering damage and diffusion of diluted carbon atoms to the surface, where they create small graphene patches.
3. Ar ion sputtering with the same parameters for 60 min to remove the graphene.
4. Multi step oxygen annealing at $p_{\text{O}_2} = 1 \cdot 10^{-7}$ mbar to oxidize contaminants (20 min at 16 W \rightarrow 20 min at 24 W \rightarrow 10 min at 32 W electron beam power).
5. Repeated sputtering and oxygen annealing leads to the creation of a depletion zone close to the crystal surface with very low amounts of contamination.
6. At a base pressure below $1 \cdot 10^{-9}$ mbar, flash annealing for 60 s at 1450 K removes surface contaminants created by the last oxygen annealing step.

Pd/Fe films from previous preparations can be removed by repeating the cleaning cycle several times. The cleaned crystal was transferred to the MBE chamber to subsequently grow iron and palladium layers on the substrate with the following parameters:

1. < 0.5 ML Fe, $T = 525$ K, $p = 6.8 \cdot 10^{-10}$ mbar, $I_{\text{ionic}} = 10$ nA, $U_{\text{accel.}} = 990$ V, 90 s.
2. < 0.2 ML Pd, $T = 375$ K, $p = 6.2 \cdot 10^{-10}$ mbar, $I_{\text{ionic}} = 5$ nA, $U_{\text{accel.}} = 927$ V, 40 s.

The choice of substrate temperature was determined by a compromise between ideal step flow growth and the avoidance of alloying between Fe and Pd. High temperature promotes regular growth of Pd and Fe monolayers due to the atoms' high surface diffusion. But high temperature also promotes interlayer diffusion, leading to defects, where Fe atoms are incorporated into the Pd layer [11]. The completely prepared sample was transferred to the STM chamber and inserted in the cold ($T = 4.2$ K) STM.

Fig. 4.6 A shows the topography of the prepared Pd/Fe/Ir(111) surface which is divided in terraces of differing width by monoatomic steps of the fcc-Ir(111) substrate. Iron and palladium growth starts at the Ir(111) step edges. The first evaporated layer grows from the step edges and can be identified as fcc-Fe-monolayer terraces, as hcp-Fe can not continue the fcc substrate

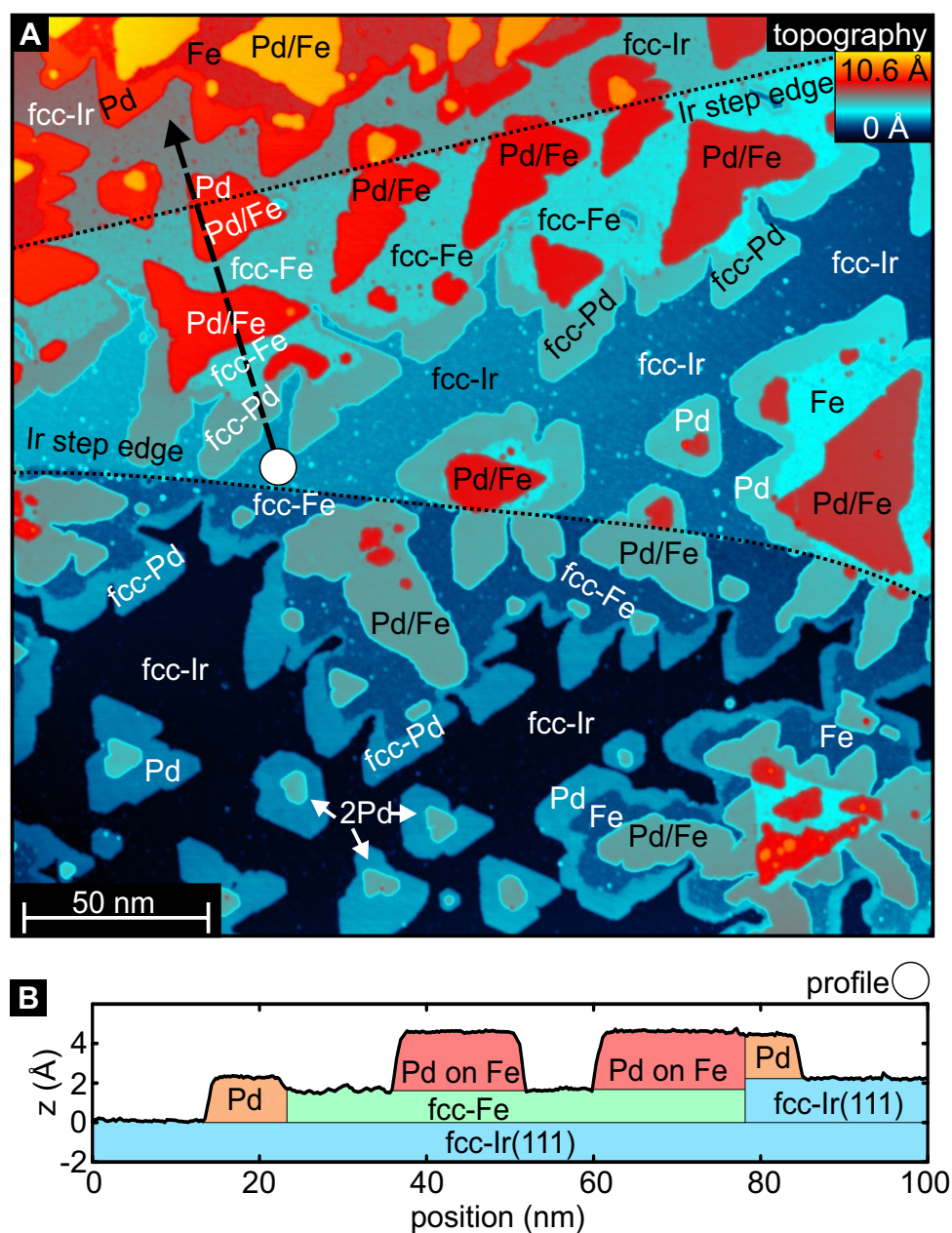


Figure 4.6: Pd/Fe/Ir(111) sample topography. A: Characteristic surface area with different structures and growth modes. B: Height profile and corresponding cut view of the composition along the black arrow in A with position "0" at the white dot. Different materials are represented by different colors. $I_T = 1$ nA, $U = 700$ mV, $T = 4.2$ K, $B = 2.45$ T.

structure and would instead grow as islands. On the edge of the fcc-Fe-ML, a Pd monolayer continues the fcc structure on top of the substrate (Fig. 4.6 B).

Pd grows on top of the Fe terraces in two different modes: Island growth with and without contact to the Ir step edges. Without contact, fcc and hcp stacking are both possible due to the

4.5. Pd/Fe/Ir(111) sample preparation and characterization

absence of defined structures for nucleation, instead contaminant atoms inside the Fe monolayer serve as probable nucleation centers. Pd monolayers also grow directly on the step edges, but lack nucleation structures similar to the non-contact patches. Consequently, hcp and fcc stacking are possible there too. Fig. 4.6 B shows a cut view along the height profile indicated by the dashed line in Fig. 4.6 A, where both growth modes are visible. The Pd island on the right side of the profile grows over the step edge, but shows different heights depending on the layer directly below it.

Apart from the already discussed terrace growth, Fig. 4.6 A also shows islands growing directly on top of the Ir substrate. The big islands, like the one on the right side of the image, consist of an Fe monolayer in fcc or hcp stacking with a partial Pd layer grown on top of it. Similar to the terraces, Pd grows also laterally from the sides of the Fe island. The small islands are probably monolayer Pd with a center of double layer Pd.

To uniquely identify which island has which one of the four possible stacking combinations, two methods can be used: First, relying on the alignment of Fe island edges relative to the Ir steps, fcc and hcp Fe stacking were distinguished in [46]. This method cannot be easily transferred to the preparation used in this thesis, where irregular island shapes hinder the identification. Therefore, the investigation was limited to Pd islands grown on top of fcc-Fe terraces at the Ir step edges. To determine the stacking of the Pd on top of the fcc-Fe, a second method relying on the dI/dU difference between both has been used. At a bias voltage of 700 mV and 1 nA tunneling current, fcc Pd/Fe appears brighter than hcp Pd/Fe [9]. Fig. 4.7 A shows a dI/dU map of a surface area with step-flow growth of Fe terraces at the Ir step edges. On top of the terraces, Pd islands grow. The histogram of the image is displayed in Fig. 4.7 B. The five distinct peaks each correspond to a differently colored surface feature: While Pd/Ir, bare Ir and Fe/Ir appear in different shades of blue in the used color scheme (low dI/dU), the Pd islands can be easily recognized by their yellow color (high dI/dU). Islands with a brighter yellow are fcc Pd, and islands with a darker yellow are hcp Pd.

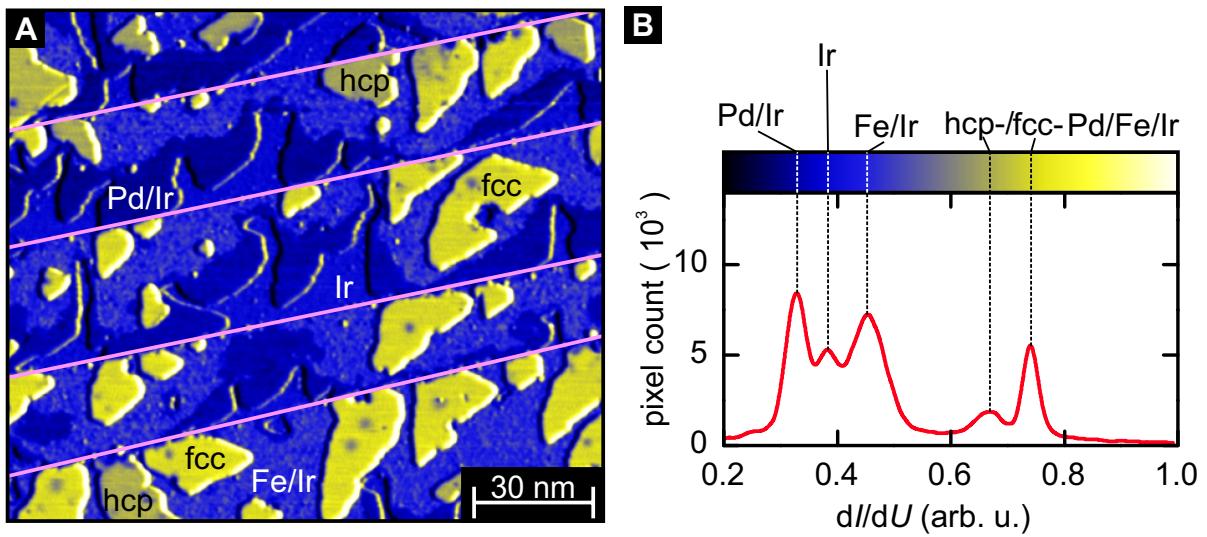


Figure 4.7: Fcc and hcp stacking of the Pd layer on fcc-Fe/Ir(111). A: dI/dU map of a characteristic surface area. Ir step edges are marked by pink lines. B: Histogram of A, peaks correspond to different surface features. fcc-Pd/Fe appears brighter than hcp-Pd/Fe at the tunneling conditions of $I_T = 1$ nA and $U = 700$ mV. $T = 1.28$ K, $B = 2$ T.

4.6 Cr tip preparation and characterization

The STM tips used in this thesis were prepared from an electrolytically etched high purity chromium wire [47], which was glued on a tip holder with electrically conductive epoxy. After the tip was inserted into the STM, short voltage pulses up to 10 V were used for further *in situ* tip preparation.

Antiferromagnetic chromium bulk STM tips are used to resolve the magnetic textures of nanostructures [47, 48]. They are typically sensitive to in-plane and out-of-plane TMR contrast due to a canted tip magnetization [49] and do not generate a stray field in contrast to ferromagnetic bulk or thin film Fe tips. The effective tip magnetic moment and its direction strongly depend on the local nanostructure of the tip apex, therefore one does not only have to prepare an atomically sharp tip, but also one with the right magnetic properties. The upper part of Fig. 4.8 A shows the topography and corresponding dI/dU map of a Pd/Fe nanoisland obtained with such a tip. The three skyrmions within the island are clearly visible as dips in topography and two-lobe objects in dI/dU . A profile through the center of the skyrmion (Fig. 4.8 C (left)) shows a dip followed by a peak along the skyrmion diameter and can be used to reconstruct the actual spin configuration of the skyrmion. The sample magnetization angle $\theta(x)$ relative to the magnetic field along a one-dimensional cut through the skyrmion center x_0 can be approximated by a linear combination of two 180 degree domain walls [23]:

$$\theta(x) = \sum_{+,-} \arccos \left(\tanh \left(\frac{x - x_0 \pm D/2}{w/2} \right) \right), \quad (4.1)$$

with skyrmion center x_0 , diameter D and wall width w . The shape of the experimentally obtained profile is highly dependent on the tip magnetization due to the dI/dU signal being proportional to the cosine of tip and sample magnetization angle:

$$\frac{dI}{dU_{\text{TMR}}}(x) = y_0(1 + A \cos(\theta(x) - \theta_{\text{tip}})), \quad (4.2)$$

with the dI/dU intensity of the field-polarized surroundings y_0 , a scaling factor A , and the angle of the tip magnetization relative to the magnetic field θ_{tip} . Eq. 4.2 can be fitted to the experimental skyrmion profile with fit parameters $y_0, x_0, D, w, A, \theta_{\text{tip}}$ and approximates its shape well, as seen in Fig. 4.8 C (left). The obtained fit parameters x_0, D and w can then be inserted into Eq. 4.1 to reconstruct the underlying spin angle through the skyrmion, which is shown in the bottom left part of Fig. 4.8 C. Additionally, the direction of tip magnetization relative to the magnetic field θ_{tip} can be extracted. When following the tip along the profile through the skyrmion, it first encounters a region of the skyrmion with magnetization antiparallel to it, then

a region parallel to it, resulting in the two-lobe shape. The position of greatest alignment and therefore highest dI/dU signal is marked by the striped green line.

The profile was chosen to go through the positions on the skyrmion with lowest and highest dI/dU in Fig. 4.8 A, therefore the in-plane projection of the tip-magnetization has to be parallel to the profile arrow. Combined with $\theta_{\text{tip}} = (94 \pm 2)^\circ$ obtained from the profile fit, which is equivalent to an almost in-plane tip orientation, the three-dimensional direction of the tip magnetization can be reconstructed.

To compare magnetic structures over a long time at different locations and in varying environmental conditions like a wide range of sample temperatures, which favor accidental tip changes, a reproducible magnetic imaging method has to be used. One such pathway is the tip magnetization-independent NCMR contrast which can be accessed by non-polarized chromium [25, 39] and tungsten tips [7, 9, 39]. Fig. 4.8 A (lower part) and B show the topography and corresponding dI/dU maps of the same nanoisland as discussed above. Now, no indications for a skyrmion can be found in topography, but a characteristic structure (see Fig. 3.5 C) appears in the dI/dU maps. The skyrmion profile (Fig. 4.8 C (right)) appears in a double-dip shape, as the tip moves over the maximum spin canting region twice, which is located outside the skyrmion center at $B = 1.5$ T.

The actual spin structure of the skyrmion can be reconstructed from the NCMR-profile, too [45]: NCMR is sensitive to the average relative angle between a central spin and its neighbors [9], therefore a change in NCMR dominated dI/dU -signal intensity corresponds to a change in angle *difference* between neighboring spins. For the analytical double domain wall approximation of the one-dimensional profile through the skyrmion center (Eq.4.1), this translates to the spatial derivative of θ :

$$\frac{d\theta}{dx}(x) = - \sum_{+,-} \frac{\text{sech}^2\left(\frac{x-x_0 \pm D/2}{w/2}\right)}{\frac{w}{2} \sqrt{1 - \tanh^2\left(\frac{x-x_0 \pm D/2}{w/2}\right)}}, \quad (4.3)$$

under the assumption of a negligible change in θ perpendicular to the profile direction due to the rotationally symmetric skyrmion structure. The total dI/dU intensity can then be approximated as:

$$\frac{dI}{dU}_{\text{NCMR}}(x) = y_0 \left(1 + C \frac{d\theta(x)}{dx}\right), \quad (4.4)$$

with the dI/dU intensity of the surrounding FP region y_0 and a scaling factor C , which incorporates the relative dI/dU difference of SK and FP at the given tunneling conditions. For dI/dU

4.6. Cr tip preparation and characterization

maps at $U = 700$ mV, C is positive, as the negative sign of the derivative already considers the darker skyrmion center relative to the field-polarized surroundings. Eq. 4.4 can be fitted to the experimental skyrmion profile with fit parameters y_0, x_0, D, w, C and approximates its shape well, as seen in the right part of Fig. 4.8 C.

Similar to the TMR case, x_0, D and w can be inserted in Eq. 4.1 to reconstruct θ , which is shown in the bottom right part of Fig. 4.8 C. The spin profiles reconstructed through the resp. TMR and NCMR fits match well. The numerical values for skyrmion diameter and wall width are $D = (2.22 \pm 0.03)$ nm and $w = (1.64 \pm 0.04)$ nm for the NCMR fit and $D = (2.51 \pm 0.07)$ nm and $w = (1.50 \pm 0.07)$ nm for the TMR fit. The small difference between the obtained values can be explained by a different skyrmion configuration of the island in Fig. 4.8 A to B. In [25], skyrmion displacement and compression due to the presence of other skyrmions in a confined island geometry was found to change the apparent skyrmion width up to 15 %. Additionally, the TMR fit implicitly assumes no NCMR contribution to the recorded dI/dU signal, although magnetic contrast generated by Cr bulk tips is a combination of NCMR and TMR contributions, as shown in Eq. 3.6. NCMR is always present at $U = 700$ mV, but the TMR part highly depends on the tip magnetization. Both effects can be discriminated by two factors: First, the NCMR contribution was not visible in topography, therefore structures in topography indicate TMR contrast. Secondly, the unique NCMR dI/dU skyrmion shape will be disturbed by any in-plane TMR contribution which can be easily identified. The only tip magnetization direction which cannot be excluded this way, is purely out-of-plane, parallel to the magnetic field. It would not deform the NCMR skyrmion shape in an unambiguous way, but should be visible in the constant-current map.

All STM measurements and images in chapters 4 and 5 of this thesis except Fig. 4.8 were taken with a Cr tip without noticeable spin polarization.

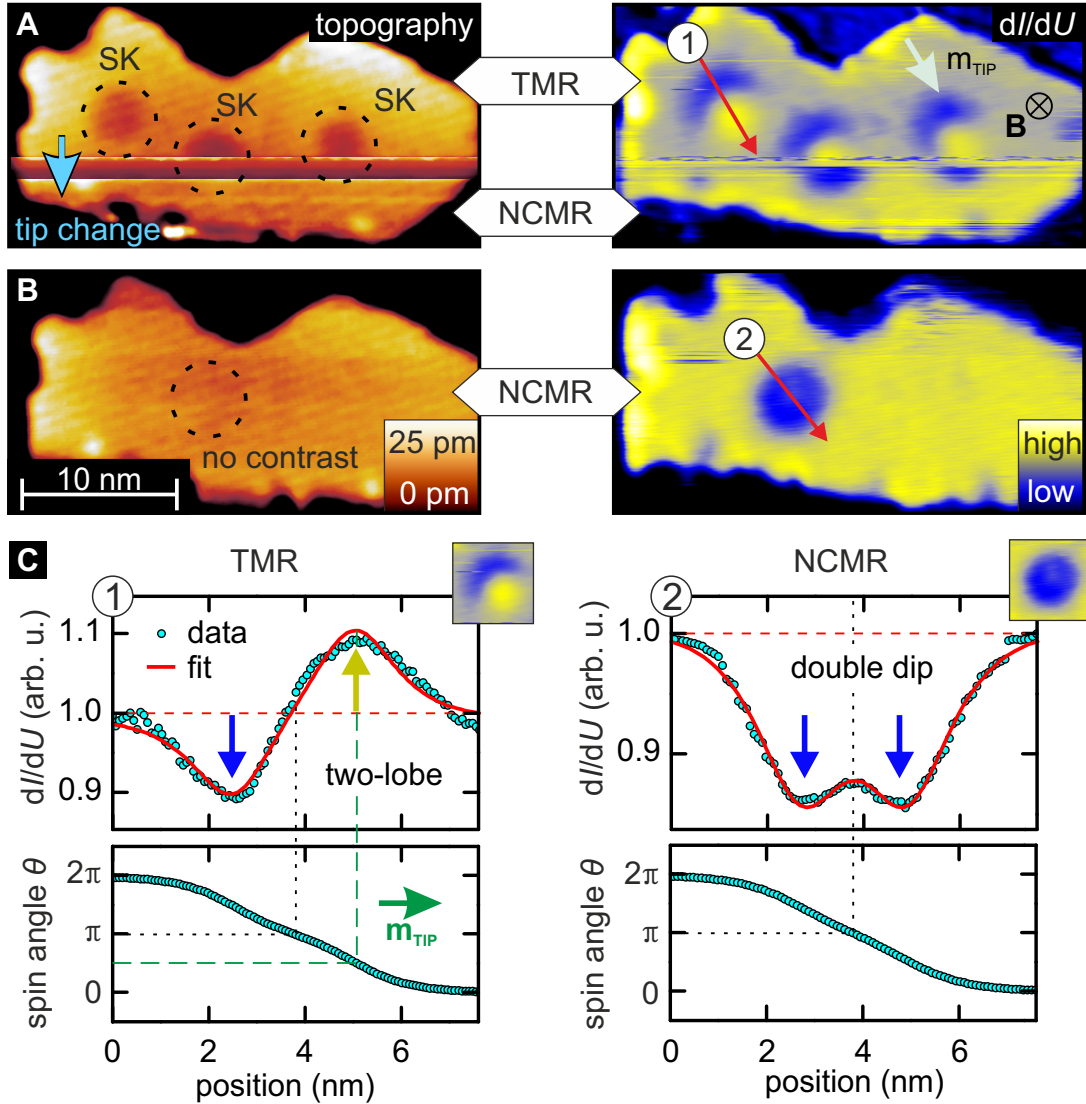


Figure 4.8: TMR and NCMR imaging with a chromium bulk tip. A: Topography (left) and dI/dU -map of a Pd/Fe nanoisland. An accidental tip change occurred during the scan and lead to switching between TMR- (top) and NCMR- (bottom) dominated contrast. B: Same nanoisland, recorded with NCMR contrast only. Note the difference in skyrmion configuration compared to A. C: Line profiles along the red arrows in A and B, fitted with the TMR resp. NCMR functions defined in the text. TMR (left) shows a two-lobe structure, whereas a double-dip like feature is observed with NCMR contrast (right). Bottom row: Corresponding spin angles relative to the magnetic field, reconstructed from the fit functions. $I_T = 1$ nA, $U = 700$ mV, $T = 1.2$ K, $B = 1.5$ T.

Chapter 5

Results

This chapter contains the results of the experimental investigation of the Pd/Fe/Ir(111) system at low and elevated sample temperatures.

5.1 Confirmation of the ordered magnetic phases at low temperature

The known spin spiral, skyrmion and field-polarized phases were confirmed for the prepared Pd/Fe/Ir(111) sample as a control experiment. Fig. 5.1 combines the results of this confirmation: Fig. 5.1 A shows the topography (left) and corresponding dI/dU -map (right) of a nanoisland at zero external field. A meandering structure with a wavelength close to 3.5 nm between locations alternating with high and low signal intensity can be found in the dI/dU map. This structure is a spin spiral, imaged by NCMR contrast. An ideal, homogeneous spin spiral would be invisible, as the angle between neighboring spins, averaged over all 6 neighbors, would be the same at all positions of the spin spiral, providing no NCMR contrast. Due to magnetocrystalline anisotropy with an out-of-plane (oop) easy axis in Pd/Fe/Ir(111), the atomic spins gain energy by increased collinear alignment to the easy axis. Therefore, regions aligned closer to the easy axis (oop spin orientation) grow and regions aligned perpendicularly to the easy axis (in-plane (ip) spin orientation) shrink compared to the homogeneous case. As the spin spiral still consists of a full 360° rotation, the angle between neighboring spins increases in the ip and decreases in the oop region, leading to a periodic modulation in NCMR contrast with half of the magnetic wavelength. The length of two periods of the structure in the dI/dU -map of Fig. 5.1 A matches the observed 7 to 8 nm magnetic spin spiral wavelength in the literature well. In Fig. 5.1 B (right), three skyrmions can be found at moderate magnetic fields. The typical low-field skyrmion ring shape caused by the NCMR contrast mechanism is well pronounced for the

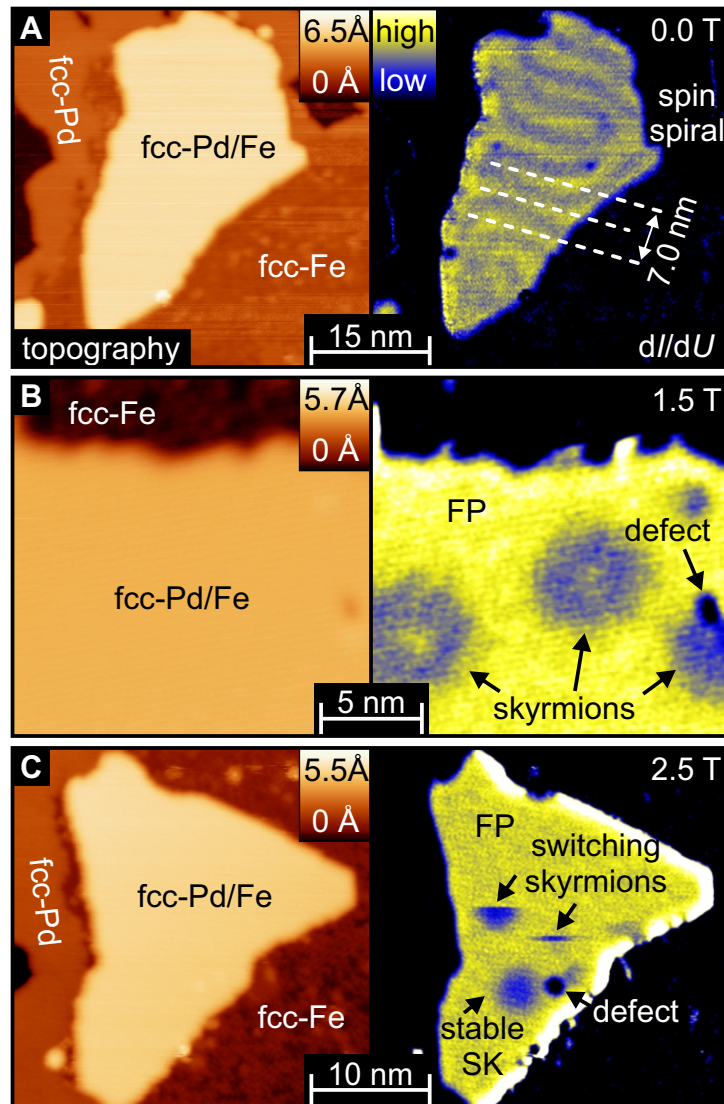


Figure 5.1: Low temperature magnetic phases of fcc-Pd/Fe/Ir(111). Left side: Constant-current topography. Right side: Simultaneously obtained dI/dU -maps acquired via NCMR contrast. A: Spin spiral phase on the whole nanoisland, $T = 2.1$ K. B: Skyrmions in field-polarized background, $T = 1.8$ K. C: One stable skyrmion and two switching skyrmion sites with field-polarized background, $T = 1.3$ K. All images: $I_T = 1$ nA, $U = 700$ mV.

left and middle skyrmion, whereas the right one is closer to the high-field dot shape. Skyrmion stability can be influenced by repulsive interaction with other skyrmions in confined geometries, leading to variations in diameter and apparent NCMR-based shape even for the same nanoisland [25]. The rest of the island appears uniform, indicating a constant angle between neighboring spins in these areas. This corresponds to the field-polarized state, where all spins are aligned to the external magnetic field. At further increased magnetic field (Fig. 5.1 C), the skyrmions

5.1. Confirmation of the ordered magnetic phases at low temperature

appear dot shaped as the location of maximum spin canting moves closer to the skyrmion center. The partial skyrmions shown in Fig. 5.1 C are artifacts of the scanning process and occur when a switching (Sec. 2.3.2) between the SK and FP state occurs just during the scan over the skyrmion. The distinction between a stable and switching skyrmion is also highly dependent on the experimental time scale and tunneling parameters, here the lower skyrmion is stable during the scan time of around 10 minutes.

To summarize, the low-temperature ordered phases could be reproduced: The spin spiral wavelength matches the ones in [10], the observed skyrmion shapes transforms from the low-field ring to the high-field dot due to the NCMR contrast mechanism [9], and also shows switching behaviour [10]. No regular skyrmion lattice phase could be observed, caused by the irregular shape and the size constraints of the nanoislands. The areas in between the skyrmions are uniform in dI/dU intensity and therefore indicate the coexistence of the field-polarized state.

5.2 Thermal influence on skyrmion creation and annihilation dynamics

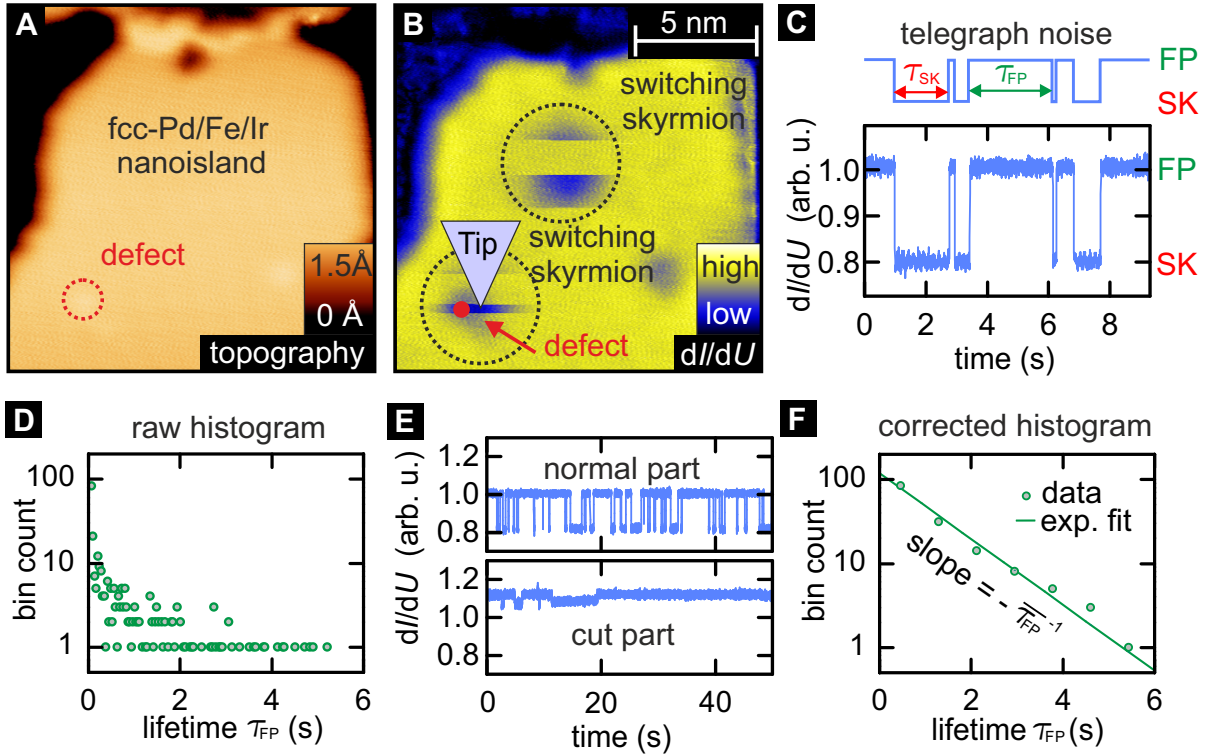


Figure 5.2: A: Constant-current topography of a fcc-Pd/Fe nanoisland. B: Simultaneously recorded dI/dU map with two switching skyrmion sites, one pinned to the defect. C: Section of the recorded dI/dU telegraph noise signal, obtained at the tip position indicated in B, with definitions of skyrmion and field-polarized lifetimes. D-F: Signal correction and mean lifetime extraction. D: Uncorrected FP lifetime histogram, deviation from the exponential distribution is caused by errors in automated lifetime detection, triggered by a shift in telegraph signal amplitude. E: Examples for normal and cut parts of the telegraph signal. F: FP lifetime histogram without the cut parts. The decay constant of the exponential distribution fit corresponds to the inverse mean lifetime. Analog method for SK lifetimes not shown. A,B: $I_T = 1$ nA, $U = 700$ mV, $T = 1.23$ K, $B = 2.5$ T. C-F: $I_T = 10$ nA, $U = 700$ mV, $T = 6$ K, $B = 2.5$ T.

The appearance of fractional skyrmion artifacts in dI/dU maps is caused by switching between the SK and FP state, which can be accessed and evaluated by telegraph noise signal analysis, which was first described for thermally induced magnetization switching of superparamagnetic Fe nanoislands on Mo(110) in [50] and applied to the SK-FP switching on Pd/Fe/Ir(111) in [10]. Fig. 5.2 A and B show a constant-current topography and dI/dU map of a fcc-Pd/Fe nanoisland, which hosts two sites with switching skyrmions. The STM was stabilized over the center of the

5.2. Thermal influence on skyrmion creation and annihilation dynamics

lower site, and the fluctuating dI/dU signal recorded. A time-trace of this signal is shown in Fig. 5.2 C and consists of varying durations of alternating high and low dI/dU with vertical transitions between them. High and low signal levels correspond to the absence (high,FP) and presence (low,SK) of a skyrmion at the tip position. The actual transition process between both states cannot be resolved by the experimental time resolution, which is limited by the chosen integration time of 3 ms of the lock-in amplifier which is used to record the dI/dU signal.

As shown in Fig. 5.2 C, the individual state lifetimes τ_{SK} and τ_{FP} are defined by the duration, over which a dI/dU -signal corresponding to the SK or FP state remains at the same level. If the dI/dU -signal switches from SK to the FP level, the event is called "annihilation"; and "creation", if it switches back to the original SK level, respectively.

In Fig. 5.2 C, the times between transition events are not constant. The transitions between the SK and FP states can be described by individual stochastic Poisson processes, where the actual probability of a transition event is time-independent. As a result, the random lifetimes τ_i follow an exponential distribution $N(\tau_i) = N_0 \exp(-\tau_i/\bar{\tau}_i)$ with the number of lifetimes of a certain duration $N(\tau_i)$, a proportionality factor N_0 , and the average lifetime $\bar{\tau}_i$.

The average lifetimes of the FP and SK states can be extracted by histogram analysis of the telegraph noise signal. Due to the large number of transition events $300 < n < 4000$ at each of the data points in this study, manual extraction of the individual τ_i would be tedious, and a computer program is utilized to register the jumps in the signal, instead. The number of events with high or low signal in a certain τ_i -interval is then plotted against τ_i . Fig. 5.2 D shows the raw τ_{FP} histogram of a 360 s long telegraph signal, obtained by this method. The result does not follow an exponential distribution, which would be linear in the logarithmic plot. This is caused by a change in the telegraph signal amplitude midway in the signal, which triggers errors in the automated detection scheme. While events in the "normal" part of the telegraph noise signal (Fig. 5.2 E top) are registered correctly, the signal amplitude is close to the noise level in the corrupted part (Fig. 5.2 E bottom), and noise is registered as a switching event. Therefore, the program has to be supervised in the event detection. The low amplitude part of the signal was probably caused by thermal drift of the tip from the SK center to the SK rim, where the difference in dI/dU between SK and FP is lower, and consequently cut from the time-trace. The remaining part was reanalyzed and the resulting histogram is shown in Fig. 5.2 F. Now, the lifetimes follow the expected exponential distribution of the Poisson process. In general, the validity of the recorded telegraph noise signal can be judged by checking the lifetime histogram, as certain factors like a changed configuration of the neighboring [25] or remote [40] skyrmions can displace skyrmions from their original position and therefore change the telegraph noise signal. The corrected histogram was fitted with the exponential distribution function, and the

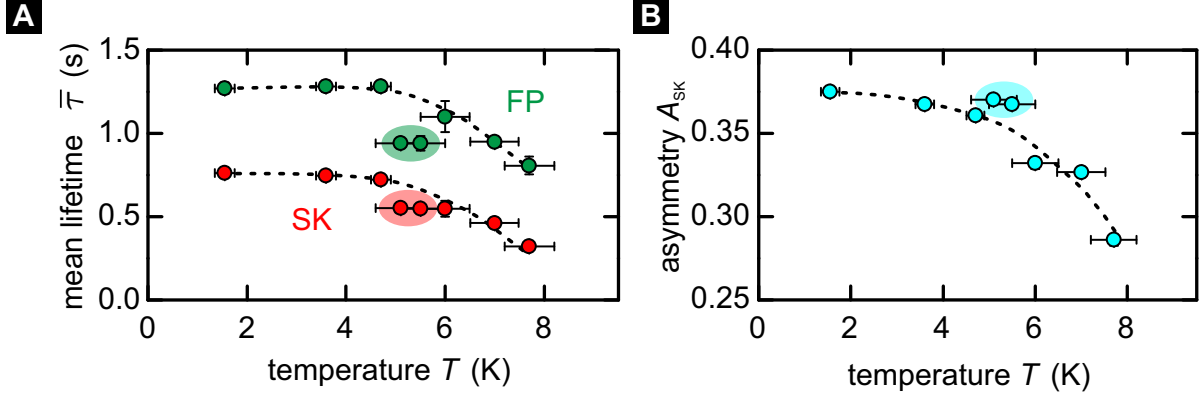


Figure 5.3: A: Temperature dependent mean SK and FP lifetimes obtained by analysis of the telegraph noise signals, which were recorded at the marked position in Fig. 5.2 B. B: Corresponding T -dependent skyrmion asymmetry. The striped black curves indicate general trends in the data ("guide to the eye"), from which the shaded points deviate in all three sets. $I_T = 10$ nA, $U = 700$ mV, $B = 2.5$ T.

mean lifetime $\overline{\tau_{FP}} = (1.10 \pm 0.09)$ s extracted. The mean SK lifetime $\overline{\tau_{SK}}$ can be extracted from the SK lifetime histogram in the same way.

The calculated mean lifetimes can be utilized to compute additional related physical quantities, the transition rates and the skyrmion asymmetry. The transition rates represent the average number of SK \rightarrow FP (skyrmion annihilation) resp. FP \rightarrow SK (skyrmion creation) events per time unit: $\nu_{ANNIHILATION} = \overline{\tau_{SK}}^{-1}$ and $\nu_{CREATION} = \overline{\tau_{FP}}^{-1}$. The skyrmion asymmetry represents the proportion of time spent in the SK state compared to the total measurement time $A_{SK} = \frac{\overline{\tau_{SK}}}{\overline{\tau_{SK}} + \overline{\tau_{FP}}}$ and ranges from 0 (always FP) to 1 (always SK).

To investigate possible thermal effects on the skyrmion annihilation and creation dynamics, the telegraph noise signal was recorded at different temperatures between $T = 1.55$ K and $T = 7.7$ K at the same switching site marked by the tip in Fig. 5.2 B while warming up the empty 1K-pot and subsequently analyzed with the method described above. The resulting mean lifetimes are displayed in Fig. 5.3 A. Both SK and FP lifetimes show a similar behavior: At low temperature, they remain rather constant, followed by a significant decrease, starting at roughly 4 K. Additionally, $\overline{\tau_{FP}}$ is higher than $\overline{\tau_{SK}}$ over the whole investigated range, indicating a lower stability of the SK state compared to the FP state at the chosen magnetic field $B = 2.5$ T. In Fig. 5.3 B, the skyrmion asymmetry is displayed, which shows a trend to decrease with increasing temperature. This is equivalent to the system's preferred state moving closer to FP. Obviously, the thermal behavior of the SK and FP states at the investigated position is not the same. In all three data rows, the data points marked by the ellipses deviate significantly from the observed trends.

To compare the experimental data to the telegraph noise data from [10] and the Arrhenius model of thermal activation from [24], which are both described in Sec. 2.3.2, the transition rates ν_i between the SK and FP states are examined. Within the harmonic approximation of transition state theory, the skyrmion annihilation and creation rates can be described by an Arrhenius equation like Eq. 2.6, which is typically linearized by plotting the transition rates ν_i on a logarithmic scale against the inverse temperature T^{-1} on a linear scale. This is called an Arrhenius plot and can be described mathematically as

$$\nu_i = \nu_{0,i} \exp\left(\frac{-E_{b,i}}{k_B T}\right) \quad (5.1)$$

$$\ln \nu_i = \ln \nu_{0,i} - \frac{E_{b,i}}{k_B} \frac{1}{T}. \quad (5.2)$$

The energy barriers $E_{b,i}$ and attempt frequencies $\nu_{0,i}$ can then be computed from the slope and intercept of the linear function Eq. 5.2.

The Arrhenius plot of the experimentally obtained transition rates ν_i between the SK and FP states is shown in Fig. 5.4. The data points clearly do not follow a linear slope, instead they can be described by a constant rate at high T^{-1} (low T), which increases with decreasing T^{-1} (increasing T). Therefore, Eq. 5.1 alone is not sufficient to match the data and the underlying model has to be extended.

In [10], thermal contributions to the transition rate were ruled out for $T = 4.2$ K and $\nu \approx 3.5$ /s was found for $I_T = 300$ nA, $U = 700$ mV, $B = 2.7$ T at the investigated switching position. The reported linear current dependency of the transition rate can be used to extrapolate the transition rate at $I_T = 10$ nA to $\nu = \frac{10 \text{ nA}}{300 \text{ nA}} 3.5$ /s ≈ 0.1 /s, around one order of magnitude smaller than the experimentally obtained transition rates at similar temperature in Fig. 5.4. This deviation is consistent with the observed transition rate variation of two to three orders of magnitude for different switching positions at otherwise constant conditions in [25].

In contrast to the proposed non-thermal switching in [10], the transition rates found in this study (Fig. 5.4) strongly indicate a temperature dependency, which clearly does not follow the Arrhenius law (Eq. 5.2). Both concepts of temperature-independent and temperature-dependent contributions to the transition rates can be considered simultaneously by using a combined ansatz, which is structurally identical to Matthiessen's rule of phonon scattering, where the total scattering time is approximated by an inverted sum of the inverse partial scattering times of its different contributions. Transferred to the case of SK-FP transitions, the ansatz for the total mean lifetime and corresponding transition rates can then be written as

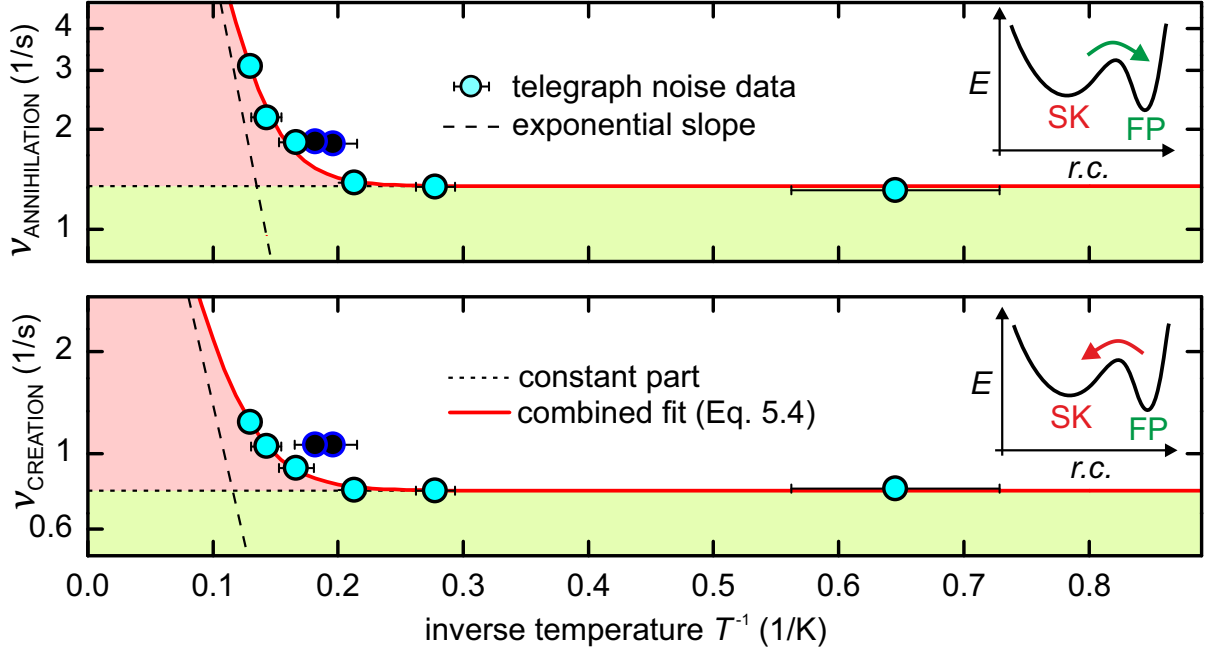


Figure 5.4: Arrhenius plot of mean skyrmion creation and annihilation rates derived from the telegraph noise signal acquired at the position indicated in Fig.5.2 B. Vertical error bars are smaller than the symbols. Constant and exponential part of the fit function shaded in green and red. Black data points not included in the fit. Inserts: Sketch of the potential landscape, transition direction indicated by arrows. $I_T = 10$ nA, $U = 700$ mV, $B = 2.5$ T.

$$\bar{\tau}_i = \left(\frac{1}{\tau_{C,i}} + \frac{1}{\tau_{th,i}} \right)^{-1} \Leftrightarrow \nu_i = \nu_{C,i} + \nu_{th,i}, \quad (5.3)$$

with the respective constant non-thermal and variable thermal partial transition rates $\nu_{C,i}$ and $\nu_{th,i}$. Substituting $\nu_{th,i}$ with the right side of Eq. 5.1 yields

$$\nu_i = \nu_{C,i} + \nu_{0,i} \exp\left(\frac{-E_{b,i}}{k_B T}\right), \quad (5.4)$$

which was subsequently fitted to the experimental transition rates in Fig. 5.4 A and B. Due to the deviant behavior of the shaded data points in Fig. 5.3 A and B, their corresponding transition rate data points were excluded from the fit. The functions with optimum fit parameters (Tab. 5.1) are shown as the red curves in Fig. 5.4, and the model provides a good match to the transition rate data points for the annihilation and creation cases. In the low temperature limit ($T^{-1} \rightarrow \infty$), the total transition rates become equivalent to the non-thermal contribution $\nu_i \sim \nu_{C,i}$ and remain constant. This part of the function is represented by the dotted lines and areas shaded in green in Fig. 5.4 and provides the offset for the thermally dependent part of Eq.

5.4, which itself is represented by the areas shaded in red. Its exponential slope is represented by the striped lines. In the high temperature limit ($T^{-1} \rightarrow 0$), the total transition rate is equivalent to the sum of non-thermal transition rate and thermal attempt frequency $\nu_i \sim \nu_{C,i} + \nu_{0,i}$. The crossing point of the striped and dotted lines is the temperature, where non-thermal and thermal parts are of the same size and contribute equally to the total transition rates. For both Fig. 5.4 A and B, the leftmost (highest T) data points are close to the crossing points, therefore the upper temperature of the measurement series is located in the crossover region of both model regimes.

Table 5.1: Optimum fit parameters of Eq. 5.4 for Fig. 5.4 with their standard regression uncertainties.

Transition	ν_C (1/s)	ν_0 (1/s)	$E_{b,i}$ (meV)
creation	0.78 ± 0.01	60 ± 30	3.2 ± 0.3
annihilation	1.35 ± 0.07	500 ± 600	3.8 ± 0.8

This observation is reflected by the high relative regression uncertainty of the attempt frequencies $\nu_{0,i}$, which are determined by the extrapolated intercepts of the fitting functions. For a set of similar fitting functions with slightly different exponential slopes, which all describe the data points in the crossover region well, its value varies strongly due to the mutual interdependency of the fit parameters $\nu_{0,i}$ and $E_{b,i}$. The uncertainty should be reducible by extending the measurement range to higher temperatures, which probably leads to an increase of the transition rates. Data obtained by such an experiment would be able to better map the exponential part of Eq. 5.4 and increase the validity of the obtained physical parameters.

The experimentally obtained energy barriers are significantly smaller than $E_b \approx 80$ meV for SK creation and $E_b \approx 35 - 50$ meV for SK annihilation from [24]. The difference could, of course, be caused by the insufficient mapping of the assumed Arrhenius behavior, but may also result from the aforementioned variation of transition rates and energetic stability for skyrmions in different local environments. Here, a systematic study for many skyrmion switching positions could help to isolate the environmental influence.

To summarize, indications for a temperature dependence were found in the skyrmion creation and annihilation dynamics, which could be described by a combined model of non-thermal and thermal contributions to the transition rates between the SK and FP states. A T -dependent increase in the transition rates at constant U and I indicates, that local heating of the sample by the tunneling current is not a determining factor, as the injected power UI remained constant during the experiment. Instead, thermal excitation of the creation and annihilation via increased sample temperature is sufficient to explain the observations.

5.3 The ordered phases at elevated temperature

5.3.1 Spin spiral, skyrmion and field-polarized phase at $T \approx 40$ K

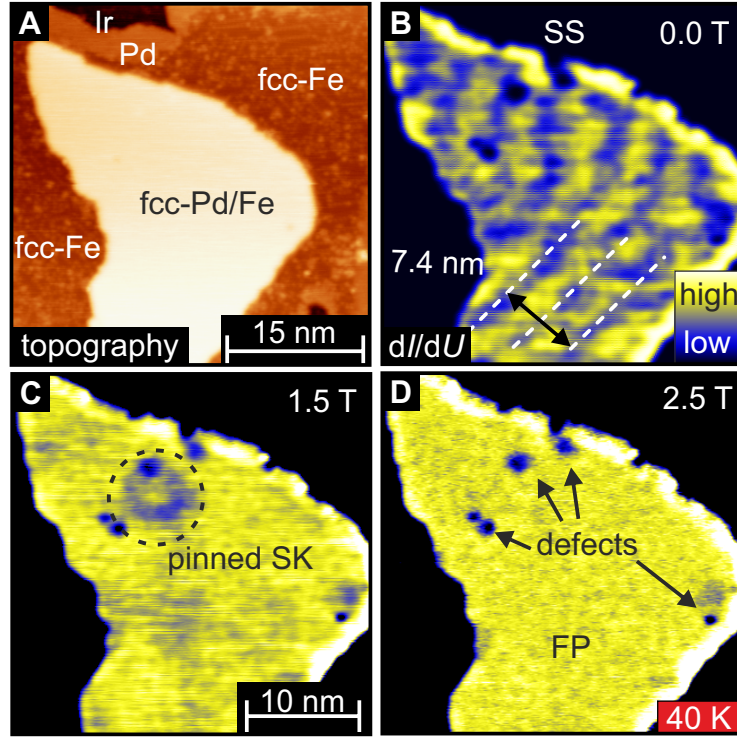


Figure 5.5: The ordered magnetic phases of fcc-Pd/Fe/Ir(111) at $T = 40$ K. A: Constant current topography of a Pd/Fe nanoisland. B,C,D: Simultaneously obtained dI/dU -maps. A: Spin spiral phase on the whole nanisland. B: A single ring-shaped skyrmion pinned to a defect in field-polarized background. C: Completely field-polarized island. All images: $I_T = 1$ nA, $U = 700$ mV.

Fig. 5.5 shows a fcc-Pd/Fe nanoisland topography (A) with corresponding dI/dU maps for different magnetic fields (B-D) at a sample temperature $T = 40$ K. At zero field, the spin spiral can be clearly identified in Fig. 5.5 B due to its matching appearance with the SS at $T = 2.1$ K in the right part of Fig. 5.1 A. The length of two periods in dI/dU variation $d \approx 7.4$ nm, which is equal to the magnetic period of the SS, is comparable to the observed length of $d \approx 7.0$ nm at $T = 2.1$ K, $d \approx 7.4$ nm at $T = 2$ K and $d \approx 7.0$ nm at $T = 50$ K from [45], and $d \approx 7$ nm from [10] and [11].

With increasing field, the spin spiral is substituted by a skyrmion, which appears ring-shaped in Fig. 5.5 C, similar to the skyrmions observed at $T = 1.8$ K in Fig. 5.1 B. At even higher magnetic field, the skyrmion vanishes, leaving a nanoisland with uniform dI/dU signal intensity

(Fig. 5.5 D) corresponding to the field-polarized state. The remaining dark spots in the dI/dU maps are caused by the aforementioned in-layer defects, which can serve as pinning centers for skyrmions.

5.3.2 Skyrmion movement and contrast changes

So far, the appearance of the low temperature ordered phases could be reproduced at elevated temperature. But a closer look at Fig. 5.5 C reveals additional dark sites apart from the skyrmion and the defects. The cause for the dark areas, of which one is highlighted in Fig. 5.6 C, appears to be temperature induced skyrmion movement. The authors of [51] used the same fcc-Pd/Fe nanoisland as a template for micromagnetic simulations in confined geometries. In the simulation, all sites on the island are energetically equal, except for a single impurity modeled by a fixed atomic spin pointing parallel to the sample surface and to the right of the image. Magnetic interactions were modeled with an effective magnetic field representing the Hamiltonian in Eqn. 2.1 - 2.4, with material parameters extracted from the experimental skyrmion profiles in [23]. Fig. 5.6 A shows the temporal evolution of the island at simulated $T = 25$ K, each image consists of a time frozen snapshot of the spin configuration, with grayscale coding of the z-component of the local magnetization m_z . While the skyrmion on the top left of the island rapidly changes its shape between the images taken at 5, 10 and 20 ns, its position remains the same due to the strong pinning to the simulated impurity. Conversely, the other four skyrmions inside the island are freely changing positions in the right part of the island due to the absence of strong pinning locations. Their movement is confined to the center of the island by SK-SK and SK-edge repulsive interactions [51].

The simulated time scale in the order of nanoseconds is not accessible by the experimental setup used in this thesis. The experimental time resolution is limited by the lock-in amplifier integration time of 3 ms which is several orders of magnitude higher than the time scale for the skyrmion dynamics. Therefore, the individual skyrmion movements cannot be observed in the experimental dI/dU map shown in Fig. 5.6 C.

Instead, a much better consistence between experiment and theory is achieved in Fig. 5.6 B, where a 20 ns average of all individual simulation snapshots is displayed. Here, the movement of the mobile skyrmions blurs to a diffuse region with m_z lower than the surrounding field-polarized regions. The skyrmion pinned to the artificial defect now appears as a round shaped object similar to Fig. 3.5 B. Apart from the ring-shape caused by the NCMR imaging mode, the skyrmion in Fig. 5.6 C also deviates from the forced artificial pinning direction due to the

presence of additional defects near the pinning location and no directional constraints at the defect site itself.

To further compare Fig. 5.6 B to C, the lower part of the images shows profiles along the red, striped arrows, representing the change in z -magnetization resp. relative dI/dU intensity along the pinned SK^P and mobile SK^M skyrmion sites.

Both profiles start at a FP area, characterized by high dI/dU resp. high positive m_z , then continue through the pinned skyrmion SK^P marked by the dI/dU double-dip resp. negative m_z to another FP area. The following, right part of the profile consists mostly of the SK^M area, where dI/dU intensity and m_z are lower than their values for FP, but higher than their corresponding SK^P values. The observed decrease in signal intensity depends on the ratio of skyrmion occupation time to total measurement time at the investigated spot, which is equivalent to the skyrmion asymmetry A_{SK} . A high dip in intensity results from a high skyrmion dwell ratio relative to its absence. Conversely, a low dip in intensity results from a low skyrmion dwell ratio. In the extreme cases of 100% SK or 0% SK, the signal converges to the values for SK and FP at low temperature.

The good agreement between experimental data and micromagnetic simulations leads to an updated interpretation of the physical spin configuration behind the dI/dU maps at elevated temperature: According to Sec. 3.5, NCMR imaging is not sensitive to the sample spin orientation relative to the tip but rather the angle between the investigated spin and its neighbors. Therefore, dI/dU maps acquired with this technique only show the local non-collinearity or spin canting of the magnetic structures like spin spirals or skyrmions in the sample. By including the findings at elevated temperature, the dI/dU maps now additionally contain a time-averaged skyrmion probability which modulates the static structure intensities, effectively generating maps of skyrmion probability density.

5.3. The ordered phases at elevated temperature

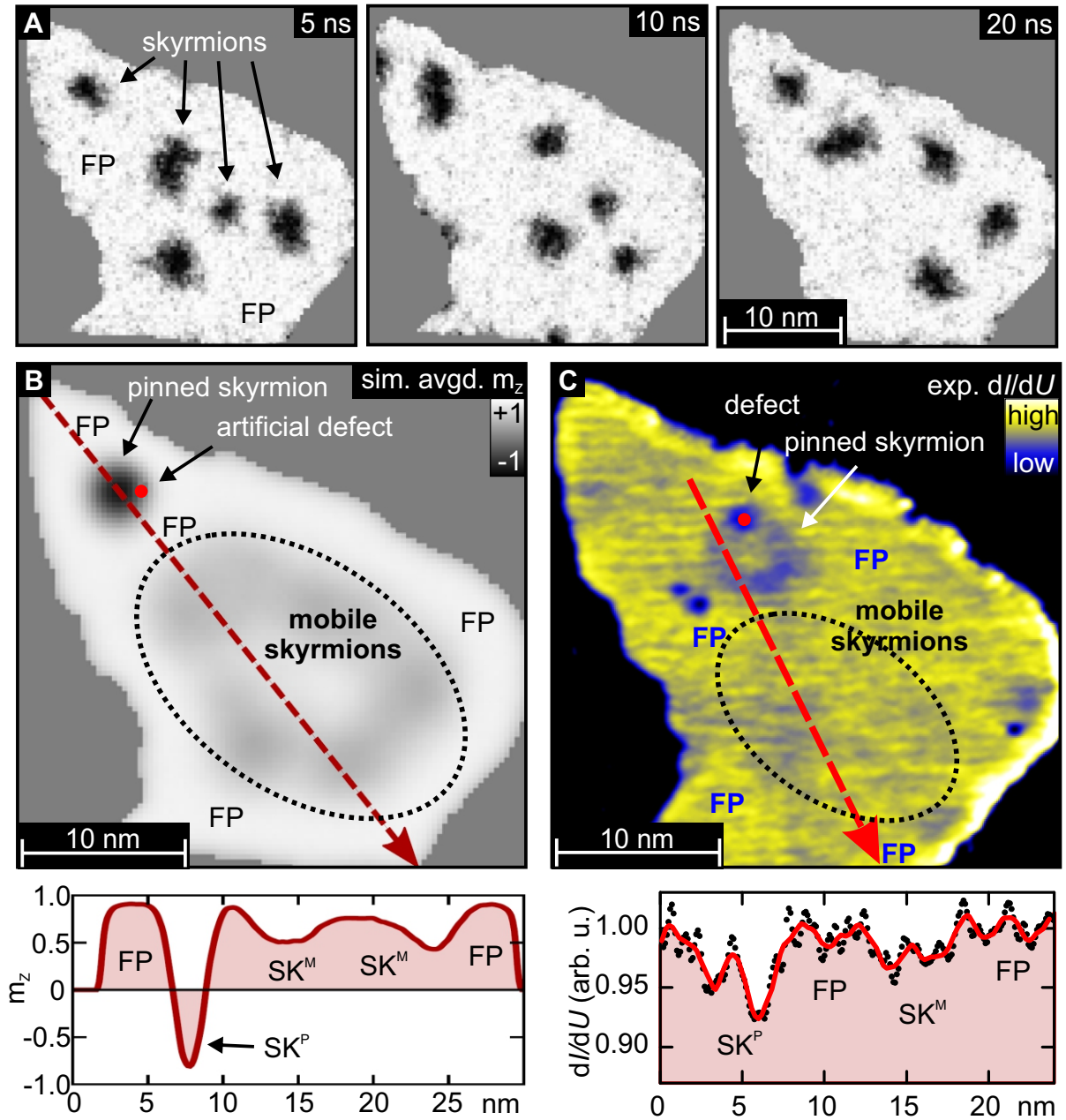


Figure 5.6: Effects of skyrmion movement. A: Temporal evolution of several skyrmions in the field polarized (FP) background of a fcc-Pd/Fe nanoisland, computed by micromagnetic simulation in [51]. The z component of the local magnetization m_z is greyscale coded. B: 20 ns time-average of the simulation. C: Experimental dI/dU map of the island used as motivation for the simulation. Bottom row: profiles corresponding to the red arrows in C and D. A,B: $T = 25$ K, $B = 1.5$ T. C: $I_T = 1$ nA, $U = 700$ mV, $T = 40$ K, $B = 1.5$ T. A and B adapted from [51], licensed under CC-BY-4.0.

5.3.3 Thermal stability of the ordered phases

Fig. 5.7 shows magnetic field dependent dI/dU maps of a fcc-Pd/Fe nanoisland at $T = 78$ K. At zero magnetic field, indications for the spin spiral phase, characterized by a typical period length of $d \approx 7.5$ nm, are found in Fig. 5.7 A and marked by the dotted lines in the lower half of the nanoisland. On the upper half of the island, patterns with different characteristics arise, which cannot be described as a spin spiral due to the lack of a repeating period. At $B = 1.5$ T, the observed structures deviate strongly from the zero-field structures. The island now contains two roughly circular dark objects, which are marked by the striped circles in the middle of Fig. 5.7 B. Additionally, dark structures with asymmetric shape, but higher dI/dU than the circular structure, are found at the upper and lower part of the island, replacing the SS and irregular structures found at zero field. Between the dark structures and near the edge of the island, a more uniform high dI/dU signal is found. At the maximum available magnetic field $B = 3.0$ T, the dI/dU signal appears uniformly high for the whole island, except for some areas with slightly darker structures.

Based on the comparison of the experimental dI/dU map with the time-dependent simulation in the last section, the observed features at $T = 78$ K can be interpreted: The round dark objects in the middle of the island at $B = 1.5$ T would correspond to positions with high SK probability (SK^H), while the less dark, irregularly shaped objects would correspond to areas with medium skyrmion probability (SK^M). Similar to the simulation, the structures seem to avoid the islands edges, leading to a vanishing SK probability at these regions, which is equivalent to the FP state. To justify this interpretation, one of the circular objects is investigated in detail: Fig. 5.8 A shows zoomed-in dI/dU -maps of the structure marked by the right circle in Fig. 5.7 B at different magnetic fields. The dI/dU -maps are normalized to the area around the bottom "FP" marker in Fig. 5.7 B for each individual B value and show a general shrinking of the dark area with increasing magnetic field. Additionally, the distribution of relatively darker and brighter locations inside the structure changes with the field, too. At $B = 1.0$ T, the lowest normalized dI/dU value is not found in the center, but roughly midway from the center to the rim, while the lowest values are found at the center for $B = 2.5$ T. This behavior resembles the ring-to-disk shape change of skyrmions under NCMR imaging conditions. For $B = 3.0$ T, some irregular, faint structures remain at the position. As the fine structure of the object is superimposed with noise, a radial average was chosen to minimize its influence on the profile through its diameter. The obtained radial profiles are displayed in the row below the dI/dU -maps in Fig. 5.8 A: For $B = 1.0 - 2.0$ T, the lowest dI/dU values are found off center of the object, and for $B = 2.5$ T, at the center. The profiles were fitted with the NCMR skyrmion profile function given by Eq.

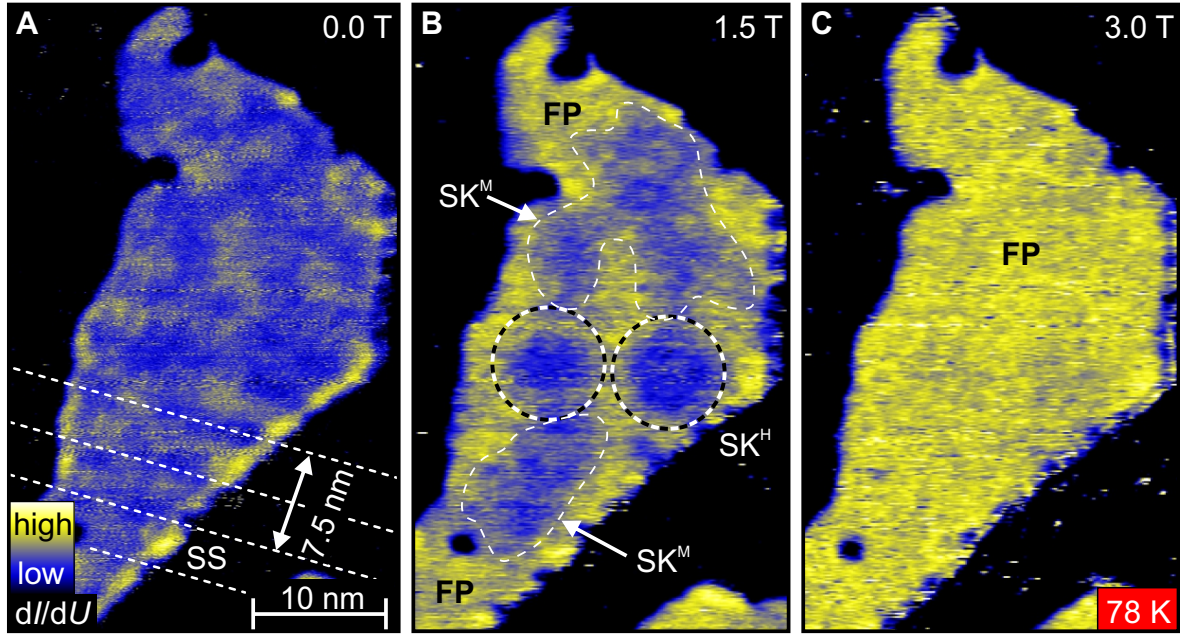


Figure 5.7: Magnetic field dependent dI/dU maps of a fcc-Pd/Fe nanoisland at $T = 78$ K. A: Indications for the spin spiral state are found in the lower part, marked by the striped lines. The upper part contains irregular structures. B: Bright areas arise, indicating field-polarized regions. Dark spots of high SK probability (SK^H) are visible, marked by the striped circles. Also, irregularly shaped spots of medium SK probability (SK^M) thread through the FP areas. C: Uniform dI/dU intensity in the field polarized state. Color scale adjusted individually for each image. $I_T = 1$ nA, $U = 700$ mV.

4.4 in section 4.6, with skyrmion center position x_0 set to zero due to the radial profile and FP dI/dU -intensity y_0 set to 1 due to the normalization. The fitted curves (red in Fig. 5.8 A) reproduce the shape of the radial profiles for $B = 1.0 - 2.5$ T.

The successfully fitted functions can be used to extract the magnetic field dependent skyrmion diameter D and wall width w , which are displayed in Fig. 5.8 B. Standard relative regression uncertainties for D and w are below 5 % for all data points. The skyrmion diameter decreases from $D \approx 4.3$ nm at 1.0 T to $D \approx 2.8$ nm at 2.5 T, which is close to the reported decrease from $D \approx 4$ nm to $D \approx 2$ nm obtained from TMR-based profiles at similar magnetic fields in [23]. The extracted wall widths w in Fig. 5.8 B do not show a strong B -dependency, in qualitative agreement with the results from [23]. Therefore, the investigated structure has properties similar to a skyrmion.

A significant difference to the skyrmions found at low temperature remains: a relatively low dI/dU contrast. The scaling factor $C \approx 0.03$ from the skyrmion profile at $B = 1.5$ T in Fig. 5.8 A significantly deviates from $C \approx 0.11$, obtained by similar analysis of the skyrmion profile in

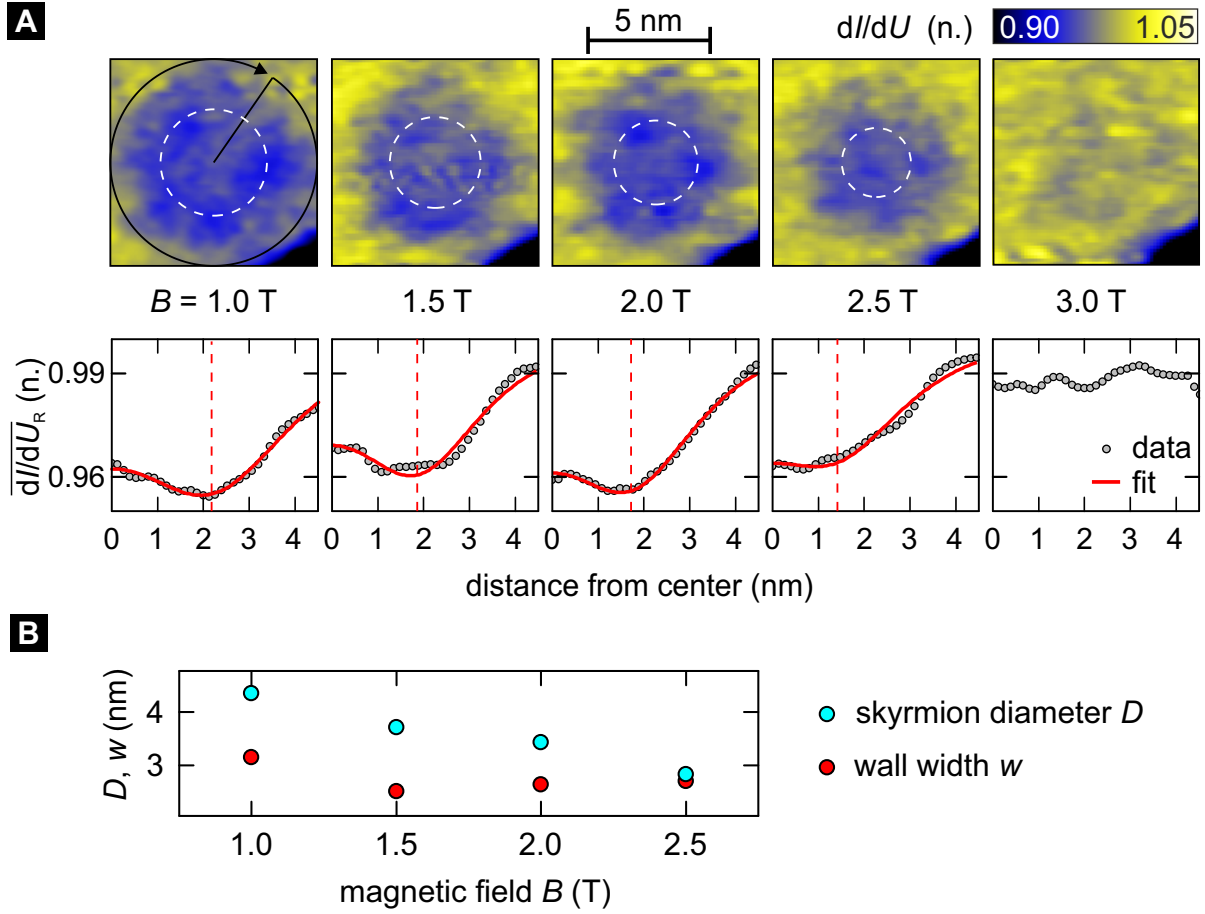


Figure 5.8: A: Zoom-ins of the right skyrmion position from Fig. 5.7 B at different magnetic fields and corresponding radially averaged profiles with NCMR fit. Striped white circles indicate the skyrmion diameter obtained from the fit, the corresponding radii are marked by red striped vertical lines in the profiles. dI/dU signal normalized to the area around the bottom "FP" marker in Fig. 5.7 B. B: Magnetic field dependent skyrmion wall width and diameter extracted from the NCMR fits in A. $I_T = 1$ nA, $U = 700$ mV, $T = 78$ K.

Fig. 4.8, which was recorded at $T = 1.2$ K and $B = 1.5$ T. C is a measure for the relative dI/dU difference between SK and FP states, therefore the statement of the last sentence is equivalent to a decrease in contrast between SK and FP by a factor of at least 3 at $T = 78$ K relative to the contrast at $T = 1.2$ K. The difference is likely caused by the already discussed time-averaging effect, which incorporates the SK asymmetry in the observed dI/dU signal intensity.

The presented measurements in this section were performed at the highest temperature, at which characteristic features of the spin spiral, skyrmion or the field-polarized state were found.

5.4 Observation of disordered structures

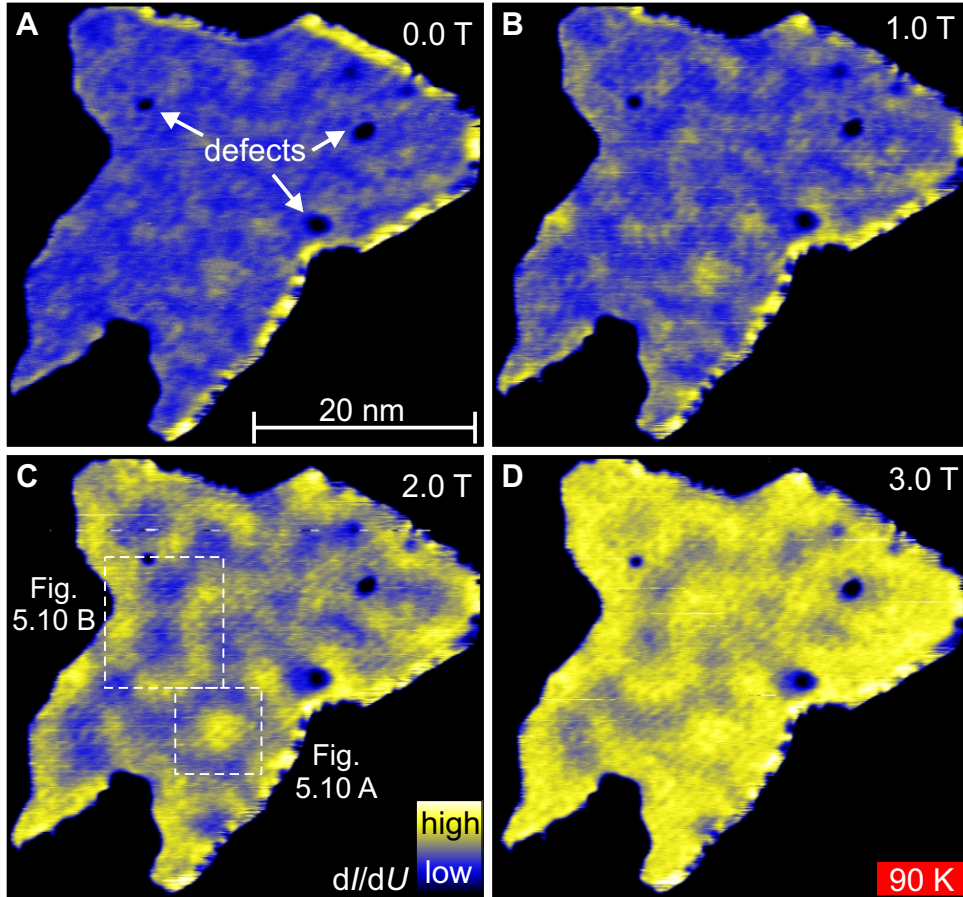


Figure 5.9: Magnetic field dependent dI/dU maps of a fcc-Pd/Fe nanoisland at $T = 90$ K. The small period pattern along the diagonal direction results from mechanical noise. The very dark spots inside the island are caused by defects. Image color scale corresponds to the same dI/dU range for A-D. $I_T = 1$ nA, $U = 700$ mV.

For $T > 78$ K, the observed structures deviate significantly from the previous observations. Fig. 5.9 shows a dI/dU map series of a fcc-Pd/Fe nanoisland at $T = 90$ K. The island contains three very dark spots, as marked by the white arrows in Fig. 5.9 A, which are likely caused by the already mentioned typical in-layer defects of the surface Pd layer. Apart from the defects, an irregular fine structure, consisting of alternating areas of low (blue, dark) and high (yellow, bright) dI/dU intensity with varying size and shape is found on the island. By comparison of the dI/dU maps A-D, which were recorded at different magnetic fields, an overall increase in dI/dU signal intensity with B is found. The increase does not occur uniformly for the whole nanoisland, but seems to start at certain bright spots with no obvious, regular arrangement (Fig. 5.9 B).

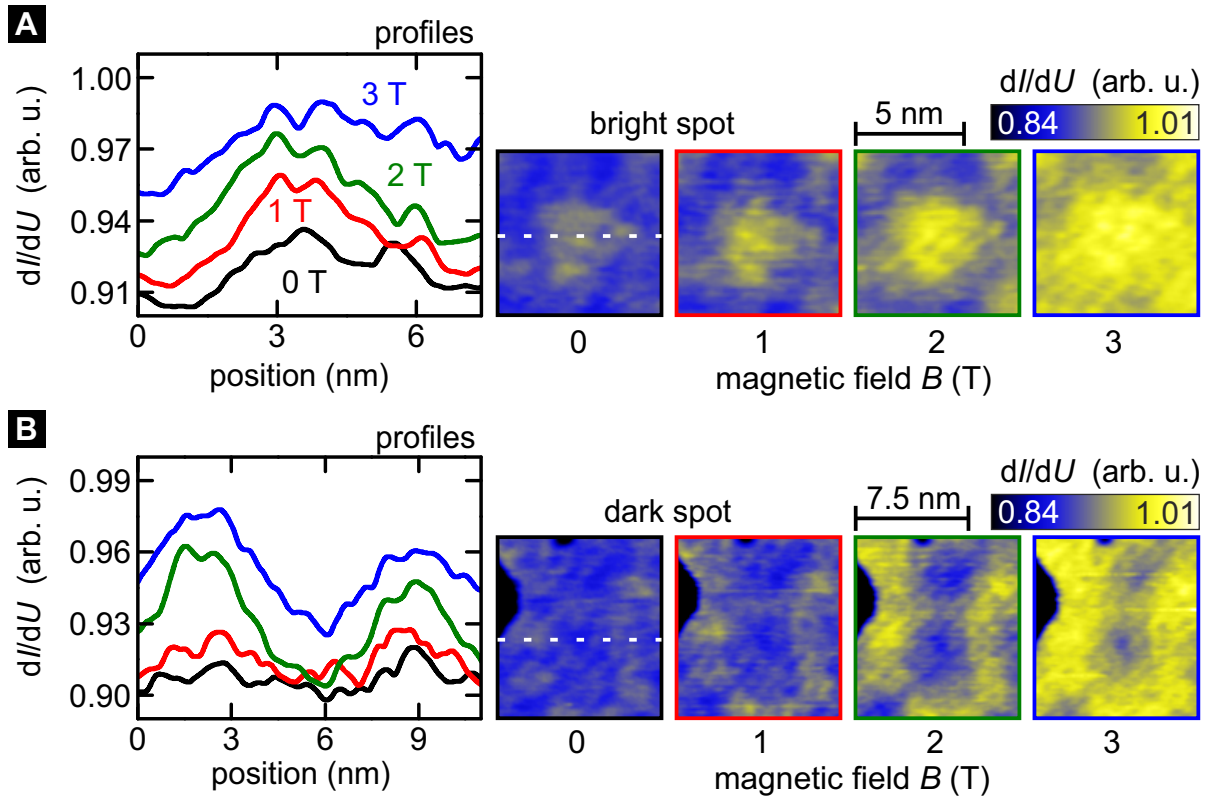


Figure 5.10: A: Zoom-ins of the bright spot marked in Fig. 5.9 and corresponding profiles along the white striped line. B: Zoom-ins of the dark spot marked in Fig. 5.9 and corresponding profiles along the white striped line. $I_T = 1$ nA, $U = 700$ mV.

Further increased B leads to stronger segregation of bright and dark structures: The former are concentrated mostly near the island's edge and at certain positions in the center, while the latter mostly avoid the edge and group at the center (Fig. 5.9 C). At the instrumental high field-limit $B = 3.0$ T, dark structures remain at the center of the island and less variations in dI/dU signal intensity are still found at the bright areas (Fig. 5.9 D).

Zoom-ins on the bright and dark spots marked in Fig. 5.9 C and dI/dU profiles through their centers are displayed in Fig. 5.10. Here, the difference in magnetic field dependent behavior between them becomes more pronounced than in the overview maps. The bright spot (Fig. 5.10A) increases in dI/dU intensity with increasing B , and the center position of the profile curves in the left part of the image shows a regular increase in dI/dU intensity between the magnetic field steps.

The dark spots behavior, as displayed in Fig. 5.10 B, is different. Profiles along the striped white line show, that the dI/dU intensity at its center remains rather constant for $B = 0.0, 1.0$ and 2.0 T, and increases from 2.0 T to 3.0 T. The bright areas adjacent to the dark spot (left

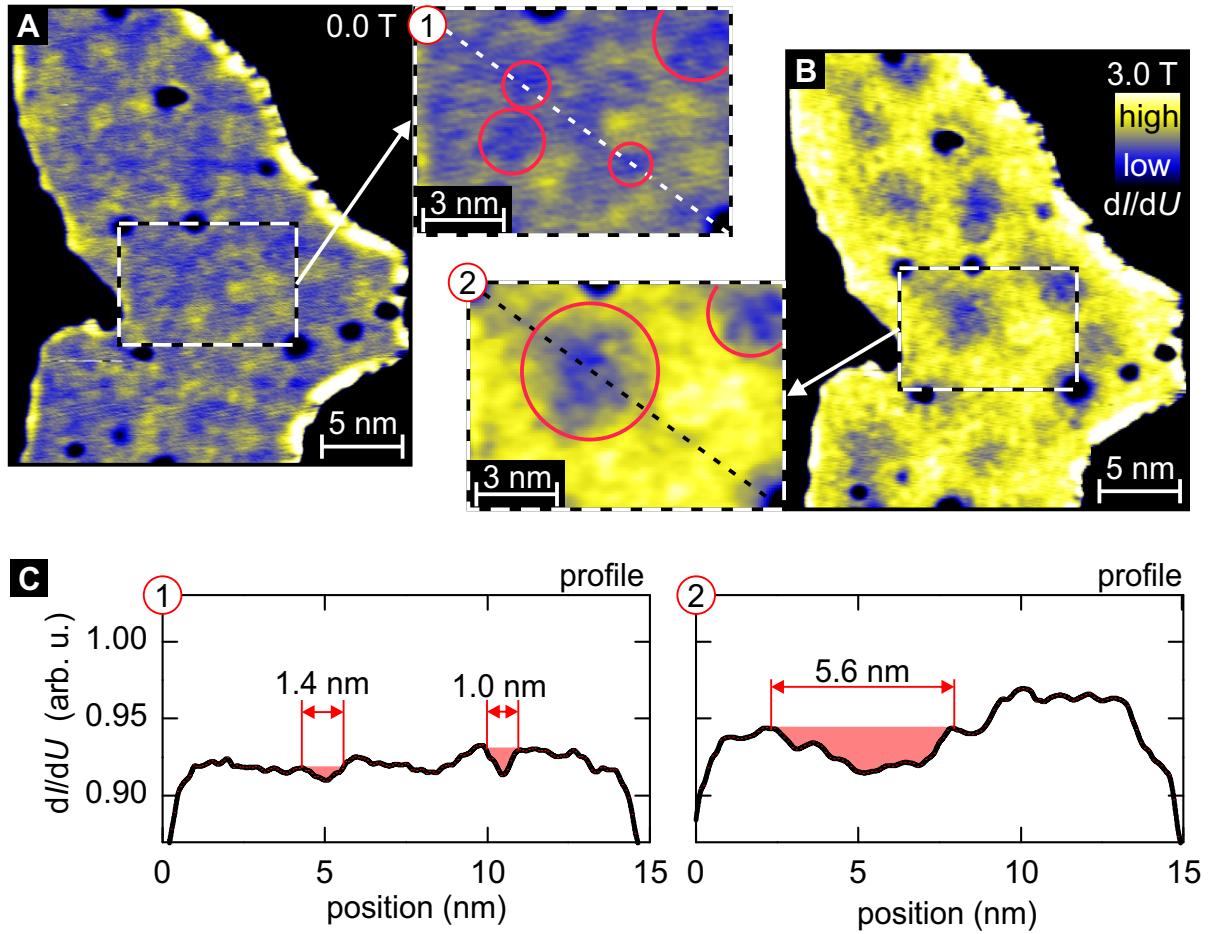


Figure 5.11: A,B: dI/dU maps of a fcc-Pd/Fe nanoisland at $T = 95$ K. Small images: Zoom-ins of the striped rectangles, some dark spots are highlighted with red circles. C: Profiles through the zoom-ins of A and B along the striped lines. Length scales of the dark spots indicated by the red shaded areas. Image color scale corresponds to the same dI/dU range for A,B. $I_T = 1$ nA, $U = 700$ mV.

and right side of the profile), start to increase in dI/dU intensity at the first B step, similar to the bright spot in Fig. 5.10 A.

Fig. 5.11 shows dI/dU maps of a nanoisland for $B = 0.0$ T (A) and $B = 3.0$ T (B), recorded at $T = 95$ K. The individual observations of overall brightness increase and non-uniform local brightness can be found for the displayed structures, too. At the zoomed-in areas, different sizes of the dark spots are marked by red circles. At zero field, the structure size is small, and a lot of fine dark and bright spots are found. At high field, the dark structures condense to few, but bigger dark spots. Profiles along the striped lines are shown in Fig. 5.11 C, and dips in the dI/dU intensity correspond to the dark spots. The zero field structures are not only smaller than the high field structures, but also consist of less dI/dU variation along the profile line.

To summarize the observations, the investigated structures in the dI/dU maps of the fcc-Pd/Fe nanoislands show three distinct effects with increasing magnetic field: First, the overall dI/dU intensity of the nanoislands increases. Second, the local dI/dU intensity of bright areas increases faster than for dark areas. Third, the characteristic feature size increases. Additionally, the dI/dU intensity of the island is not uniform at the maximum achievable $B = 3.0$ T.

An interpretation of these observations can be given, if an NCMR-dominated imaging mechanism is assumed and applied to the irregular structures. This assumption can not be proven explicitly due to the unknown spin structure of the investigated objects, but is probable due to the good agreement of the skyrmion, spin spiral and field-polarized surface features at up to $T = 78$ K with their known appearance in low-temperature NCMR-images. A low dI/dU intensity would then indicate a low local collinearity, *i.e.* high average angle between the neighboring magnetic moments. Conversely, a high dI/dU intensity would indicate a high local collinearity or small average angle between the neighbors. Transferred to the consistently used color scheme of the dI/dU -maps in this study, bright (yellow) areas indicate higher local collinearity than dark (blue) areas.

Based on the previous considerations, the following statements about the observed structures can be derived:

1. Sensitivity to changes in the applied magnetic field indicates a magnetic origin.
2. The structures are spatially non-uniform at all investigated magnetic fields, therefore the underlying spin structure has to be spatially non-uniform, too. This especially excludes the presence of a fully field-polarized configuration, which would lead to a uniform dI/dU intensity.
3. They are generally driven to a more collinear configuration by the magnetic field, indicated by the overall increase in dI/dU signal intensity. This is energetically favorable only for a spin configuration, which gradually aligns to the field. Therefore, the spin configuration of the island is approaching the FP state, but has not reached it yet at $B = 3.0$ T.
4. This approach is conducted unevenly at different areas of the island: As a first step, the filigree fine structure is compressed to bigger non-collinear patches, while the remaining areas start to align to the external field. The bigger patches remain in a highly non-collinear state and start to align to the external field at higher B . This is reflected by the increased contrast between dark and bright areas at $B = 2.0$ T, compared to the 0.0 T and 3.0 T structures.

5.4. Observation of disordered structures

5. The structures contain neither regular periods (indicator for the spin spiral) nor rotationally symmetric objects of low collinearity (indicator for skyrmions), therefore no indications for SS and SK based structures can be derived from the observations.

The experimentally obtained dI/dU maps at $B \geq 2.0$ T bear a strong resemblance to the simulated spin configuration of the fluctuation-disordered phase from [28], which is shown in Fig. 2.7. Both consist of patches of non-collinear spins with similarly irregular shapes and sizes in a more collinear background, which is aligned to the external magnetic field.

Due to the similarities with the fluctuation-disordered state and the absence of indications for ordered structures like SS, SK and FP in the dI/dU maps, the structures found for $T > 78$ K are labeled as a disordered state.

The exact nature of the constituting objects cannot be determined by the experimental approach used in this study due to the averaging effect of the limited time resolution. An experimental technique to differentiate between possible static and dynamically fluctuating spin configurations in the island would need to combine sub-nanometer spatial resolution with simultaneous nanosecond time resolution.

5.5 The thermomagnetic phase diagram

A thermomagnetic phase diagram visualizes the observed magnetic phases as a function of temperature T and magnetic field \mathbf{B} . While the magnetic field perpendicular to the sample plane B and the STM temperature T are clearly defined quantities, which can be adjusted within the safe operational limits of the cryomagnet system, the observed "phase" depends on the interpretation of the structures found in the dI/dU maps at variable B and T . Therefore, consistent criteria were used:

Spin spiral: The dI/dU -maps contain regular stripe patterns within the Pd/Fe nanoislands which correspond to the spin spiral wavelength of ≈ 7 nm [10]. A typical example for the SS is found in Fig. 5.5 B.

Field-polarized: The dI/dU -maps show a uniform dI/dU -level on significant parts of the Pd/Fe nanoisland. A typical example for the FP state is found in Fig. 5.5 D.

Skyrmions: The dI/dU -maps contain dark objects with unique skyrmion properties such as rotational symmetry or ring-shape at low magnetic fields. A typical example for a skyrmion is the ring-shaped object in Fig. 5.5 C.

Disordered: The dI/dU -maps contain B -sensitive structures which can not be attributed to SS, SK or FP. A typical example would be Fig. 5.9 A-D.

The experimental phase diagram was mapped within the instrumental limits $0.0 \text{ T} \leq B \leq 3.0 \text{ T}$ and $1.2 \text{ K} \leq T \leq 100 \text{ K}$: The STM temperature was stabilized via PID feedback at the desired elevated T to record magnetic field dependent dI/dU maps of fcc-Pd/Fe nanoislands. The cumulative result of the individual measurements for numerous nanoislands is displayed in Fig. 5.12: each white or red point represents an individual data point, taken at a particular fcc-Pd/Fe nanoisland at defined B and T . The spin spiral, field-polarized and disordered phase were uniquely identified according to the definitions above and are marked by the colored background. Spin spirals were found for $B \leq 1.0 \text{ T}$ and $T < 78 \text{ K}$. Field-polarized spin arrangements were found for $B > 1.0 \text{ T}$ and $T < 78 \text{ K}$. The disordered state was found above the critical temperature $T_C = 78 \text{ K}$ at all available magnetic fields.

Experimentally observed skyrmions in Pd/Fe/Ir(111) occur either in coexistence with the SS, as individual skyrmions in the FP state, or as a loosely connected hexagonal lattice in a field-

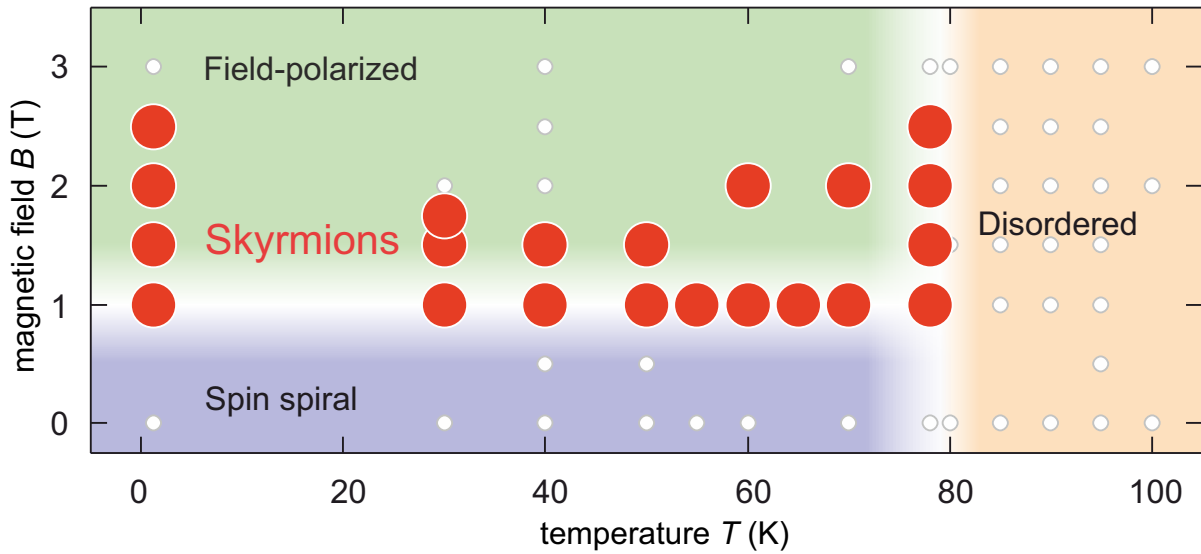


Figure 5.12: Cumulative thermomagnetic phase diagram of the Pd/Fe nanoislands. Every data point represents the phases found for different temperature and magnetic field values. The spin spiral, field-polarized and disordered phases are indicated by the color shaded regions. Red data points indicate the existence of skyrmions within the host phases. $I_T = 1$ nA, $U = 700$ mV.

polarized background [10, 23], depending on the applied perpendicular B . The distinction between the latter sub-phases is blurred by the size restriction of the Pd/Fe nanoislands of the preparation used in this study: If only a small number of skyrmions exists in an island, the difference between individual skyrmions and the loose skyrmion lattice becomes somewhat arbitrary. Therefore, indications for skyrmion occurrence either in stable or rapidly switching form are marked by the red points inside the host phases and found for $1.0 \text{ T} \leq B \leq 2.5 \text{ T}$ and $T < 80 \text{ K}$.

Monte-Carlo simulation based phase diagrams in [28] and [29] are in very good qualitative and quantitative agreement with the experimental results of this thesis. Both are shown in Fig. 5.13 and yield a critical temperature of $T_C = 100 \text{ K}$ resp. $T_C = 81 \text{ K}$ compared to the experimental result of $T_C = 78 \text{ K}$. Both simulated phase diagrams contain a regular skyrmion lattice phase between the low B spin spiral and high B field-polarized phase, which is not found for Pd/Fe nanoislands. Therefore, the concept of a phase boundary between the field-polarized and skyrmion lattice state does not strictly apply here, but the experimental boundary between the skyrmion containing FP phase and SS phase at $B \approx 1.0 \text{ T}$ is reproduced well by both simulated diagrams with $B \approx 1.0 \text{ T}$ and $B \approx 1.5 \text{ T}$.

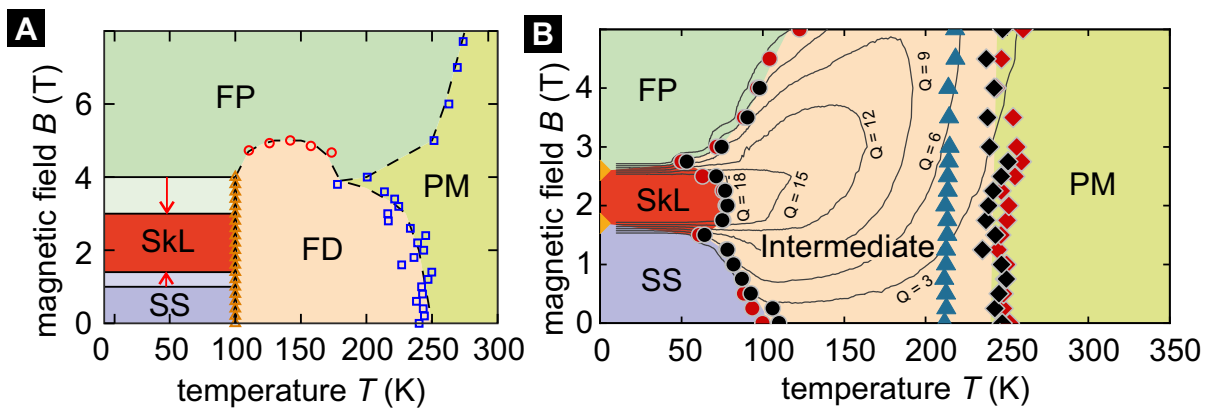


Figure 5.13: Thermomagnetic phase diagrams of fcc-Pd/Fe/Ir(111) obtained by Monte-Carlo simulations. Differently coded symbols represent different methods to obtain the phase boundaries at their locations. A: The faded areas and red arrows between spin spiral (SS), skyrmion lattice (SkL) and field-polarized (FP) phases represent transition regions which could not be resolved by the simulation. PM = paramagnet. Adapted with permission from [28]. Copyright (2016) by the American Physical Society. B: Adapted from [29], licensed under CC-BY-3.0.

Chapter 6

Upgrading an existing multi-probe scanning tunneling microscope

This chapter describes the upgrade of a multi-probe scanning tunneling microscope (MP-STM). It includes several improvements over the original design and consequential function tests.

6.1 Motivation and MP-STM basics

A MP-STM is essentially a STM with multiple scanning tips. The simultaneous application of multiple tunnel junctions or contact electrodes to a sample allows to investigate electron transport via 4-point resistance or potentiometry measurements on various sample surfaces [52–56].

A special class of transport experiments concerns the response of magnetic nanostructures like domain walls [57, 58] or skyrmions [12] to currents applied parallel to the sample surface. If the current density is high enough, the magnetic nanostructures can be manipulated in a controlled fashion which provides essential insights into the physics of interactions of non-collinear spin textures with spin currents.

For a nanoscale transport experiment, at least three individually controlled STM tips are needed: Two outer tips to induce a lateral current by an applied differential voltage and one central tip to image the manipulated magnetic nanostructure. Fig. 6.1 shows the tips of such an experimental setup. The tips L,C and R are glued to individual piezo tube scanners to provide three-dimensional nanopositioning above the sample surface. The side tips L and R can be moved by a coarse approach system in three dimensions to contact the sample S at the desired position and relative angle. The central tip C is then used to image the sample surface. Similar to conventional STM (one tip only), the movement range of the tube scanners is limited to a few

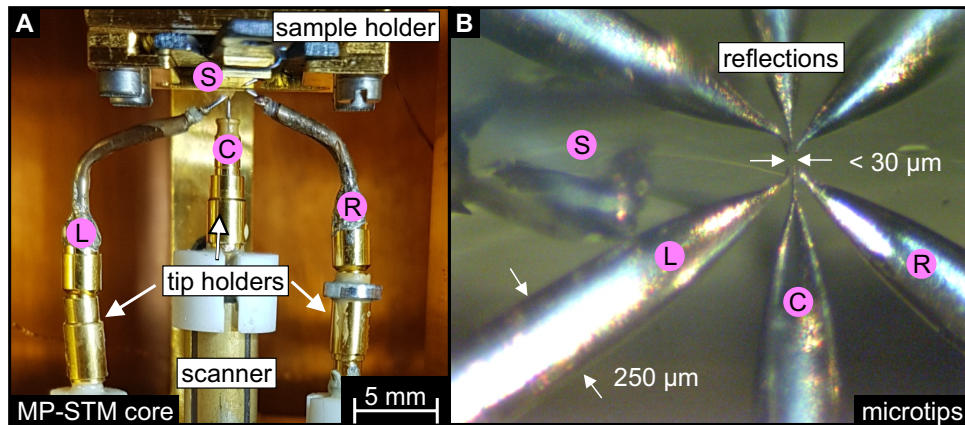


Figure 6.1: A: Core of a MP-STM setup. Tunneling tips L,C and R near the golden sample S. B: Optical micrograph of the microtips in very close proximity to the sample surface S. Top part of the image shows the reflection of the tips on the shiny crystalline gold sample surface.

micrometers. Therefore, they have to be positioned in close proximity to the sample by piezo motors operating via the stick-slip principle. Here, the increased complexity of a multiprobe STM arises: For each tip, a three-dimensional coarse approach has to be constructed. With optical microscope control, the three tips can be brought together to less than $30 \mu\text{m}$ distance between the outer tips. Further approach to the targeted sub-micrometer distance between the tips can be realized by an automated program described in [42].

6.2 State of the MP-STM before upgrade

The three tip STM was designed and constructed by Jonas Harm and a detailed description of its properties and performance evaluation can be found in his Ph.D thesis [44]. It will serve as a replacement for the single tip RF-STM, which was used for the skyrmion experiments in this thesis. Due to the size constraint caused by the magnet's inner bore diameter of just 70 mm in Fig. 4.2, the whole microscope, including all the coarse positioning piezo drives for the side tips and the sample, is restricted to an outer diameter of 60 mm. Therefore, the design is highly integrated.

In [44], the assembled MP-STM was shown to be capable of atomic resolution on HOPG in ambient conditions on an air cushioned table for the central and right scan units in constant-height mode with very fast scan velocities to reduce the impact of mechanical vibration in the tunnel junction. In a room-temperature UHV test chamber with advanced vibration isolation, the monoatomic steps of Au(111) on mica could be resolved with the right and central scanning unit. Using the same microscope, Jonas Koch imaged the characteristic herringbone reconstruction [59] with the central tip at room temperature and UHV in his Master thesis [60]. The monoatomic steps could be resolved at $T = 48$ K with the same setup.

During further development work, the lateral coarse positioning units of the side tips were identified to be the central weak point of the design and hindered further testing. Fig. 6.2 shows the complete nano and coarse positioning unit for one of the side tips. The tip is glued on top of the piezo tube scanner inside the Z coarse positioning drive, which consists of a sapphire prism inside a phosphor bronze mantle. Relative movement in Z direction is provided by piezo stick-slip motors, which did not show exceptional susceptibility to problems, characteristic for the proven Pan design [61]. The slip-stick drive is based on the transition from static to dynamic friction between two sapphire slide pieces, of which one is glued on top of a shear piezo and the other connected to the object which is to be moved, in this case the tube scanner with attached tip. If the shear piezo is deflected slowly by an applied voltage with long rise time, the friction between the slide plate stays static and causes a movement of the tube scanner. If the shear piezo is now retracted fast with high rise time in the opposite direction, the inertia of the tube scanner overcomes the static frictional force and the slide plate glides back to its original position with less tube scanner movement than in the static case. When used in alternating fashion and repeated often enough, a macroscopic tip movement with step sizes of a few dozen nanometers and total ranges of multiple centimeters is possible.

However, the repeatability and accuracy of this process depends strongly on the normal force \vec{F}_N between the touching slide plates, which determines the maximum lateral static frictional

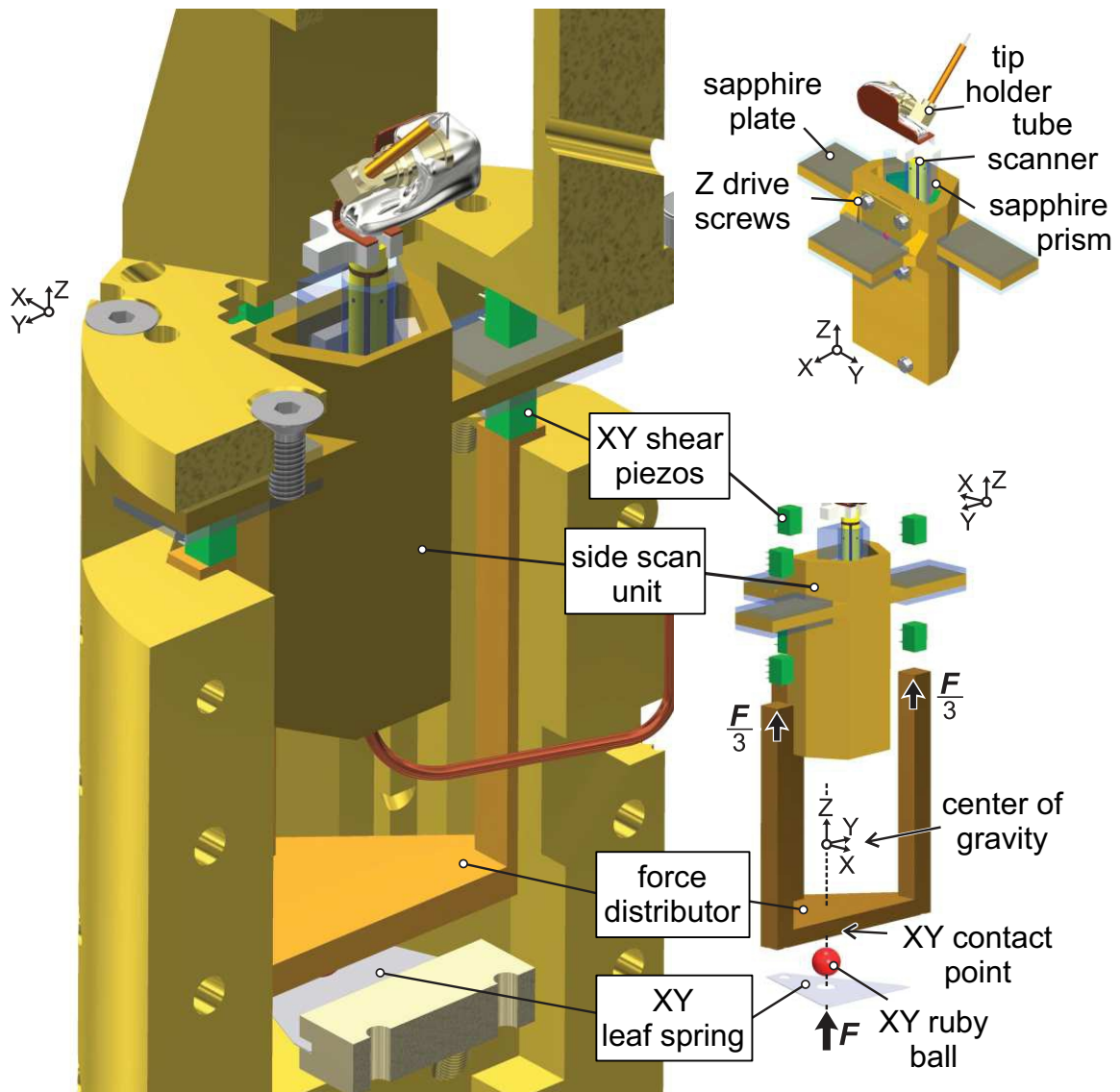


Figure 6.2: 3D schematic drawing of the side scanning unit. Left: Location of the scan unit in the STM body. Bottom right: XY piezo driver clamping mechanism. Top right: Side scanning unit with internal Z-drive and tip. Adapted with permission from [44].

force \vec{F}_S via the static friction equation $|\vec{F}_S| = \mu_S |\vec{F}_N|$ with the static coefficient of friction μ_S . The normal force is usually applied by clamping both pieces together with a screw-adjustable external spring, as shown in the top right part of Fig. 6.2. Too tight clamping does not allow sliding between the sapphire pieces, therefore no net movement is possible. Conversely, too loose clamping leads to sliding on both the forward and back parts of the cycle, therefore, no net movement occurs, too. The process is further complicated by changes in normal force due to differential thermal contraction of the materials during cooldown of the microscope, caused

6.2. State of the MP-STM before upgrade

by different coefficients of thermal expansion (CTE).

For XY coarse movement of the MP-STM side tips, a compact simultaneous X and Y drive design was chosen: On the outside of the Z-drive mantle, phosphor bronze wings with glued-on sapphire plates serve as slide surfaces for the coarse drive. Three pairs of piezo stacks, marked in green in Fig. 6.2, are pressed against the slide plates on the wings by a force distributor, which simultaneously clamps all three pairs with a joint normal force applied by the adjustable leaf spring. Stick-slip movement can then be performed either in X or Y direction by the piezo stacks, which consist of a pair of orthogonally oriented shear piezos each.

In principle, the design is well suited to equally distribute forces and provide a smooth movement of the side scan unit. In the actual experimental setup, several problems occurred:

- The long arms of the force distributors tend to jam in their narrow shafts, negating the purpose of the force distributor.
- Due to manufacturing tolerances, different glue thicknesses between piezo stacks and the arms, and/or handling-induced bending, the length of the three arms is not necessarily uniform and the magnitude of the normal force varies between the piezo stacks.
- If the stacks are not glued perfectly parallel on the arms, or the combined length of arms and piezo stacks are not equal, the normal force vector is tilted, leading to additional unwanted lateral forces.
- If the surfaces of all six sapphire slide plates are not in the same plane or tilted against each other, the normal forces gain a location-dependent component. As a consequence, the drive can get stuck at certain positions.

Apart from the problems induced by the force distributor, the glued connections between the sapphire plates and side scan unit wings often broke during a single consecutive cool down and warm up cycle. Each side tip has 6 of these glued connections and if only one is broken, the MP-STM becomes significantly more prone to external vibrations due to the rattling of the loose plate.

6.3 Upgrades

6.3.1 Improved side scanner XY coarse drive

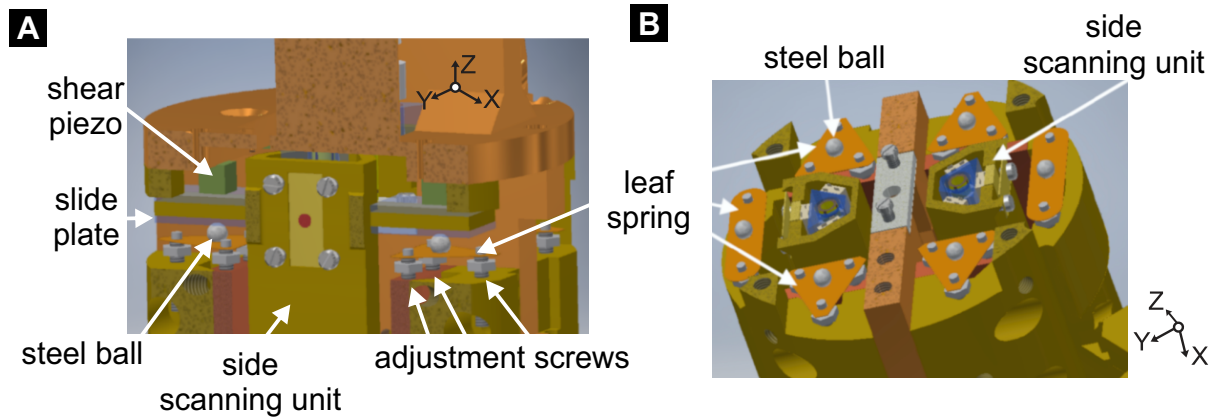


Figure 6.3: 3D sketches of the new clamping mechanism. A: Cut-view through the microscope in the XZ-plane. B: Cut view through the microscope in the XY-plane.

The problems of jamming and uneven force distribution were solved by a redesign of the side scanner XY coarse drive motor. Fig. 6.3 shows cut view sketches of the new clamping mechanism. The first change is the replacement of the joint force distribution system by three individual leaf springs: Each leaf spring is placed on top of adjustment screws, which simultaneously compensate for manufacturing induced length differences in the STM body support and allow independent changes of individual normal forces acting on each piezo contact position while the MP-STM is in an assembled state.

The second change replaces each of the lower three shear piezos with a stainless steel ball. The ball is held in position by small holes in the leaf springs and transmits the normal force of the leaf springs to the sapphire slide plates of the side scanning unit. This mechanical point contact prevents lateral components of the normal forces from reaching the slide plate. When the three remaining piezo shear stacks are operated to move the side scanning unit, the lower sapphire plates glide over the stainless steel balls.

6.3.2 Improved bonding of the side scanner slide plates

The problem of broken glue bonds between the gold-plated phosphor bronze wings of the side Z-drive mantle and the sapphire slide plates tended to be more complex. Fig. 6.4 A shows a simplified sketch of the problematic parts of the side scanner unit. As the lateral coarse drive needs to be functional even at low temperature $T \approx 1$ K, the common bonding techniques using the epoxy glue H77 or H20E turned out to be insufficient as the sapphire plate surfaces glued onto the wings are significantly larger than the surfaces which are commonly glued together in Z-coarse drive designs. Two failure modes occurring under thermal stress were found in the old design: Adhesive and cohesive failure due to the large CTE mismatch between gold-plated phosphor bronze, epoxy glue and the sapphire slide plates. Adhesive failure refers to the separation of the gold-epoxy or sapphire-epoxy interface, cohesive failure to a critical fracture inside the epoxy glue.

Adhesive failure could be prevented with an enhanced pre-glue treatment of the contact surfaces. The gold surface was hydrophobic after the standard UHV-cleaning procedure of subsequent water/soap, demineralized water and isopropyl alcohol ultrasonic baths. As epoxy glue in general acts hydrophilic, this leads to de-wetting of the interface and poor bond performance. The isopropyl alcohol step was removed to avoid possible solvated non-polar contaminations and the gold surface was subjected to a 20 second *aqua regia* treatment. Directly after, the freshly etched gold surface was found to be hydrophilic and therefore a better match to the epoxy glue.

Cohesive failure risk could be reduced by changing the glue geometry. The original design opted for one up to five non-connected, very thin ($d < 0.05$ mm) glue points between sapphire and gold. After contact with the glue manufacturer *Kummer GmbH*, it was found that, a) the conductive epoxy EJ2189 is more suited to the application than H77 and H20e and b) a uniform, thick ($d > 0.2$ mm) slab of glue over the whole contact area is better suited to distribute the mechanical stress due to the CTE mismatch. Also, a pre-glue vacuum treatment to remove trapped air bubbles from the epoxy, which could act as fracture nucleation sites, and a change in the epoxy heat curing to a two step process to achieve better form stability and crosslinking of the glue matrix, were included. The first step consists of 2 hours at $T = 65$ degrees C to set the glue and prevent the leaking of binder agents, followed by a one-hour ramp to $T = 150$ degrees C and one hour hold at the same temperature to harden the epoxy. The ramp was chosen to minimize thermal stress due to CTE mismatch.

Apart from the epoxy handling induced problems, the old design was very sensitive to manufacturing and handling-induced variations of the milled phosphor bronze wings parallelism,

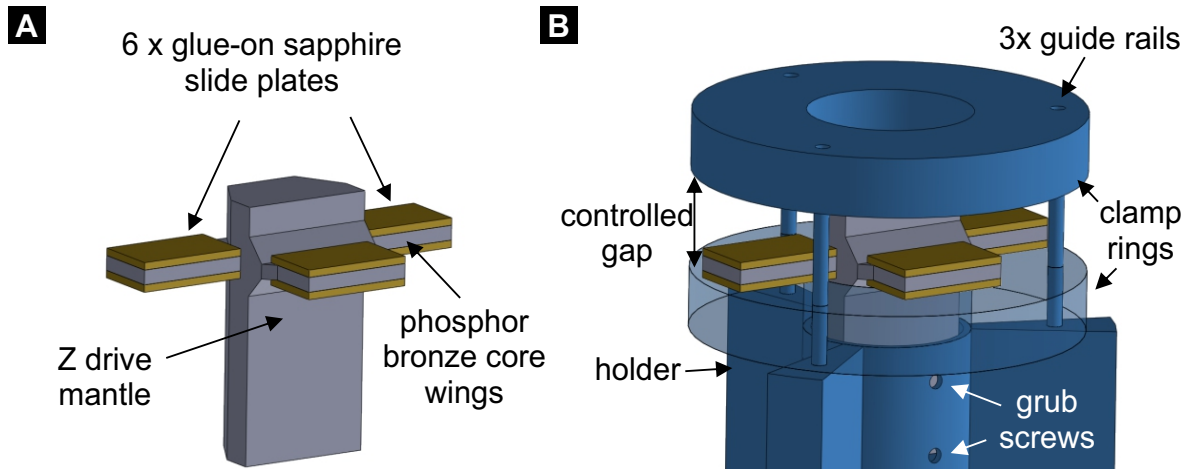


Figure 6.4: A: 3D sketch of the current side sled. The Z drive is located inside the mantle. B: Glueing control mechanism.

which here refers to the geometrical alignment of the top and bottom sapphire slide plates. If these are not perfectly parallel, the angle between them induces uneven, turning, or completely hindered movement of the XY coarse drives due to varying normal forces at different positions. To achieve a parallel configuration of all 6 slide plates, their alignment was stabilized during the curing process with the holder shown in Fig. 6.4 B. The side sled was clamped into the holder via 6 grub screws on 3 different sides. Then, after calculating the required controlled gap from parts and glue thicknesses, the sapphire plates were clamped between two precision manufactured rings, which are moveable on the guide rails. The gap width was then measured and/or adjusted via micrometer screws. The final position was fixed with nuts above and below the clamp rings to prevent the ring weight from squeezing out the glue during the curing process. Measured after the sled cooled to room temperature, the deviations from the parallel surface were below 20 micrometers.

A side sled with slide plates glued on via the control mechanism shown in Fig. 6.4 B was installed in the new XY coarse drive motor. The leaf spring controlled normal forces were then individually adjusted to allow smooth operation at ambient conditions and the design was subsequently tested in UHV at $T \approx 293$ K, 140 K, 65 K and 10 K with the same spring adjustment settings. At all temperatures, drive operation was successful [62].

6.3.3 Proposed general XY coarse drive improvement

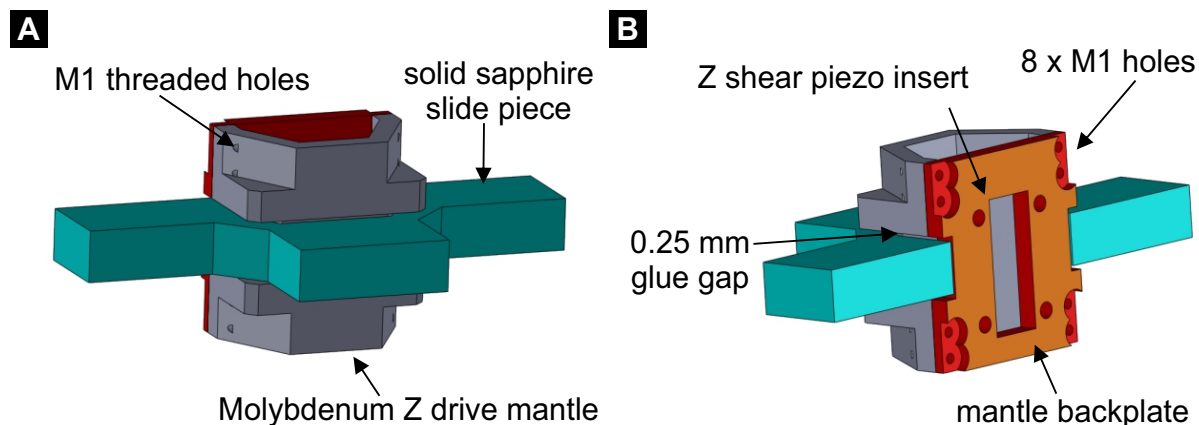


Figure 6.5: Proposed XY-coarse drive design to eliminate parallelism problems for the sample stage based on a solid sapphire slide piece glued to a modified mantle for the Z drive. Front (A) and back (B) view.

To further increase parallelism and smooth XY-drive motion, a new design proposal for the sample stage sled is shown in Fig. 6.5. The optical grade solid sapphire slide piece replaces the glued-on sapphire plates and the phosphor bronze wings, and guarantees a surface parallelism below 5 micrometers. For a nearly perfect CTE match to reduce thermal stress, the new Z-drive mantle will be composed of molybdenum. Also, the new design incorporates a removable backplate for easy access to the Z drive shear piezos. Mantle and slide piece will be glued together with a technique similar to the one described above.

6.3.4 New side tip design

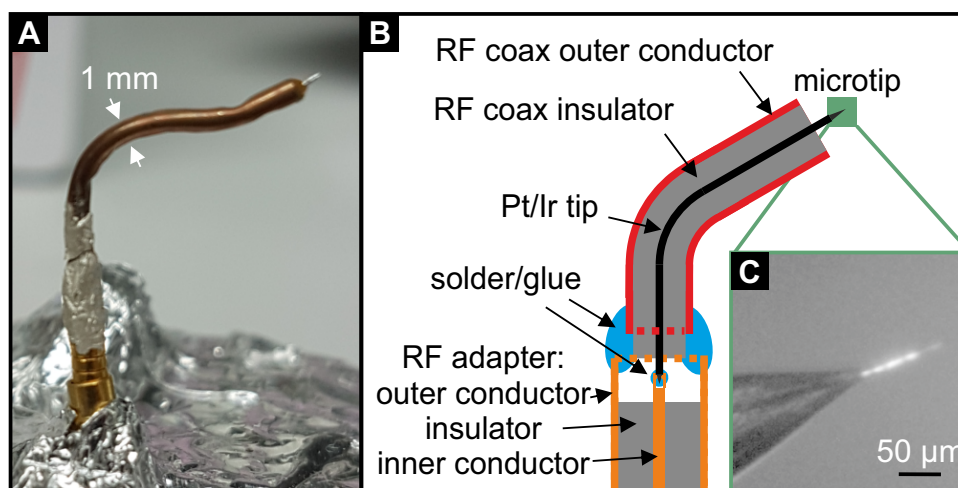


Figure 6.6: The new side tip design. A: Photograph of the new tip in a test holder. B: Cut-view schematic. C: Optical micrograph of the microtip.

The original side tips, as shown in Fig. 6.2, were composed of 4 consecutive 90 degree bends in the RF cable to incorporate the tip change mechanism shown in Fig. 6.2. The RF cable loop was presumed to be a good conductor of mechanical vibrations and therefore stabilized by a copper plate. Together with the rather bulky tip exchange mechanism, a lot of mass was concentrated on the top of the tube scanner. Higher mass on top of the tube scanner leads to a downshift of its mechanical resonance frequencies and makes the noise in the tunnel junction worse.

A lighter, streamlined version without unnecessary bends and minimal weight on top of the scanner is shown in Fig. 6.6. The center conductor of a semi-rigid RF coax was removed and replaced by a commercial Pt/Ir-tip (Nauga Needles) to prevent tip/wire interface connection problems. The lower end of the tip was then sharpened and inserted in the spring-based center conductor socket of a G3PO female RF adapter or female-female bullet. The connection was secured with either solder or conductive epoxy. Then, the RF coax and RF adapter outer conductors were connected via solder or epoxy to ensure proper shielding and mechanical stability of the STM tip. The resulting construction is very rigid and compatible with the standard SMPS connection system used elsewhere in the MPSTM. Tip to sample angle can be controlled primarily through the defined bend of the RF coax and secondarily through small but defined angle backlash in the SMPS connector.

6.4 System tests

The new tips and side scanners were installed in the MP-STM and tested in ambient conditions on top of an air-cushioned table.

6.4.1 Tube scanner XY calibration

To correlate the tube scanner control signals with a physical atomic-scale length, the XY-components of the scanner piezos were calibrated using highly oriented pyrolytic graphite (HOPG), a synthetic polycrystalline carbon allotrope. It consists of multiple, slightly misoriented and fused grains of monocrystalline graphite. Each individual crystallite is composed of vertically stacked sheets of graphene, a two-dimensional honeycomb lattice of carbon atoms in the (0001) plane, which are held together by strong covalent bonds with a bond length of $a = 142$ pm [63]. The graphene sheets stack in the ABAB configuration along the [0001] direction perpendicular to the (0001) plane and are held together by comparatively weak van der Waals forces. These weak bonds allow the preparation of a clean sample surface by removing some of the topmost graphene layers with adhesive tape.

A model of the HOPG surface is shown in Fig. 6.7 B. Due to the ABAB stacking, not all surface atoms are equal: The blue colored atoms lie above carbon atoms of the first subsurface layer, while the yellow colored ones lie above the empty centers of the honeycomb hexagons. Due to asymmetrically increased LDOS near the Fermi energy, the yellow atoms appear higher in topographic STM images and form a triangular lattice [64].

Fig. 6.7 C shows a STM topography of a freshly cleaved HOPG sample, recorded with the left tip of the upgraded MP-STM. A triangular lattice is visible in the image, but disturbed by noise due to relative vibrations between tip and sample, and probable ad- and desorption events at the tip apex. Both effects lead to horizontal stripes in the image, parallel to the fast scanning direction. To improve lattice visibility, the dynamic range of the brown color scale was limited to 80 pm, and all height values outside of this band were displayed as black and white. A fast Fourier transform (FFT) of the image is displayed in the small insert in Fig. 6.7 C and shows 6 bright spots, marked by the green circles. Each spot corresponds to a periodic structure of the real space image, and its distance from the center equals the inverse period length, averaged over the whole image. By cutting out all regions outside the green circles and computing the inverse FFT, all that remains from the original image is the triangular lattice, which is blended into the original image via the blue-yellow round insert in Fig. 6.7 C. The big insert shows a zoom-in on one of the white hexagons, with marked atom positions. The triangular lattice

of yellow spots appears to be rotated relative to the FFT spots, therefore the FFT spots do not correspond to the distance between the individual yellow atoms, but to the distance of yellow atom rows, which is marked in Fig. 6.7 B with striped lines. Based on the honeycomb lattice geometry, a line distance $b = (1 + \cos 60^\circ) \cdot a = 213$ pm results.

The actual calibration consists of comparing this computed line distance with the FFT-measured line distance and multiplying the measured image length scale with the calibration factor $r = b_{\text{comp.}}/b_{\text{FFT}}$. The size bar in Fig. 6.7 C is equivalent to an image distance of 1 nm, calibrated via this method. The calibration factor as determined on HOPG can be used to accurately display distances in future STM images.

The same procedure was repeated for the central and right tip, and the used STM topographic images are displayed in Fig. 6.7 A and D. All hexagons in the big inserts of A, C and D are irregular due to the presence of thermal drift during image acquisition, which compresses or stretches the measured lattice. To minimize its influence on the calibration factor, the fast scan axis was oriented close to perpendicular to one of the yellow atom rows and only the corresponding FFT spot was used for the calibration.

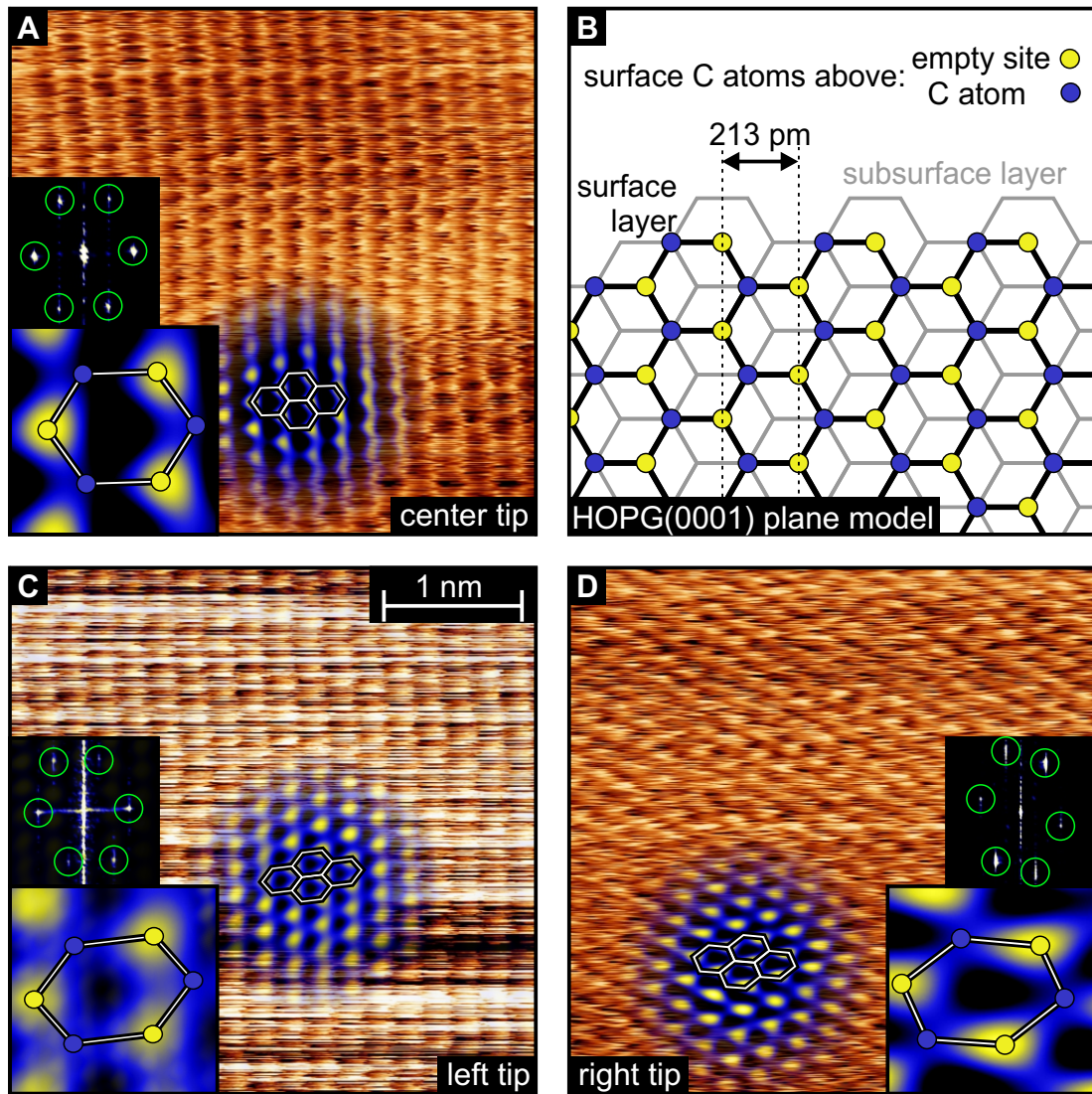


Figure 6.7: Scanner XY-calibration using HOPG. A,C,D: Atomic resolution STM topography in ambient conditions, color scale described in the main text. Filtered topography blended in via round inserts, honeycomb lattice marked in white. Small inserts: Fast Fourier transform of the topography with high symmetry points marked by green circles. Big inserts: Zoom-in of the filtered topographic images with marked atomic positions. B: HOPG lattice model, blue and yellow circles represent individual carbon atoms of the surface layer. A: $I_T = 5 \text{ nA}$, $U = 2 \text{ mV}$. C: $I_T = 3 \text{ nA}$, $U = 100 \text{ mV}$. D: $I_T = 9 \text{ nA}$, $U = 7 \text{ mV}$.

6.4.2 Tube scanner Z calibration

The Z-components of the tube scanners were calibrated with another known atomic length scale, the distance between Au(111) atomic layers. In the fcc crystal, the distance between (111) layers b is defined by $b = a/\sqrt{3} = 235$ pm, with the Au lattice spacing $a = 408$ pm. The Au(111) single crystal was cleaned via flame annealing and constant-current STM images were recorded. The images were tilt-corrected, then rectangular shapes were cut out with the long side parallel to the fast scan direction for drift influence minimizing. The results are shown in Fig. 6.8 A for the individual STM tips. The Au crystal was polished at a slightly different angle to the (111) surface, therefore monoatomic terraces form at the Au(111) surface during the annealing process. The height difference between the terraces is equivalent to the (111) layer distance, as shown by the model in Fig. 6.8 B. On the right side of Fig. 6.8 A, the z histograms of the STM images show separate peaks for each height level, marked with the same numbers as the terraces in the STM images. Each histogram peak was individually fitted with a gaussian distribution $f(z) \propto \exp(-(z - z_0)^2/(2\sigma^2))$ to determine the average z value of an individual terrace z_0 and its standard deviation σ . The fit centers of all peaks of the left tip image histogram from Fig. 6.8 A are plotted against the Au(111) layer number x in Fig. 6.8 C and subsequently fitted with a linear function $A + bx$, weighted with the standard deviations, to extract the average step height b . The intercept of the fit function A is equivalent to the extrapolated z value of terrace number 0, depends on the arbitrarily chosen zero point of the z -scale and is therefore of no significance. The actual calibration consists of comparing the measured b to the known layer distance of 235 pm and multiplying the image z -scale with the recalibration factor $r = 235 \text{ pm}/b$. The procedure was repeated for the center and right tip of the MP-STM and results in the calibrated z -scale of the height histograms in Fig. 6.8 A.

The results of the room temperature XY and Z calibrations are combined in Tab. 6.1. The displayed scan ranges in rows 2 and 4 are obtained by multiplication of the calibrated linear calibration constants C_i with an applied scanner deflection voltage $U = 80$ V for the lateral and $U = \pm 200$ V for the vertical directions.

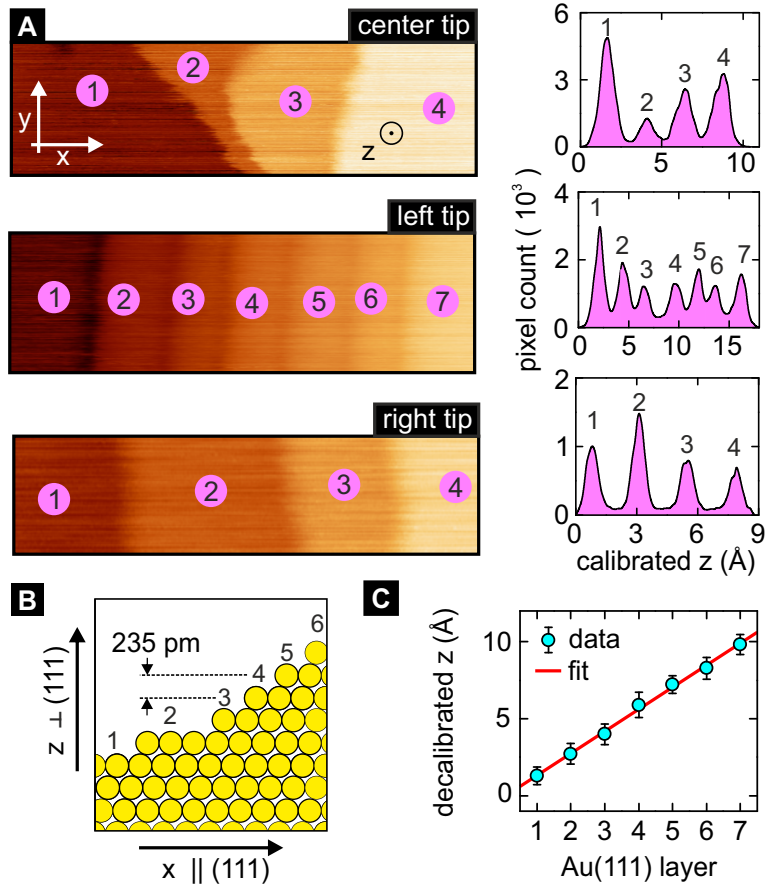


Figure 6.8: Scanner Z-calibration using Au(111) step edges. A: STM topography in ambient conditions with corresponding height histogram and marked Au(111) layer numbers. B: Au(111) side view lattice model. C: Step height fit of the calibration procedure described in the text. Center tip: $I_T = 5$ nA, $U = -60$ mV. Left tip: $I_T = 8$ nA, $U = -60$ mV. Right tip: $I_T = 6$ nA, $U = -60$ mV.

Table 6.1: Room temperature tube scanner calibration results.

	left scanner	center scanner	right scanner
C_{xy} (nm/V)	8.13	20.37	9.63
xy-range (nm)	650	1630	771
C_z (nm/V)	1.92	1.44	2.68
z-range (nm)	766	574	1072
C_{xy}/C_z	4.24	14.20	3.59

6.4.3 Lateral current test

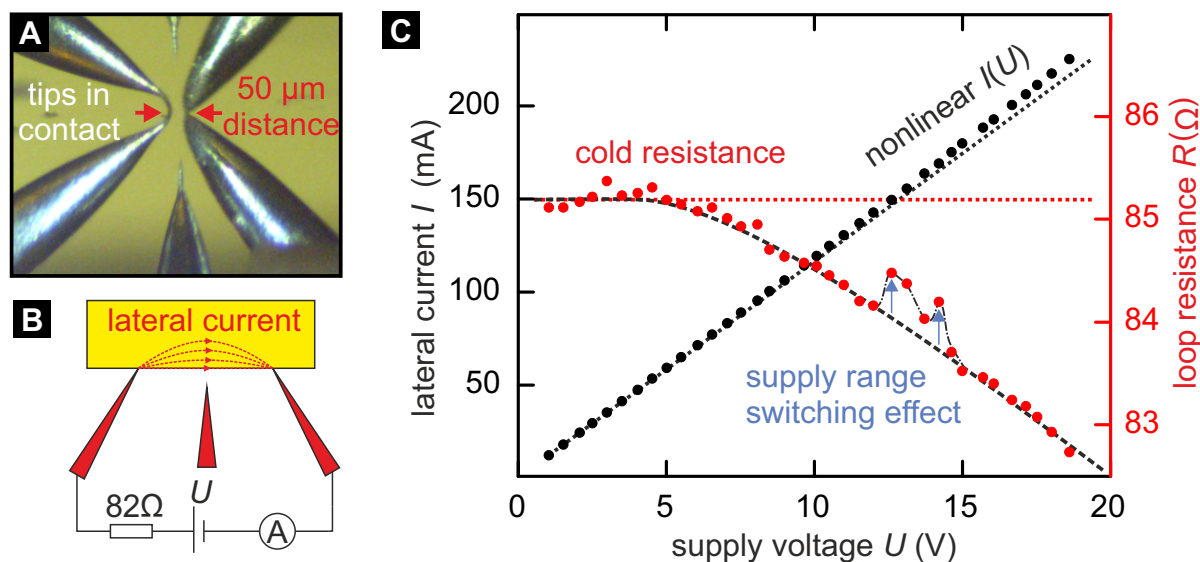


Figure 6.9: A: Optical micrograph of the tip configuration. B: Simplified wiring schematics. C: Lateral current and loop resistance vs. applied supply voltage plot. The black dotted line represents the linear $I(U)$ curve expected from an ideal ohmic resistor. The red dotted line is the circuit resistance at low voltage. The black striped curve serves as a guide to the eye for the loop resistance without switch effects.

One of the main reasons to build a MPSTM is to conduct transport measurements with an applied lateral current. To demonstrate this capability, the outer Pt/Ir tips were contacted very close to each other with the Au(111) crystal and a lateral current of up to 220 mA was applied between them (Fig. 6.9 A,B). Tip to sample approach was realized by the coarse Z positioning system, while the current between the tip and biased sample ($U_b < 1$ mV) was monitored with the Nanonis SPM control system. After contact was indicated by a sudden jump from zero to finite current, the tip wiring was disconnected and the same procedure repeated for the other side tip. After both were in contact, the sample bias wire was disconnected, resulting in a floating sample potential.

A lateral current is the result of a potential difference at both ends of a resistor. Here, the resistor consists of the serially connected Au(111) sample, two Pt/Ir tips and the RF cables leading from the UHV feedthroughs to the tips, all of which are highly conductive. Therefore, a small voltage has to be used to prevent sudden high current flow.

A series resistor switch with selectable resistance from $R_s = 82 \Omega$ to $R_s = \infty$ (disconnected) was installed between the outer tips and the output of a power supply U_S . The loop resistance of the circuit (resistor switch at 82Ω plus sample, tips, contact resistance, and cables) was

measured to be $R \approx 85 \Omega$. According to the voltage divider formula $U_t = \frac{R-R_s}{R}U_S$, a relatively high supply voltage leaves a small voltage between the tip contacts $U_t \approx 0.035 U_S$. Therefore, a stable voltage source can be used as a stable very low voltage source.

Supply voltage was provided by a standard laboratory power source, and the resulting current through the circuit was measured by a multimeter. Loop resistance was calculated via Ohm's law $R = U_S/I$, both quantities are shown in Fig. 6.9 C. For small voltages (and currents), the voltage-current relationship remains linear. Above $U_s = 5 \text{ V}$, the current increases faster than the ideal Ohmic behavior and consequently, the loop resistance decreases. This behavior was caused by Joule heating of the ceramic 82Ω resistor, which has a slightly negative temperature coefficient. Irregularities in the resistance curve are caused by voltage range switching in the power supply, which allows the resistor to cool for a short time. At the maximum tested current $I = 225 \text{ mA}$ at $U_S = 18.6 \text{ V}$, the thermal heating power can be calculated by $P_{th} = U_S I = 4.2 \text{ W}$. Most of the heat is generated in the resistor switch according to $P_{th} = RI^2 = 4.04 \text{ W}$, the remaining 160 mW are shared between the rest of the circuit's elements. At the point contacts between the tips and sample, the highest resistance and therefore Joule heating are expected, but no evidence for spot welding of the tips to the sample was found, as they could be separated after the experiment with no apparent damage.

To estimate the distribution of Joule heating in the tips and sample, the individual resistances of the sample and the two contact points have to be measured. In the two-probe geometry of this lateral current experiment, only the sum of sample and contact resistances is accessible. A separation of both components is possible by a four-point resistance measurement, which could be performed with a four-probe STM.

In [65], the lateral current between two tips on the surface of a thick sample was estimated to spread to a width roughly twice the tip distance d . Symmetry considerations suggest, that the current spreads to a sample depth of d , therefore the current between both point contacts must flow through an area of $A = 2d \cdot d$. The corresponding current density $j = I/A$ then yields 40 MA/m^2 for $I = 200 \text{ mA}$ with $d = 50 \mu\text{m}$ from the experiment.

With the automated lateral approach program described in [42], a tip-tip distance of 500 nm should be easy to reach. The resulting $j = 0.4 \text{ TA/m}^2$ exceeds the threshold of 0.2 TA/m^2 needed for skyrmion movement as found in [12]. In a thin film based sample, much lower lateral currents are needed due to changes in sample geometry. At a sample thickness of 100 nm , 0.4 TA/m^2 can be achieved with $I = 40 \text{ mA}$ at the same tip separation.

Chapter 7

Conclusion

As main part of this thesis, the properties of skyrmions and other magnetic nanostructures inhabiting the Pd/Fe/Ir(111) sample system were investigated by variable-temperature and time-resolved scanning tunneling microscopy and spectroscopy.

Measurements were performed on the face centered cubic palladium-iron double layer, which was grown by molecular beam epitaxy on the surface of an Ir(111) single crystal. The preparation method resulted in fcc-Pd/Fe nanoislands of different sizes and shapes.

Magnetic nanostructure imaging was conducted by utilization of the non-collinear magnetoresistance effect (NCMR), which manifests in dI/dU signal intensity differences for spin textures with different mean canting angles between neighboring spins. NCMR is caused by local density of states (LDOS) modification due to mixing of the spin-up and spin-down tunneling channels in the tunneling junction. Parallel and anti-parallel aligned (summarized as collinear) neighboring spins do not modify the sample LDOS. The field-polarized (FP) phase, where spins align with the external field, is an example. With increased angle between neighboring spins, thereby increased non-collinearity, the LDOS is reduced proportional to the canting angle at $U = 700$ mV. Skyrmions (SK) and other inhomogeneous spin textures like spin spirals (SS) of Pd/Fe/Ir(111) are examples for this scenario.

As a control experiment, the previously known low-temperature SS, SK and FP phases were confirmed at $T < 4$ K. Due to the finite size of the Pd/Fe nanoislands, the regular, hexagonal skyrmion lattice phase could not be found, instead the skyrmions occurred either in coexistence with the SS at low magnetic fields $B = 1$ T perpendicular to the (111) sample plane or in coexistence with the FP phase at high magnetic fields $B > 1$ T. At even higher $B \geq 2$ T, stochastic skyrmion creation and annihilation events were found.

Time resolved scanning tunneling spectroscopy was employed to record the magnetic telegraph signal caused by the stochastic changes in dI/dU signal intensity at a fixed position on the sample. Through statistical telegraph signal analysis, mean SK and FP lifetimes, the SK asymmetry,

and creation/annihilation rates could be extracted for the same switching position at different temperatures $1.58 \text{ K} \leq T \leq 7.7 \text{ K}$ and $B = 2.5 \text{ T}$. With increasing T , a decrease in the lifetimes and SK asymmetry was found. The non-thermal and thermal contribution to the SK annihilation and creation rates could be separated by fitting a combined model. Crossover from non-thermal to thermal creation and annihilation occurred at $T \approx 4.0 \text{ K}$.

Caused by the rapid increase of transition rates with T , time-resolved methods were not available at elevated temperature. Instead, the interpretation of the dI/dU maps had to change to a time-averaged concept. Based on a comparison with micromagnetic simulations of a similarly shaped and sized nanoisland [51], one can conclude that skyrmions move inside the island on trajectories determined by the lateral potential energy landscape shaped by pinning defects, island edges and the interaction with other skyrmions. The resulting patches of dI/dU signal intensity in between FP and SK levels correspond to positions with a certain averaged skyrmion probability, effectively transforming the dI/dU map to a map of skyrmion probability density. The ordered magnetic phases could be found within their particular magnetic field boundaries at up to $T = 78 \text{ K}$ and showed no significant deviations from their low-temperature appearance, except for a general decrease in SK-FP dI/dU contrast, probably caused by the time-averaging effect.

Above the critical temperature $T_C = 78 \text{ K}$, a new magnetic texture with significant differences to the ordered phases was discovered. It consists of irregularly shaped objects with varying degrees of local spin collinearity, whose characteristic length scale and average collinearity increases with B . Through dI/dU map analysis at $T = 90 \text{ K}$ and 95 K , a two-step process was found to phenomenologically describe the B dependence of the observed structures: First, the filigree patches with lower collinearity are compressed into less, but larger objects. The remaining large structures are gradually forced to align with the external magnetic field. At the maximum achievable $B = 3 \text{ T}$, the process is still incomplete and the field-polarized state is not yet reached. The experimental dI/dU -maps of the new spin phase closely resemble Monte-Carlo simulations of a fluctuation-disordered (FD) phase consisting of rapidly fluctuating objects with irregular size and shape.

A cumulative thermomagnetic phase diagram was constructed by combination of the investigated fcc-PdFe nanoislands. For each NCMR image of an island, the occurring magnetic phases were assigned according to fixed criteria. The experimental $B - T$ phase diagram corresponds quantitatively and qualitatively well to Monte-Carlo based phase diagrams, which report the first critical temperature $T_C = 81 \text{ K}$ [29] resp. $T_C = 100 \text{ K}$ [28], compared to the experimental result of $T_C = 78 \text{ K}$. Compared to the nanoskyrmion lattice of Fe/Ir(111) with a critical temperature of $T_C \approx 28 \text{ K}$ [21], the additional capping layer of palladium increased the

thermal skyrmion stability by a factor of nearly 3. This is likely caused by enhanced exchange interaction between the Fe atoms and the highly polarizable, almost ferromagnetic Pd atoms [17].

The second part of the thesis focused on the improvement of a multi-probe scanning tunneling microscope (MP-STM), which ultimately could be used to access dynamic transport properties of skyrmions.

The side tip lateral macro-positioning motors were radically altered to counter several of the weak points found in the previous iteration of the MP-STM. Its joint force distribution system was split into individually adjustable clamping springs for each piezoelectric driver. Also, one set of the drivers was replaced with stainless steel glide balls to eliminate uneven and tilted force distributions. Additionally, the epoxy glued bonds between the support structure and glide plates of the macro-positioning system were found to be prone to thermocycling damage during subsequent MP-STM bakeout and cool-down. The epoxy glue was changed in formula, bond geometry and curing process, and a tailored surface treatment and pre-cure epoxy treatment procedure was developed to maximize adhesion and bond toughness between the glide plates and support structure. The new motor design was tested at variable temperature and found to be operational at ambient conditions as well as for $293\text{ K} \geq T \geq 10\text{ K}$ in UHV conditions with the same mechanical settings of the clamping springs.

The side tip design and exchange mechanism were also improved to a lightweight, rigid design without unnecessary bends in the RF cables leading to the tip.

Test measurements on freshly cleaved highly oriented pyrolytic graphite and flame-annealed Au(111) surfaces were used to calibrate the tube scanners of all three tips. Here, constant-current atomic resolution was achieved for all tips in ambient conditions on an air-cushioned table, which proves enhanced MP-STM stability over the previous design, where only the center tip was able to achieve this result in a vibrationally isolated UHV chamber.

A lateral current experiment was performed to showcase the MP-STM readiness for transport experiments with a maximum current of 225 mA between two side tips in contact with the sample. If a smaller current of 200 mA is imprinted with an easy to achieve tip-to-tip distance of 500 nm, the resulting current density of $0.4\text{ TA}/\text{m}^2$ will already exceed the skyrmion movement threshold of $0.22\text{ TA}/\text{m}^2$ in [12].

The next step will consist of more design changes to include the proposed new single crystal sapphire slide piece on the sample coarse drive and a compatible new STM head with improved wiring. After that, the assembled microscope will be tested in cryogenic UHV conditions with the ultimate goal of replacing the RF-STM used for the skyrmion experiments in this thesis,

enabling radio-frequency atomic-scale skyrmion transport experiments at variable temperatures and external magnetic fields.

Bibliography

- [1] E. Masanet, A. Shehabi, N. Lei, S. Smith and J. Koomey. *Recalibrating global data center energy-use estimates*. Science **367**(6481):984 (2020).
- [2] *Bitcoin energy consumption index*. <https://digiconomist.net/bitcoin-energy-consumption>. Accessed 2020-06-14.
- [3] *Electricity domestic consumption data*. <https://yearbook.enerdata.net/electricity/electricity-domestic-consumption-data.html>. Accessed 2020-06-14.
- [4] T. H. R. Skyrme. *A non-linear field theory*. Proceedings of the Royal Society A: Mathematical, Physical and Engineering Sciences **260**(1300) (1961).
- [5] I. Dzyaloshinsky. *A thermodynamic theory of "weak" ferromagnetism of antiferromagnetics*. Journal of Physics and Chemistry of Solids **4**(4):241 (1958).
- [6] T. Moriya. *Anisotropic superexchange interaction and weak ferromagnetism*. Physical Review **91**(1):91 (1960).
- [7] P. J. Hsu, A. Kubetzka, A. Finco, N. Romming, K. von Bergmann and R. Wiesendanger. *Electric-field-driven switching of individual magnetic skyrmions*. Nature Nanotechnology **12**(2):123 (2017).
- [8] S. Mühlbauer, B. Binz, F. Jonietz, C. Pfleiderer, C. Rosch, A. Neubauer, R. Georgii and P. Böni. *Skyrmion lattice in a chiral magnet*. Science **323**(5916):915 (2011).
- [9] C. Hanneken, F. Otte, A. Kubetzka, B. Dupé, N. Romming, K. von Bergmann, R. Wiesendanger and S. Heinze. *Electrical detection of magnetic skyrmions by tunnelling non-collinear magnetoresistance*. Nature Nanotechnology **10**(12):1039 (2015).
- [10] N. Romming, C. Hanneken, M. Menzel, J. E. Bickel, B. Wolter, K. von Bergmann, A. Kubetzka and R. Wiesendanger. *Writing and Deleting Single Magnetic Skyrmions*. Science **341**(6146):636 (2013).

- [11] C. Hanneken, A. Kubetzka, K. von Bergmann and R. Wiesendanger. *Pinning and movement of individual nanoscale magnetic skyrmions via defects*. New Journal of Physics **18**(5):055009 (2016).
- [12] S. Woo, K. Litzius, B. Krüger, M. Y. Im, L. Caretta, K. Richter, M. Mann, A. Krone, R. M. Reeve, M. Weigand, P. Agrawal, I. Lemesh, M. A. Mawass, P. Fischer, M. Kläui and G. S. Beach. *Observation of room-temperature magnetic skyrmions and their current-driven dynamics in ultrathin metallic ferromagnets*. Nature Materials **15**(5):501 (2016).
- [13] S. Meyer, M. Perini, S. von Malottki, A. Kubetzka, R. Wiesendanger, K. von Bergmann and S. Heinze. *Isolated zero field sub-10 nm skyrmions in ultrathin Co films*. Nature Communications **10**:3823 (2019).
- [14] G. Binnig, H. Rohrer, C. Gerber and E. Weibel. *Tunneling through a controllable vacuum gap*. Applied Physics Letters **40**(2):178 (1982).
- [15] R. J. Hamers. *Atomic-Resolution Surface Spectroscopy With the Scanning Tunneling Microscope*. Annual Review of Physical Chemistry **40**:531 (1989).
- [16] R. Wiesendanger, H. J. Güntherodt, G. Güntherodt, R. J. Gambino and R. Ruf. *Observation of vacuum tunneling of spin-polarized electrons with the scanning tunneling microscope*. Physical Review Letters **65**(2):247 (1990).
- [17] B. Dupé, M. Hoffmann, C. Paillard and S. Heinze. *Tailoring magnetic skyrmions in ultrathin transition metal films*. Nature Communications **5**:4030 (2014).
- [18] P. J. Hsu, L. Rózsa, A. Finco, L. Schmidt, K. Palotás, E. Vedmedenko, L. Udvardi, L. Szunyogh, A. Kubetzka, K. von Bergmann and R. Wiesendanger. *Inducing skyrmions in ultrathin Fe films by hydrogen exposure*. Nature Communications **9**:1571 (2018).
- [19] S. Seki, X. Z. Yu, S. Ishiwata and Y. Tokura. *Observation of skyrmions in a multiferroic material*. Science **336**(6078):198 (2012).
- [20] X. Z. Yu, Y. Onose, N. Kanazawa, J. H. Park, J. H. Han, Y. Matsui, N. Nagaosa and Y. Tokura. *Real-space observation of a two-dimensional skyrmion crystal*. Nature **465**(7300):901 (2010).
- [21] S. Heinze, K. von Bergmann, M. Menzel, J. Brede, A. Kubetzka, R. Wiesendanger, G. Bihlmayer and S. Blügel. *Spontaneous atomic-scale magnetic skyrmion lattice in two dimensions*. Nature Physics **7**(9):713 (2011).

- [22] P. Lindner. *Untersuchung von Wachstum und magnetischen Eigenschaften der Eisenmonolage auf Ir / YSZ / Si (111) mittels spinpolarisierter Rastertunnelmikroskopie*. B.Sc. Thesis, Universität Hamburg (2014).
- [23] N. Romming, A. Kubetzka, C. Hanneken, K. von Bergmann and R. Wiesendanger. *Field-dependent size and shape of single magnetic Skyrmions*. Physical Review Letters **114**(17):177203 (2015).
- [24] J. Hagemester, N. Romming, K. von Bergmann, E. Y. Vedmedenko and R. Wiesendanger. *Stability of single skyrmionic bits*. Nature Communications **6**:8455 (2015).
- [25] P. Lindner. *Untersuchung der Interskyrmion-Wechselwirkung in Palladium-Eisen-Nanoinseln auf Ir(111) mittels zeitaufgelöster Rastertunnelmikroskopie*. M.Sc. Thesis, University of Hamburg (2016).
- [26] E. Ising. *Beitrag zur Theorie des Ferromagnetismus*. Zeitschrift für Physik **31**(1):253 (1925).
- [27] L. Onsager. *Crystal Statistics. A Two-Dimensional Model with an Order-Disorder Transition*. Physical Review **65**(3):117 (1944).
- [28] L. Rózsa, E. Simon, K. Palotás, L. Udvardi and L. Szunyogh. *Complex magnetic phase diagram and skyrmion lifetime in an ultrathin film from atomistic simulations*. Physical Review B **93**(2):024417 (2016).
- [29] M. Böttcher, S. Heinze, S. Egorov, J. Sinova and B. Dupé. *B-T phase diagram of Pd/Fe/Ir(111) computed with parallel tempering Monte Carlo*. New Journal of Physics **20**(10):103014 (2018).
- [30] F. Hund. *Zur Deutung der Molekelspektren. III*. Zeitschrift für Physik **43**(11-12):805 (1927).
- [31] L. Nordheim. *Zur Theorie der thermischen Emission und der Reflexion von Elektronen an Metallen*. Zeitschrift für Physik **46**(11-12):833 (1928).
- [32] J. Tersoff and D. R. Hamann. *Theory and application for the scanning tunneling microscope*. Physical Review Letters **50**(25):1998 (1983).
- [33] R. Wiesendanger. *Scanning Probe Microscopy and Spectroscopy: Methods and Applications*, Band (Cambridge University Press, Cambridge, 1994).

- [34] M. Julliere. *Tunneling between ferromagnetic films*. Physics Letters A **54**(3):225 (1975).
- [35] E. C. Stoner. *Collective Electron Ferromagnetism. II. Energy and Specific Heat*. Proceedings of the Royal Society A: Mathematical, Physical and Engineering Sciences **169**(938):339 (1939).
- [36] S. Blundell. *Magnetism in Condensed Matter* (Oxford University Press, Oxford, 2001).
- [37] D. Wortmann, S. Heinze, P. Kurz, G. Bihlmayer and S. Blügel. *Resolving Complex Atomic-Scale Spin Structures by Spin-Polarized Scanning Tunneling Microscopy*. Physical Review Letters **86**(18):4132 (2001).
- [38] C. Gould, C. Rüster, T. Jungwirth, E. Girgis, G. M. Schott, R. Giraud, K. Brunner, G. Schmidt and L. W. Molenkamp. *Tunneling anisotropic magnetoresistance: a spin-valve-like tunnel magnetoresistance using a single magnetic layer*. Physical Review Letters **93**(11):117203 (2004).
- [39] C. Hanneken. *Observation of Non-Collinear Magnetoresistance by Scanning Tunneling Spectroscopy on Skyrmions in PdFe / Ir (111)*. Dissertation, Universität Hamburg (2015).
- [40] J. Friedlein. *A radio frequency-spin-polarized-scanning tunneling microscope for spin dynamics experiments*. Dissertation, Universität Hamburg (2018).
- [41] J. Friedlein, J. Harm, P. Lindner, L. Bargsten, M. Bazarnik, S. Krause and R. Wiesendanger. *A radio-frequency spin-polarized scanning tunneling microscope*. Review of Scientific Instruments **90**(12):123705 (2019).
- [42] J. Harm. *Konzeption eines Mehrfach-Spitzen-Rastertunnelmikroskops für spinaufgelöste Experimente mit hoher Zeitauflösung*. M.Sc. Thesis, Universität Hamburg (2014).
- [43] A. Hellwig. *Helmholtz coil schematic*. https://en.wikipedia.org/wiki/Helmholtz_coil#/media/File:Helmholtz_coils.png. Accessed 2016-10-12.
- [44] J. Harm. *Entwicklung und Aufbau einer Tieftemperatur-Ultrahochvakuumanlage für spinaufgelöste Mehrfach-Spitzen-Rastertunnelmikroskopie mit hoher Zeitauflösung*. Dissertation, Universität Hamburg (2019).
- [45] L. Bargsten. *Experimentelle Untersuchung des thermomagnetischen Phasendiagramms von Pd/Fe/Ir(111) mittels Rastertunnelmikroskopie*. M.Sc. Thesis, University of Hamburg (2017).

- [46] K. von Bergmann, S. Heinze, M. Bode, G. Bihlmayer, S. Blügel and R. Wiesendanger. *Complex magnetism of the Fe monolayer on Ir(111)*. *New Journal of Physics* **9**:396 (2007).
- [47] I. V. Shvets, R. Wiesendanger, D. Bürgler, G. Tarrach, H. J. Güntherodt and J. M. Coey. *Progress towards spin-polarized scanning tunneling microscopy*. *Journal of Applied Physics* **71**(11):5489 (1992).
- [48] A. Kubetzka, M. Bode, O. Pietzsch and R. Wiesendanger. *Spin-Polarized Scanning Tunneling Microscopy with Antiferromagnetic Probe Tips*. *Physical Review Letters* **88**(5):057201 (2002).
- [49] A. Schlenhoff, S. Krause, G. Herzog and R. Wiesendanger. *Bulk Cr tips with full spatial magnetic sensitivity for spin-polarized scanning tunneling microscopy*. *Applied Physics Letters* **97**(8):083104 (2010).
- [50] M. Bode, O. Pietzsch, A. Kubetzka and R. Wiesendanger. *Shape-Dependent Thermal Switching Behavior of Superparamagnetic Nanoislands*. *Physical Review Letters* **92**(6):067201 (2004).
- [51] A. F. Schäffer, L. Rózsa, J. Berakdar, E. Y. Vedmedenko and R. Wiesendanger. *Stochastic dynamics and pattern formation of geometrically confined skyrmions*. *Communications Physics* **2**:72 (2019).
- [52] A. P. Li, K. W. Clark, X. G. Zhang and A. P. Baddorf. *Electron transport at the nanometer-scale spatially revealed by four-probe scanning tunneling microscopy*. *Advanced Functional Materials* **23**(20):2509 (2013).
- [53] A. Bannani, C. A. Bobisch and R. Möller. *Local potentiometry using a multiprobe scanning tunneling microscope*. *Review of Scientific Instruments* **79**(8):083704 (2008).
- [54] R. Hobara, N. Nagamura, S. Hasegawa, I. Matsuda, Y. Yamamoto, Y. Miyatake and T. Nagamura. *Variable-temperature independently driven four-tip scanning tunneling microscope*. *Review of Scientific Instruments* **78**(5):053705 (2007).
- [55] F. Lüpke, S. Korte, V. Cherepanov and B. Voigtländer. *Scanning tunneling potentiometry implemented into a multi-tip setup by software*. *Review of Scientific Instruments* **86**(12):123701 (2015).

- [56] M. Salomons, B. V. Martins, J. Zikovsky and R. A. Wolkow. *Four-probe measurements with a three-probe scanning tunneling microscope*. Review of Scientific Instruments **85**(4):045126 (2014).
- [57] I. M. Miron, T. Moore, H. Szambolics, L. D. Buda-Prejbeanu, S. Auffret, B. Rodmacq, S. Pizzini, J. Vogel, M. Bonfim, A. Schuhl and G. Gaudin. *Fast current-induced domain-wall motion controlled by the Rashba effect*. Nature Materials **10**(6):419 (2011).
- [58] S. S. P. Parkin, M. Hayashi and L. Thomas. *Magnetic Domain-Wall Racetrack Memory*. Science **320**(5873):190 (2008).
- [59] J. V. Barth, R. J. Behm, H. Brune and G. Ertl. *Scanning tunneling microscopy observations on the reconstructed Au(111) surface: Atomic structure, long-range superstructure, rotational domains, and surface defects*. Physical Review B **42**(15):9307 (1990).
- [60] J. Koch. *Aufbau und Charakterisierung eines Mehrspitzen-Rastertunnelmikroskops für Hochfrequenzmessungen*. M.Sc. Thesis, Universität Hamburg (2019).
- [61] S. H. Pan, E. W. Hudson and J. C. Davis. *^3He refrigerator based very low temperature scanning tunneling microscope*. Review of Scientific Instruments **70**(2):1459 (1999).
- [62] P. Ewerhardt. *Aufbau und Optimierung eines Drei-Spitzen-Rastertunnel-Mikroskops*. B.Sc. Thesis, Universität Hamburg (2019).
- [63] Y. Wang, Y. Ye and K. Wu. *Simultaneous observation of the triangular and honeycomb structures on highly oriented pyrolytic graphite at room temperature: An STM study*. Surface Science **600**(3):729 (2006).
- [64] D. Tomanek, S. G. Louie, H. J. Mamin, D. W. Abraham, R. E. Thomson, E. Ganz and J. Clarke. *Theory and observation of highly asymmetric atomic structure in scanning-tunneling-microscopy images of graphite*. Physical Review **35**(14):7790 (1987).
- [65] S. Hasegawa. *Multi-Probe Scanning Tunneling Microscopy*. In: Kalinin S., Gruverman A. (eds) *Scanning Probe Microscopy* (Springer, New York, NY. 2007).

Publications

- P. Lindner, L. Bargsten, S. Kovarik, J. Friedlein, J. Harm, S. Krause and R. Wiesendanger. *Temperature and magnetic field dependent behavior of atomic-scale skyrmions in Pd/Fe/Ir(111) nanoislands*. Physical Review B **101** 214445 (2020).
- J. Friedlein, J. Harm, P. Lindner, L. Bargsten, M. Bazarnik, S. Krause and R. Wiesendanger. *A radio-frequency spin-polarized scanning tunneling microscope*. Review of Scientific Instruments **90** 123705 (2019).
- A. Schlenhoff, P. Lindner, J. Friedlein, S. Krause, R. Wiesendanger, M. Weigl, M. Schreck, and M. Albrecht *Magnetic nano-skyrmion lattice observed in a Si-wafer-based multilayer system*. ACS Nano **9** 5908 (2015).

Conference contributions

- P. Lindner, L. Bargsten, J. Friedlein, J. Harm, S. Krause, and R. Wiesendanger. *Experimental Investigation into the thermomagnetic Phase Diagram of Pd/Fe/Ir(111)*. 82nd Spring Conference, Deutsche Physikalische Gesellschaft, Berlin (Germany). 15.03.2018 (Talk).
- P. Lindner, J. Friedlein, J. Harm, S. Krause, and R. Wiesendanger. *Repulsive Skyrmion Interaction observed in Pd/Fe-Nanoislands on Ir(111)*. 81st Spring Conference, Deutsche Physikalische Gesellschaft, Dresden (Germany). 21.03.2017 (Talk).
- A. Schlenhoff, S. Krause, P. Lindner, J. Friedlein, R. Wiesendanger, M. Weinl, M. Schreck, and M. Albrecht. *A Magnetic Nano-Skyrmion Lattice Observed in a Si-Wafer Based Multilayer System*. International Conference on Nanoscience and Technology, Busan (Republic of Korea). 23.08.2016 (Talk).
- S. Krause, A. Schlenhoff, P. Lindner, J. Friedlein, R. Wiesendanger, M. Weinl, M. Schreck, and M. Albrecht. *A Magnetic Nano-Skyrmion Lattice Observed in a Si-Wafer Based Multilayer System*. 20th International Conference on Magnetism (ICM-20), Barcelona (Spain). 10.07.2015 (Talk).
- S. Krause, A. Schlenhoff, P. Lindner, J. Friedlein, R. Wiesendanger, M. Weinl, M. Schreck, and M. Albrecht. *A Magnetic Nano-Skyrmion Lattice Observed in a Si-Wafer Based Multilayer System*. 79th Spring Conference, Deutsche Physikalische Gesellschaft, Berlin (Germany). 16.03.2015 (Talk).
- P. Lindner, L. Bargsten, S. Kovaric, J. Friedlein, J. Harm, S. Krause, and R. Wiesendanger. *Experimental Thermomagnetic Phase Diagram of Pd/Fe/Ir(111)*. 8th International Conference on Scanning Probe Spectroscopy (SPS 2019), Hamburg (Germany). 18.06.2019 (Poster).

- P. Lindner, L. Bargsten, S. Kovarik, J. Friedlein, J. Harm, S. Krause, and R. Wiesendanger. *Probing the Thermomagnetic Phase Diagram of Pd/Fe/Ir(111) via STM*. SkyMag 2017, Paris (France). 03.05.2017 (Poster).
- A. Schlenhoff, P. Lindner, J. Friedlein, S. Krause, R. Wiesendanger, M. Weinl, M. Schreck and M. Albrecht. *A Magnetic Nano-Skyrmion Lattice observed in a Si-wafer based Multilayer System*. SkyMag 2017, Paris (France). 03.05.2017 (Poster).

Danksagung / Acknowledgements

Ich danke insbesondere:

- **Prof. Dr. Roland Wiesendanger** für die Betreuung meiner Promotion, die Übernahme des Erstgutachtens, und vor allem die Möglichkeit, seit dem Jahre 2014 in dieser Forschungsgruppe kontinuierlich arbeiten und forschen zu dürfen.
- **Prof. Dr. Michael Thorwart** für die Übernahme des Zweitgutachtens.
- **Dr. Stefan Krause** für kritische Diskussion der Ergebnisse, kontinuierliche Betreuung, und die angenehme Atmosphäre in der Lab018 Untergruppe.
- Meinen Kollegen **Dr. Johannes Friedlein, Dr. Jonas Harm und Lennart Bargsten** für die enge Zusammenarbeit in Aufbau, Messungen, und kontinuierlicher Weiterentwicklung der Lab005-Anlage, an der die Pd/Fe/Ir(111)-Messungen im ersten Teil dieser Arbeit durchgeführt wurden.
- Meinem Kollegen **Jonas Koch** für die enge Zusammenarbeit in der Weiterentwicklung des Mehrfachspitzen-Rastertunnelmikroskops, mit dem sich der zweite Teil dieser Arbeit befasst.
- **Patrick Ewerhardt, Hermann Osterhage, Dr. Cody Friesen, Dr. Anika Schlenhoff** und allen anderen Mitglieder unserer Forschungsgruppe für die produktive Arbeitsumgebung.

Den Teams der Heliumversorgung, Feinmechanik- und Elektronikwerkstatt danke ich für die zuverlässige Versorgung mit Kühlflüssigkeiten und schnelle Umsetzung von Designideen.

Mein ganz herzlicher Dank gilt meinen Eltern Gesine und Jonas, und meiner Schwester Juliane für die Unterstützung in allen Jahren meines Studiums. Ihr habt diese Arbeit erst möglich gemacht.

Für Lilly.

Eidesstattliche Versicherung / Declaration on oath

Hiermit versichere ich an Eides statt, die vorliegende Dissertationsschrift selbst verfasst und keine anderen als die angegebenen Hilfsmittel und Quellen benutzt zu haben.

Die eingereichte schriftliche Fassung entspricht der auf dem elektronischen Speichermedium.

Die Dissertation wurde in der vorgelegten oder einer ähnlichen Form nicht schon einmal in einem früheren Promotionsverfahren angenommen oder als ungenügend beurteilt.

Hamburg, den 30. 09. 2020

Unterschrift des Doktoranden